Technische Universität München

Physik Department

MPQ

Cold Guided Beams of Polar Molecules

Michael Motsch

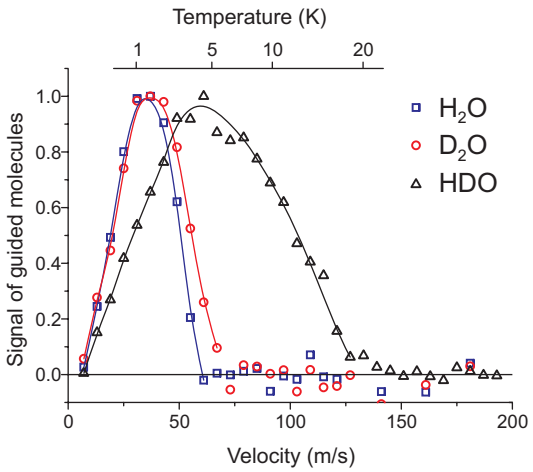

Dissertation

Max-Planck-Institut für Quantenoptik, Garching
and Physik Department, Technische Universität München

December 2009

Cover illustration: The figure on the cover shows velocity distributions of cold guided water molecules produced by electrostatic velocity filtering. These distributions illustrate the different sensitivity of the water isotopologs H_2O, D_2O, and HDO to external electric fields.

Technische Universität München
Max-Planck-Institut für Quantenoptik

Cold Guided Beams of Polar Molecules

Michael Motsch

Vollständiger Abdruck der von der Fakultät für Physik der Technischen Universität München zur Erlangung des akademischen Grades eines

Doktors der Naturwissenschaften (Dr. rer. nat.)

genehmigten Dissertation.

Vorsitzender :		Univ.-Prof. Dr. W. Zwerger
Prüfer der Dissertation :	1.	Hon.-Prof. Dr. G. Rempe
	2.	Univ.-Prof. Dr. St. Paul

Die Dissertation wurde am 30. 10. 2009 bei der Technischen Universität München eingereicht und durch die Fakultät für Physik am 11. 12. 2009 angenommen.

Abstract

This thesis reports on experiments characterizing cold guided beams of polar molecules which are produced by electrostatic velocity filtering. This filtering method exploits the interaction between the polar molecules and the electric field provided by an electrostatic quadrupole guide to extract efficiently the slow molecules from a thermal reservoir. For molecules with large and linear Stark shifts such as deuterated ammonia (ND_3) or formaldehyde (H_2CO), fluxes of guided molecules of 10^{10}–10^{11} molecules/s are produced. The velocities of the molecules in these beams are in the range of 10–200 m/s and correspond to typical translational temperatures of a few Kelvin. The maximum velocity of the guided molecules depends on the Stark shift, the molecular mass, the geometry of the guide, and the applied electrode voltage. Although the source is operated in the near-effusive regime, the number density of the slowest molecules is sensitive to collisions. A theoretical model, taking into account this velocity-dependent collisional loss of molecules in the vicinity of the nozzle, reproduces the density of the guided molecules over a wide pressure range. A careful adjustment of pressure allows an increase in the total number of molecules, whilst yet minimizing losses due to collisions of the sought-for slow molecules. This is an important issue for future applications.

Electrostatic velocity filtering is suited for different molecular species. This is demonstrated by producing cold guided beams of the water isotopologs H_2O, D_2O, and HDO. Although these are chemically similar, they show linear and quadratic Stark shifts, respectively, when exposed to external electric fields. As a result, the flux of HDO is larger by one order of magnitude, and the flux of the individual isotopologs shows a characteristic dependence on the guiding electric field.

The internal-state distribution of guided molecules is studied with a newly developed diagnostic method: depletion spectroscopy of formaldehyde. First, ultraviolet absorption spectroscopy of the $\tilde{A}^1A_2 \leftarrow \tilde{X}^1A_1$ transition of formaldehyde is performed in a room-temperature gas to extract molecular constants. These findings are used to address single rotational states of guided molecules. Since the formaldehyde molecules dissociate upon ultraviolet excitation, the laser-frequency-dependent decrease in the number of guided molecules allows to extract the population of individual rotational states in the beam. With the source temperature set to 155 K, populations of rotational states exceeding 10 % are observed, which validates the theoretical model of velocity filtering.

Finally, Rayleigh scattering into an optical cavity is investigated as an alternative, non-destructive detection method for cold molecules. Comparing the rate of scattering into the fundamental cavity mode to that into the same mode under free-space conditions, an enhancement by a factor of up to 38 is observed for room-temperature gases. This Purcell-like enhancement is explained by interference of electromagnetic fields scattered by a classical driven dipole oscillator in the resonator.

Zusammenfassung

Die vorliegende Arbeit berichtet über Experimente mit kalten geführten Molekülstrahlen, die mittels der elektrostatischen Geschwindigkeitsfilterung erzeugt werden. Dabei wird die Wechselwirkung zwischen polaren Molekülen und einem elektrischen Quadrupolführungsfeld ausgenutzt, um die langsamen Moleküle auf effiziente Weise aus einem thermischen Reservoir zu extrahieren. Für Moleküle wie Ammoniak (ND_3) oder Formaldehyd (H_2CO), die eine große lineare Stark-Verschiebung erfahren, lassen sich Flüsse von 10^{10}–10^{11} Molekülen/s realisieren. Die geführten Moleküle haben Geschwindigkeiten von 10–200 m/s, was einer Temperatur von einigen Kelvin entspricht. Die Höchstgeschwindigkeit der Moleküle wird durch ihre Stark-Verschiebung und Masse, die Geometrie der Molekülführung sowie die angelegte Elektrodenspannung bestimmt. Obwohl die Molekülzufuhr auf den naheffusiven Bereich eingestellt wird, reagiert die Zahl der langsamsten Moleküle empfindlich auf Stöße. Ein Modell, das solche geschwindigkeitsabhängigen Verluste durch Stöße im Bereich der Düse berücksichtigt, beschreibt die Dichte der geführten Moleküle über einen weiten Druckbereich. Eine Optimierung des Druckes erlaubt, die Gesamtzahl der Moleküle zu erhöhen, während Verluste der langsamsten Moleküle durch Stöße minimiert werden. Dies ist für zukünftige Anwendungen wichtig.

Die Vielseitigkeit der elektrostatischen Geschwindigkeitsfilterung wird durch die Erzeugung kalter geführter Strahlen der Wasserisotopologe H_2O, D_2O und HDO demonstriert. Obwohl chemisch sehr ähnlich, zeigen sie im externen elektrischen Feld einen linearen bzw. quadratischen Stark-Effekt. Der Fluss an kaltem HDO ist daher um eine Größenordnung höher, und der Fluss der Isotopologe zeigt jeweils eine charakteristische Abhängigkeit vom angelegten elektrischen Führungsfeld.

Die Verteilung der internen Zustände der geführten Moleküle wird mittels einer neu entwickelten Methode, der Entvölkerungsspektroskopie von Formaldehyd, untersucht. Zunächst wird zur Bestimmung von Molekülkonstanten in einem thermischen Formaldehydgas Absorptionsspektroskopie des ultravioletten Übergangs $\tilde{A}^1A_2 \leftarrow \tilde{X}^1A_1$ durchgeführt. Damit lassen sich dann einzelne Rotationszustände im geführten Molekülstrahl ansprechen. Da Formaldehydmoleküle bei ultravioletter Anregung dissoziieren, lässt der Einbruch im Signal der geführten Moleküle auf die Besetzung einzelner Zustände im Strahl schließen. Bei einer Temperatur der Quelle von 155 K werden Zustandsbevölkerungen von über 10 % beobachtet, was die im Vorfeld entwickelte Theorie der Geschwindigkeitsfilterung eindeutig bestätigt.

Mit der Rayleigh-Streuung in einen optischen Resonator wird eine alternative, nicht destruktive Detektionsmethode für kalte Moleküle untersucht. Die Rate der Streuung in die fundamentale Resonatormode ist für thermische Gase um einen Faktor 38 höher als jene in dieselbe Mode im freien Raum. Diese dem Purcell-Effekt entsprechende Überhöhung wird durch Interferenz der von einem klassischen getriebenen Dipol gestreuten elektromagnetischen Wellen beschrieben.

Contents

Chapter 1

Cold polar molecules

The field of cold and ultracold atoms has received a lot of attention in the last two decades. The use of light forces for cooling of atoms, constituting a main ingredient for this research field, was proposed already early on [Ash70, Hän75, Win75, Ash78]. Shortly after the advent of stable, narrow-linewidth lasers, laser cooling of trapped ions [Neu78, Win78] and, only few years later, of free atoms in the gas phase was demonstrated[1]. The development of these laser-cooling techniques has paved the way for investigations in the field of fundamental light-matter interactions and ultracold quantum gases. Therefore, the 1997 Nobel Prize in Physics was jointly awarded to S. Chu, C. Cohen-Tannoudji, and W. D. Phillips "for development of methods to cool and trap atoms with laser light". The demonstration of Bose-Einstein condensation (BEC) in dilute atomic gases was a research highlight employing these newly-developed cooling techniques. To honour this, the 2001 Nobel Prize in Physics was awarded to E. A. Cornell, W. Ketterle, and C. E. Wieman "for the achievement of Bose-Einstein condensation in dilute gases of alkali atoms, and for early fundamental studies of the properties of the condensates"[2]. Only few years later, the cold atom community routinely uses such dense and cold atomic gases trapped in optical lattices to study problems arising in solid-state systems such as, e.g., the superfluid to Mott-insulator phase transition [Gre02, Vol06, Vol07] or Anderson localization [Bil08, Roa08]. Ultracold atomic gases can also be used to study phenomena related to superconductivity such as the BEC-BCS crossover [Blo08, Gio08]. Here, ultracold atomic fermions are paired up by a suitably tailored magnetic interaction to form a bosonic compound system resembling a Cooper pair.

The degrees of freedom in these atomic systems are, however, limited to electronic excitations and to different nuclear spin states. A natural development would be to extend this field of research by including molecules, which offer additional degrees

[1] For a review of these developments see, e.g., the 1997 Nobel-Prize lecture by W. D. Phillips [Phi98] and references therein.

[2] For a review of the developments on the route to BEC in cold atomic gases see, e.g., the 2002 Nobel-Prize lectures by E. A. Cornell and C. E. Wieman [Cor02], W. Ketterle [Ket02], and references therein.

of freedom such as vibrational and rotational excitations. Furthermore, especially polar molecules are subject to the long-range, anisotropic dipole-dipole interaction, which is of special interest for cold chemistry and also promises to pave the road for new developments in quantum information science and quantum simulations. In the following section, some research fields which are expected to benefit from the availability of samples of cold polar molecules are presented: cold chemistry, quantum information science, and measurements of the electron's electric dipole moment. For a broader overview, the reader is referred to some recent special issues on cold and ultracold polar molecules in Eur. Phys. J. D [Doy04], J. Phys. B [Dul06], and New J. Phys. [Car09].

1.1 Applications of cold polar molecules

Before discussing possible applications of cold polar molecules, a definition of the term "cold" shall be given [Doy04, Kre08]. The *cold regime* is reached, when the magnitude of the interaction between the molecules and an externally applied electric or magnetic field becomes comparable to the thermal energy. For typical laboratory fields and molecular dipole moments this happens at temperatures of around 1 K. At these energies, the distribution of internal molecular states is strongly purified as compared to an ensemble at room temperature. Therefore, collisions between cold molecules are strongly influenced by the contribution of single rotational states, which can exhibit significantly differing collision properties. However, different partial waves contribute to the scattering process in the cold regime. This changes once the *ultracold regime* is reached at typical temperatures of around 1 mK. In this regime a collision between the molecules can be fully described by s-wave scattering, i.e., only a single partial wave contributes to the scattering process. For even lower temperatures the *quantum-degenerate regime* is approached. Here, effects caused by quantum statistics such as the Pauli exclusion principle strongly contribute to the interaction between particles.

1.1.1 Cold chemistry and cold collisions

The dynamics of chemical reactions is often governed by a barrier in the reaction coordinate. To overcome this reaction barrier and drive the reaction, energy must be fed to the reactants. In the cold regime with collision energies corresponding to a temperature on the order of 1 K, there is not enough energy available to overcome such a barrier. Nevertheless, exothermic chemical reactions with a barrier are predicted to take place even under such conditions due to quantum-mechanical tunneling, as was theoretically shown for the reaction $F + H_2 \rightarrow FH + H$ [Bal01, Bal02].

The influence of rotational excitation on the dynamics of chemical reactions was investigated by J. J. Gilijamse *et al.*, who measured the cross section of the collision between cold OH radicals and Xe atoms [Gil06]. In their experiment, cold OH

molecules were produced by Stark deceleration and collided with a supersonic Xe jet. By adjusting the final velocity of the OH molecules in the range of 33–700 m/s, the collision energy was varied from 50–400 cm^{-1}. At collision energies exceeding the energy corresponding to the lowest rotational excitations of the OH molecule, new reaction channels opened in the inelastic collision, as observed from the appearance of population in excited rotational states of OH. B. C. Sawyer *et al.* reported on a similar study of collisions between cold molecules and an atomic or molecular gas jet [Saw08]. In this experiment a supersonic beam of He or D_2 was collided with magnetically trapped OH molecules. In this trap, OH molecules at a density of 10^6 cm^{-3} and a temperature of 70 mK were stored for 430 ms. The collision energy was adjusted by heating the valve for the supersonic expansion of He or D_2, which tuned the beam's velocity. This way, center-of-mass energies of 60–230 cm^{-1} (145–210 cm^{-1}) were accessible for the collision He–OH (D_2–OH). When the collision energy was reduced below the threshold energy for rotational excitation of OH, a sudden drop in the loss rate of molecules from the trap was found, indicating a reduced collision cross section when this inelastic channel is not available. Even more examples for cold chemistry can be found by including also ionic species. The reaction $Ca^+ + CH_3F \rightarrow CaH^+ + CH_2F$ was studied by S. Willitsch *et al.* using a laser-cooled crystal of Ca^+ ions stored in a linear Paul trap and a slow beam of CH_3F produced by electrostatic velocity filtering and guiding [Wil08a, Wil08b, Bel09a]. J. Mikosch *et al.* studied the nucleophilic substitution reaction $Cl^- + CH_3I \rightarrow I^- + CH_3Cl$, by crossed molecular beam imaging to clarify the reaction pathway [Mik08a, Mik08b].

In cold collisions, the interaction energy between the molecule and an externally applied electric or magnetic field can be on the same order of magnitude as the collision energy. Calculations of scattering rates for OH radicals show that the long-range dipole-dipole interaction dominates collisions between polar molecules [Avd02]. Therefore, formation rates in these low-energy chemical reactions are expected to be modifiable and finally even controllable by applying suitable electric and magnetic fields [Kre05, Kre08, Bel09b]. As a prototype system, the hydrogen abstraction channel in the reaction $H_2CO + OH \rightarrow HCO + H_2O$ was theoretically studied [Hud06]. This system is of special interest since both involved species, formaldehyde (H_2CO) molecules and OH radicals, can be produced at tunable energies by Stark deceleration and even electrostatically trapped. In this reaction, the barrier is adjustable by an external electric field, such that suppression effects in the reaction rate could be observable.

Externally applied fields can also play an important role for the lifetime of molecules in electric or magnetic traps. For example, calculations show that suitable electric offset fields can prevent trap losses by inelastic collisions [Boh01]. Another example are collisions between cold $^{17}O_2$ and atomic ^{3}He in the presence of magnetic fields [Vol02]. Such conditions are present in setups combining buffer-gas cooling with magnetic trapping. For buffer-gas cooled and magnetically trapped NH molecules, inelastic collisions with He were identified as trap-loss mechanisms [Cam07, Cam09].

1.1.2 Quantum information science

One of the key challenges in quantum information science is to find systems permitting fast gate operations, strong and controllable couplings between individual qubits, and, at the same time, long decoherence times. Molecules, in general, possess a rich internal level structure, including long-lived rotational states which seem adequate to encode quantum information in. D. DeMille proposed to use an array of polar molecules stored in suitable electric fields as an architecture for a quantum computer [DeM02]. Here, the information is encoded in the orientation of the molecular dipole moment with respect to an externally applied electric field. At the same time the electric dipole moment promotes a coupling between individual qubits. Together with single-qubit rotations, these controlled couplings constitute a necessity for universal quantum-gate operations. C. M. Tesch and R. de Vivie-Riedle suggested to use vibrationally excited molecules for quantum information processing [Tes02]. Here, the different vibrational modes of a molecule are used as qubits, while the quantum-logic operations are driven by shaped femtosecond laser pulses. A. André *et al.* proposed to couple polar molecules to a microwave stripline cavity [And06, Côt06]. While the molecular rotational states are used for storage of quantum information, the strong dipole coupling to the cavity-enhanced electric field permits an efficient means for transferring the information to the resonator. This way, the coupling between distant qubits can be mediated over large distances by the microwave cavity field. Furthermore, the strong coupling of the molecules to the intracavity field can be used for sideband cooling in the trap [Vul01, Wal08, Lei09]. P. Rabl *et al.* suggested to use a setup combining molecular ensembles and a Cooper-pair box coupled to a stripline cavity [Rab06]. While the Cooper-pair box can be used for fast gate operations, the molecules, offering long decoherence times, serve as a quantum memory. The coupling between these two is achieved via the stripline cavity, which can also be used to convert the information stored in the molecular ensemble to a flying qubit in the microwave field. Molecular ensembles coupled to such stripline cavities can also be used to implement a many-qubit system, where the information can either be stored in the collective excitation of the ensemble [Tor08a] or in a spatial phase variation over the ensemble [Tor08b].

Another proposed application of cold polar molecules is their use for quantum simulations. The idea of using a well-controllable quantum system to simulate the unknown behavior of another quantum system dates back to R. Feynman [Fey82, Bul09]. Ultracold atomic or molecular gases which are trapped in optical lattices could be used to simulate the behavior of solid-state systems described by different Bose-Hubbard models [Lew07]. Especially polar molecules are ideal tools to simulate the Hamiltonians of such systems. As proposed by A. Micheli *et al.*, lattice spin systems can be realized by considering diatomic polar molecule stored in an optical lattice where the spin is mapped on a single valence electron [Lew06, Mic06]. The anisotropic spin-spin interactions are then replaced by the dipole-dipole interaction between the polar molecules in combination with microwave excitations and

spin-rotation couplings. By choosing suitable arrangements and orientations of the molecular dipoles with respect to each other, the Hamiltonians corresponding to different physical systems can then be simulated.

As shown in the preceding paragraph, a whole variety of proposals for applications of cold polar molecules in quantum information science exists. However, the challenge remains to prepare suitable samples of cold polar molecules. For many of the above-mentioned schemes, the molecules must be localized to a high degree, e.g., in an optical dipole trap or an optical lattice, and prepared in a well-defined initial state. Furthermore, gate operations demand for the well-controlled coupling of internal states by phase-coherent light fields.

1.1.3 Precision spectroscopy: Tests of CPT symmetry

Due to their rich internal structure, which at first seems to complicate the interpretation of their spectra, molecules are excellent candidates for precision tests of CPT symmetry (C: charge conjugation, P: parity transformation, T: time reversal). The first experimental demonstration of a violation of any of the three fundamental symmetries was the observation of an asymmetry in the β-decay of polarized ^{60}Co by C. S. Wu *et al.* [Wu57]. This asymmetry is caused by parity violation in the weak interaction, as suggested by T. D. Lee and C. N. Yang [Lee56]. Furthermore, this observation already hinted at a combined violation of C and P symmetry [Lee57, Wu57] which was confirmed by the observation of CP violation in the decay of the neutral K meson system [Chr64]. However, if CP symmetry is broken, also T symmetry must not be conserved to fulfill the CPT theorem, considered an essential constituent of quantum field theory [Pau55].

The search for a permanent electric dipole moment (EDM) of the neutron or of the electron bound in atoms or in molecules represents one possible test of T and CPT symmetry [Pur50, Hun91, Bol08]. P. G. H. Sanders pointed out that the effect of the EDM of an electron in an atomic system is significantly enhanced by relativistic effects (the enhancement scales as $\propto \alpha^2 Z^3$, with α being the fine structure constant and Z the nuclear charge) as compared to the free electron's EDM [San65, Com07]. Therefore, the so far most precise tests of the electron's EDM have been performed in heavy atoms such as ^{205}Tl [Reg02] or ^{199}Hg [Gri09]. These experiments give an upper bound for the electron's EDM of $d_e < 3 \times 10^{-29}\, e\,\mathrm{cm}$ (e is the elementary charge, $e = 1.602 \times 10^{-19}\,\mathrm{C}$). While the standard model of particle physics predicts a value of $10^{-38}\, e\,\mathrm{cm}$ for the electron's EDM, theories beyond the standard model predict values in the range $< 10^{-26} - 10^{-28}\, e\,\mathrm{cm}$ [Com99]. The sensitivity in these experiments has therefore reached a level which seems eligible to discriminate between such models.

Even larger enhancement effects are present in polar molecules which makes them very attractive for the search for the EDM of the electron [Hin97, DeM00, Koz02, Mey08, Mey09, Tar09]. The energy shift due to the electron's EDM d_e, which an atom or molecule experiences in an externally applied electric field E_a, is given by $d_e \cdot P(E_\mathrm{a}) \cdot E_\mathrm{int}$, where E_int is the atomic or molecular-structure-dependent internal

electric field, and $P(E_a)$ is the degree of polarization of the atom or molecule. While the internal electric field of heavy atoms and molecules can have similar size, the degree of polarization is much larger in molecules. In atoms, different electronic energy levels must be mixed to induce a polarization. In polar molecules, these electronic states are already mixed by the chemical bond. Therefore, only rotational states must be mixed to induce a polarization. Due to their proximity on the energy scale, this results in a larger degree of polarization for an applied electric field of the same magnitude. Furthermore, polar molecules have the advantage of being less sensitive to stray magnetic fields. First experiments with molecules (YbF) have been performed and are already close to reaching a sensitivity compatible with the experiments employing atoms [Hud02]. In this experiment, a molecular beam effusing out of a hot oven containing Yb and AlF_3 has been used. The use of a cold, slow beam of YbF is expected to bring an additional sensitivity due to the longer interaction times with the probing laser fields [Sau06a, Sau06b].

1.2 Production of cold polar molecules

The complex internal structure of molecules, which facilitates the promising applications discussed in the preceding paragraphs, necessitates new cooling schemes. Laser cooling, which has enabled the production of ultracold atomic samples, relies on iteratively scattering photons on a more or less closed cycling transition [Met99]. In general, the plethora of internal states accessible in molecules upon spontaneous decay from an electronically excited state renders standard laser-cooling and repumping schemes unfeasible. Nevertheless, there might be a few special molecular systems with very favorable Franck-Condon factors. In these rare cases, the number of vibrational states within the electronic ground state which are populated upon spontaneous decay might be restricted to a sufficiently small number to make laser cooling possible [DR04, Stu08].

In recent years a variety of techniques has been developed which allow for the production of molecular samples in the cold and even the ultracold domain (see, e.g., the special issues on cold molecules in Eur. Phys. J. D [Doy04], J. Phys. B [Dul06], and New J. Phys. [Car09]). These may be subdivided in two groups: On the one hand side, there are *indirect methods* which start with ultracold atomic samples and produce bound atom pairs, i.e., molecules, using either magnetic Feshbach resonances [Köh06] or photoassociation [Jon06]. Since these molecules are produced in collisions of ultracold atom pairs by "controlled chemistry", no kinetic energy release occurs. The molecules produced by these methods are therefore translationally at roughly the same temperature as the atoms. Since a coupling must be mediated between a bound molecular state and a pair of free atoms, the molecules produced that way typically occupy highly excited internal molecular states. On the other hand side, *direct methods* start with "real" molecules, either from supersonic beam sources or thermal reservoirs. Different techniques aim at the control of the exter-

nal degrees of motion by suitably tailored electric [Bet99, Ran03, vdM08], magnetic [Nar08b], or optical [Ful04] fields. Cooling of the internal motion is achieved either in a supersonic expansion [Pau00] or by collisions with a cryogenic buffer gas [Wei98]. Cold molecules can also be produced by implantation of molecules into helium nanodroplets [Toe98, Sti01]. Since these molecules intrinsically interact with the helium environment, this latter cooling mechanism falls outside the scope of this thesis and is not further discussed here.

1.2.1 Indirect methods: Forging molecular bonds between ultracold atoms

Magnetic Feshbach resonances occur in collisions between two atoms, when an incident open channel is coupled to a closed molecular channel. In collisions between ultracold atoms the states involved are different hyperfine states coupled by some sort of interaction. Due to their different magnetic moments, the relative energy between these states can be tuned by external magnetic fields. By suitable ramps of these fields, population can be transferred from an atom-pair state to a bound molecular state [Joc03, Reg03, Zwi03, Dür04, Ino04, Sta04]. These molecules are produced in a highly-excited vibrational state.

Meanwhile it has been shown that vibrational deexcitation can be achieved by application of Raman-laser pairs [Dan08, Lan08, Osp08, Dan09, Osp09]. With this method, ultracold homonuclear Rb_2 molecules have been produced in the rovibrational ground state of the $a^3\Sigma_u^+$ electronic state [Lan08]. This method is also applicable to polar molecules, as has been demonstrated with the transfer of ultracold KRb to the rovibrational ground state of the $a^3\Sigma$ and $X^1\Sigma$ electronic states [Ni08, Osp09, Ni09]. Unfortunately, the variety of molecular species obtainable by this technique is limited: the molecules are forged together from atoms which can be efficiently laser cooled and trapped, essentially limiting this technique to homonuclear and heteronuclear alkali dimers.

Photoassociation produces molecules via optical excitation of an electronically excited molecular state during the collision of two ground-state atoms in a dense and cold atomic cloud [Let93, Mil93, Abr95, Wan96, Fio98, Pil00]. The excited molecular state may then spontaneously decay–or be transferred down by laser fields–to rovibrational states within the electronic ground-state manifold. Starting with a two-species cloud of ultracold atoms, polar molecules such as KRb, NaCs, RbCs, or LiCs can be created by photoassociation as well [Hai04, Ker04a, Ker04b, Man04, Wan04, Kra06]. However, these molecules produced by photoassociation typically populate many different rovibrational states since the molecules spontaneously decay to the electronic ground state.

To arrive at a cold molecular sample in a single rovibrational state, a laser-stimulated transfer scheme can be employed [Sag05]. Choosing a suitable rovibrational state in the electronically excited state with favorable Franck-Condon

factors, also spontaneous decay can lead to efficient decay of molecules into the rovibrational ground state [Dei08b]. The population of rovibrational states can also be redistributed by excitation with broad-bandwidth pulses. Using a suitable high-frequency cutoff, such that the rovibrational ground state is not resonantly excited anymore, population transfer to the rovibrational ground state is achieved [Vit08]. Replacing the sharp frequency cutoff by pulse-shaping techniques, even population transfer to an arbitrary selected vibrational level is possible [Sof09]. Since photoassociation demands for dense clouds of ultracold atoms to begin with, the molecular species which can be produced by photoassociation are limited to alkali dimers, same as for the Feshbach molecules.

1.2.2 Direct methods: Controlling translational and internal molecular motion

Buffer-gas cooling in a cryogenic environment was the first successful approach to produce cold polar molecules in the gas phase [Wei98]. Molecules in the gas phase are loaded into the buffer-gas cell, and then thermalize both translationally and internally by collisions with the cold helium atoms. Several methods are available to bring the molecules into the buffer-gas cell. The gas-phase molecules, in this case CaH, can be produced in the helium buffer gas cell by laser ablation from a solid target, here CaH_2. An alternative to laser ablation, increasing the flexibility concerning the available molecular species, is loading from a beam [Ego02, Ego04] or a warm capillary [Pat07, Som09, vB09]. After being cooled by collisions with the cold helium atoms, the molecules can be magnetically trapped by including a suitable magnetic-field-coil arrangement in the cryogenic setup. The trapped sample of molecules allows, e.g., studies of collision and relaxation processes [Cam07, Cam08, Hum08b, Cam09].

Buffer-gas cooling can also serve as a source for cold molecular beams [Max05]. Here, the molecules thermalize by collisions with the cold helium buffer gas, before they leave the cryogenic environment through an exit hole in the buffer-gas cell, forming a molecular beam. This extraction of cold molecules from the buffer-gas cell can be combined either with a magnetic [Pat07] or an electric [Som09, Pat09, vB09] guide, which delivers the molecules to an ultrahigh-vacuum chamber for further experiments. Advantages of the buffer-gas-cooling technique are the high fluxes of molecules which are achievable and the flexibility with respect to the used molecular species. The achievable temperature is essentially determined by the refrigerator used to cool the helium buffer-gas cell and by the requirement of a sufficiently high helium density for efficient cooling.

Stark and Zeeman deceleration apply concepts developed for the acceleration and focussing of charged particle beams to influence the motion of polar molecules. To control a polar molecule's motion, the Coulomb force acting on a charged particle is replaced by the force due to the interaction of a dipole with an inhomogeneous

electric or magnetic field [vdM08]. All these deceleration experiments employ a supersonic-expansion molecule source [Pau00]. In such a source, the temperature of the beam can be as low as a few K in the comoving frame. Additionally, the internal degrees of freedom are cooled down to low temperatures ($\approx$ 1–10 K for rotations, tens of K for vibrations). This cooling happens, however, at the cost of a high center-of-mass velocity of the molecular beam which is, depending on the used carrier gas, in the range of a few hundred m/s. Stark and Zeeman deceleration now aim at bringing these fast molecular beams to a rest in the laboratory frame.

By switching a series of high-voltage electrodes on and off in a dedicated timing sequence, a situation can be established in which the molecule looses its kinetic energy on its way along the decelerator [Bet99, Bet02]. Furthermore, also transverse focussing and transverse stability is guaranteed for the molecules moving synchronously with the switching of the electrodes. The slowed-down molecules can then be loaded into an electric trap [Bet00, Bet06], into a storage ring [Cro01] or a molecular synchrotron [Hei06, Hei07]. A variety of experiments can be performed with these decelerated and trapped molecules. These include, e.g., the lifetime measurement of the excited $^3a\Pi$ state in metastable CO [Gil07], studies of optical pumping by the thermal blackbody radiation for trapped OH and OD radicals [Hoe07], or the observation of cold collisions between decelerated OH molecules and a supersonic beam of Xe atoms [Gil06].

While a conventional Stark decelerator is a big machines, typically consisting of hundreds of electrodes which results in a total length exceeding 1 m, it was recently shown that microfabrication allows for a dramatic miniaturization. Since large electric-field gradients can be achieved with such structures, guiding and deceleration of polar molecules is possible in compact setups. For example, a total length of only 5 cm was needed to decelerate metastable CO molecules from 312 m/s to 96 m/s [Mee08, Mee09]. The need for long deceleration distances in a multi-stage Stark decelerator, relying on subsequent switching of high-voltage electrodes, can be circumvented as well by exploiting the huge electric fields reached in the light pulses produced by a mode-locked laser [Sie86]. Focussing such powerful laser pulses, the large electric field gradients which are necessary to influence the motion of polar molecules can be achieved [Sta97, Cor99, Bar01, Bar02, Don05]. This was experimentally used to decelerate pulsed atomic and molecular beams [Ful04, Ful06a, Ful06b].

It should be mentioned that not only deceleration with pulsed electric fields, i.e., Stark deceleration, is used to produce cold molecules, but other deceleration schemes exist as well. Pulsed magnetic fields are used to slow down paramagnetic atomic [Nar07b, Nar07c, Van07, Hog08a, Nar08a, Rai09] and molecular [Nar08b] beams. Hydrogen atoms, which had been slowed by such a Zeeman decelerator, were successfully loaded into a magnetic quadrupole trap [Hog08b].

One important feature of Stark and Zeeman deceleration is the tunability of the final velocity of the molecules. This offers a simple manner for adjusting the relative energy in a collision experiment, which was, e.g., successfully used in the study of the collision Xe + OH in the experiment by J. J. Gilijamse *et al.* [Gil06].

Mechanical methods have been employed as well to produce cold molecules. As in a Stark decelerator, these experiments start with cold but fast molecular beams produced in a supersonic-expansion source and try to bring these beams to a standstill in the laboratory frame. Possible configurations are mounting the nozzle of a supersonic expansion on a spinning rotor [Gup99, Gup01], billiard-like collisions between NO molecules and Ar [Eli03], and reflections of the molecular beam from clean silicon surfaces mounted on a rapidly-rotating paddle [Nar07a].

Reaching lower temperatures with molecules produced by direct means remains challenging. Typical temperatures achievable in the laboratory by Stark deceleration or buffer-gas cooling are in the 10 mK range. **Cavity cooling** is one of the proposed schemes [Hor97, Vul00, Vul01, Lev08, Wal08, Sal09] to bridge the gap from the cold to the ultracold regime with molecular samples. In contrast to free-space laser cooling, spontaneous emission is replaced by coherent scattering into the cavity mode, superseding the need for closed cycling transitions and making cavity cooling, in principle, applicable to molecules. In a coupled atom-cavity system, the cooling is achieved by choosing suitable detunings between the pump laser and the resonance frequency of the cavity. Cavity cooling [Mur06a, Mur06b] was demonstrated for atomic systems [Bla03, Cha03, Mau04, Nuß05a, Nuß05b] and allowed longer storage times of the atoms in the cavity mode. This permitted to perform very challenging and difficult experiments such as, e.g., the observation of the normal-mode splitting in a strongly coupled atom-cavity system [Mau05b, Mau05a], the realization of a deterministic single-photon server [Hij07a, Hij07b], and the demonstration of atom-photon entanglement in an atom-cavity system [Web08, Web09]. By surrounding an ion trap with an optical cavity, cavity cooling of a single trapped ion was demonstrated [Lei09]. In the resolved sideband regime, the vibrational quantum number, corresponding to the motional state of the ion in the trap, is lowered by detuning the cavity with respect to the exciting laser. The steady-state temperature is then determined by the competition between photon-recoil heating due to scattering into free space and cooling by scattering photons into the cavity. The theory of cavity cooling can be extended to include also the complex internal structure of molecules. By appropriate tuning of the pump laser and the cavity frequency with respect to molecular transition frequencies, rotational cooling of molecules via cavity-stimulated transitions should be possible [Kow07, Mor07].

Single-photon cooling [Pri08] or **opto-electrical cooling** [Zep09] are other schemes that intend to cool molecules by quantum-optical methods. In contrast to standard laser cooling, where the small photon recoil is used to iteratively transfer momentum to the atom and modify its motional state, these schemes use the spontaneous decay following optical excitation only as a mean to remove entropy. Kinetic energy is removed by exploiting the modified interaction energy with external fields when the molecule is transferred to a different internal state. Since the interaction energy of polar molecules with an externally applied electric field can be on the order of 1 K, only a small number of photon-scattering events is necessary to cool the

molecules by a substantial amount. This removes the need for fast decay rates and highly-closed cycling transitions imposed by standard laser cooling, making such schemes an attractive new approach for a wide class of polar molecules.

1.3 Approach of the Rempe group to produce cold molecules: Electric velocity filtering and guiding

In the Rempe group, a direct method for the production of cold polar molecules has been developed. It is based on the concept that any room-temperature gas contains slow–and therefore cold–molecules; they only need to be filtered out in an efficient way. This is accomplished by exploiting the Stark effect, which a polar molecule experiences in an electric field. An electric dipole placed in an inhomogeneous electric field experiences a force, the direction of the force depending on the orientation of the dipole with respect to the field direction. In a quantum-mechanical description the orientation of the classical dipole is replaced by the expectation value for the projection of the dipole moment on the field axis. This gives rise to the dependence of the Stark shift on the rotational state of the molecule. A molecule can hence be in a low-field-seeking (lfs) or high-field-seeking (hfs) state. In this thesis, only the production of beams of polar molecules in low-field-seeking states, which can be guided in electrostatic fields, is considered. The electric fields created by high-voltage electrodes connected in a quadrupolar manner allow trapping of transversely slow molecules. Selection on the longitudinal velocity is obtained by bending the guide. The selected slow polar molecules can then be guided along large distances to a separate ultrahigh-vacuum chamber [Ran03, Jun04a], where they are available for further experiments [Rie05]. However, it should be noted that also molecules in high-field-seeking states can be guided using time varying fields [Jun04b].

1.3.1 History, developments, and extensions of the electric guide

Velocity filtering using an electrostatic quadrupole guide was first demonstrated with formaldehyde (H_2CO) and deuterated ammonia (ND_3) molecules [Ran03, Jun04a]. There, fluxes of 10^{10}–10^{11} molecules/s at peak densities of $10^9\,\mathrm{cm}^{-3}$ were achieved using typical laboratory guiding fields of 100 kV/cm. The molecules in these guided beams had velocities of around 50 m/s, corresponding to a translational temperature of a few Kelvin. Since static electric fields were used in these experiments, only molecules in low-field-seeking states could be guided.

To extend the velocity-filtering technique to molecules in high-field-seeking states, a dynamical trapping potential must be created. This is accomplished by switching the electric guide between two dipolar configurations in a periodic manner. Thereby,

molecules in low-field-seeking and high-field-seeking states alike can simultaneously be trapped in a time-averaged potential. In the experiment it was shown that guiding of polar molecules in such alternating electric fields is indeed possible [Jun04b]. However, simulations suggested that only low-field-seeking molecules reached the detection volume at the exit of the guide. To show that high-field seekers can be trapped by alternating fields as well, an electric trap for neutral rubidium atoms was set up [Rie07b]. Another motivation for this experiment was the prospect of trapping atoms and molecules simultaneously in the same trap to achieve, e.g., sympathetic cooling of the molecules. To trap them, rubidium atoms are pre-cooled in a magneto-optical trap and then magnetically transferred to the all-electric trap. For these high-field-seeking rubidium atoms storage times of a few hundred milliseconds in the electric trap were demonstrated.

Since many experiments benefit from long interaction times of the molecules and, e.g., laser fields or other molecular or atomic species for the study of collisions, the electrostatic quadrupole guide was connected to an electrostatic trap for molecules [Rie05]. The trap consists of several ring electrodes which match in a natural way to the electric quadrupole guide. With this continuously-loadable trap, storage times of 130 ms at temperatures of 300 mK were demonstrated for ammonia molecules. The lifetime of the molecules in this trap is limited by the probability of finding an escape channel, given by either the exit or entrance quadrupole guide. This results in a velocity-dependent lifetime of molecules in the trap since fast molecules probe the surface enclosing the trap volume more rapidly. This opens the perspective of reaching longer storage times by a more elaborate design of an electrostatic trap for polar molecules.

In the first guiding experiments molecular species such as formaldehyde or ammonia were used. A polar molecule which is of high interest to different fields is water. However, due to its molecular structure, ordinary (H_2O) and fully-deuterated (D_2O) water exhibits quadratic Stark shifts. Therefore, guiding and trapping is significantly more challenging than with formaldehyde or ammonia which exhibit large, linear Stark shifts. Nevertheless, with the electrostatic guiding and velocity-filtering technique cold guided beams of deuterated water (D_2O) could be produced, showing the versatility of this method [Rie06]. Recently, these experiments with cold guided water beams were extended to include all the water isotopologues H_2O, D_2O, and HDO [Mot09b]. Although seeming very similar at a first glance, these molecules show a distinct behavior when exposed to the guiding electric fields. This allowed to investigate different aspects of the velocity-filtering process such as its dependence on rotational states of the polar molecules.

The flux of cold guided polar molecules is so high that it is easily detected with a quadrupole mass spectrometer (QMS). This has the additional advantage of being robust and flexible. However, with this measuring technique no direct information on the population of internal states of the molecules is available. Therefore, the detection with the QMS was combined with a laser-spectroscopy technique [Mot07]. In the guide, formaldehyde (H_2CO) molecules were optically pumped to an excited

state which dissociates rapidly. If this optical pumping is done in a state-dependent way, the laser-frequency-dependent decrease of the QMS signal allows to infer information on populations of individual rotational states of the guided molecules. In principle, this technique is applicable to other species as well since coupling to an unguided state is sufficient to generate losses from the guided population.

In all experiments mentioned so far the molecules were extracted from a thermal reservoir which could, at most, be cooled to 150 K. The source would, however, benefit a lot from starting with an ensemble already at cryogenic temperatures. Therefore, electrostatic velocity filtering was recently combined with buffer-gas cooling [Som09, Pat09, vB09]. Here, molecules are injected into a cryogenic helium buffer gas through a heated input capillary. The molecules thermalize by collisions with the cold helium atoms [Wei98], and finally leave the buffer-gas cell through an exit aperture [Max05, Pat07, Som09, Pat09, vB09]. This beam leaving the cell is then collected by the electric guide. With this setup, guided beams with densities of $10^9\,\mathrm{cm}^{-3}$ and fluxes of 10^{11} molecules/s at velocities of 60 m/s are produced. By collisions with the cold helium buffer gas not only the translational degrees of freedom, but also internal excitations are cooled. With the depletion-spectroscopy technique for formaldehyde it could be verified that the rotational degrees of freedom are cooled down to the temperature of the buffer gas, 4 K, resulting in a state-selected beam with at least 80 % of the population in a single rotational state.

1.4 This thesis

This thesis focusses on the properties of cold guided beams of polar molecules produced by electrostatic velocity filtering. Main questions, which are addressed, are, how the internal-state distribution influences experiments with guided molecules, how it is experimentally observable, and how it can be altered and cooled down. In **chapter 2** the working principle of electrostatic velocity filtering and guiding is explained, and the setup used for the experiments is presented. Measurements with deuterated ammonia (ND_3) molecules are discussed, which shine a new light on the detection process. More specifically, the question "what is actually measured?" is addressed, an issue of highest relevance for calibrations of the flux of guided molecules [Ran03, Jun04a, Som09, vB09]. In **chapter 3** measurements with deuterated ammonia (ND_3), which have been performed over a wide range of inlet pressures, are presented. The results show that collisional effects in the vicinity of the nozzle must not be neglected, although the source is operated in the near-effusive regime [Mot09a]. These collisions ultimately limit the flux of cold molecules achievable by electrostatic extraction of molecules from a thermal reservoir. Therefore, an optimization of the source for future experiments requires profound knowledge of these effects. In **chapter 4** guiding experiments performed with the different water isotopologs H_2O, D_2O, and HDO are presented. Although these molecules are very similar concerning their chemical properties, they show a surprisingly different be-

havior in the velocity-filtering process [Mot09b]. An explanation is found from the theoretical model of electrostatic velocity filtering and guiding. According to this model, the guiding efficiency essentially depends on a favorable Stark shift. These molecular Stark shifts are related to the rotational level structure and symmetry properties of the considered molecules. Since the individual water isotopologs have a specific rotational energy-level structure, these differences in their guiding efficiencies hint at the importance of the internal-state distribution for a proper description of the velocity-filtering process. Depletion spectroscopy of formaldehyde, which is presented in **chapter 5**, provides direct access to the internal-state distribution of molecules in the guided beam. To address individual rotational states, a detailed understanding of the formaldehyde spectrum is necessary. With molecular constants obtained from the analysis of room-temperature absorption spectra, assignment of the observed transitions to rotational states is possible. Since formaldehyde molecules dissociate following ultraviolet excitation, a loss of molecules from the guided beam, i.e., a depletion in the detector signal, is induced. This depletion is a measure for the population of the addressed internal state and is used to characterize the internal-state distribution in the guided beam. In **chapter 6** the enhancement of Rayleigh scattering by an optical cavity is discussed [Mot09c]. Such cavity-enhanced light scattering might be used as a non-destructive detection scheme for ultracold molecules. The results of this thesis work open new roads for future experiments with cold polar molecules, which are illustrated in the outlook given in **chapter 7**.

Chapter 2

Electrostatic velocity filtering and guiding of polar molecules

In the 1950's, Zacharias *et al.* made efforts to produce slow atoms and molecules for high-precision spectroscopy by directing an effusive beam upwards in a kind of fountain [Zac54, Ram90]. The slow molecules were expected to reverse their travel direction in the gravitational field of the Earth already after ascending a small height, such that they could be detected at the base of the fountain. However, no slow molecules could be observed. The explanation for this is twofold: First of all, after leaving the effusive source, the beam dilutes by spreading out, so that the density of reversed molecules at the detector is very small. Second, on their way up, the slow molecules are permanently bombarded by fast molecules from behind. In these collisions the slow molecules gain so much energy and momentum in forward direction that finally the number of slow molecules is so low that none can be detected.

Notwithstanding the experiences with the Zacharias fountain, it is possible to obtain slow molecules by velocity filtering. The filtering efficiency of the slowest molecules from an effusive source can be improved decisively by a number of measures. One is, of course, improved technology in terms of better detectors and a better vacuum. But, more importantly, it is crucial to prevent the molecules from spreading transversely by an appropriate guiding structure. This can be achieved with a magnetic guide for paramagnetic atoms and molecules which possess unpaired electrons [Gha99, Pat07]. For polar molecules, which possess a permanent electric dipole moment, electric guides are better suited. A schematic representation of an experimental setup for velocity filtering by such an electric guide is shown in Fig. 2.1. By providing an electric field which increases in all transverse directions, molecules in low-field-seeking states, i.e., those with a positive Stark shift, will be guided if their transverse velocity is small enough. Moreover, a bend in the guide offers two additional advantages: First, the longitudinal velocity is also limited, since the centripetal force supplied by the electric field only guides molecules around the corner if their longitudinal velocity is small enough. Second, a bend in the guide extracts

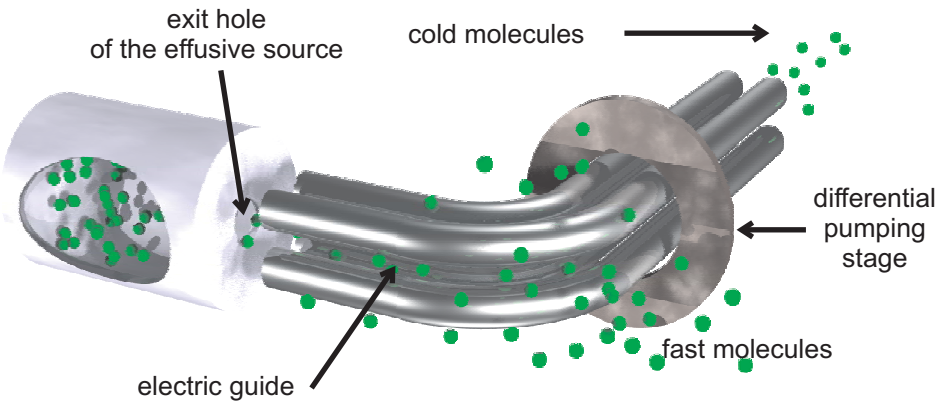

Figure 2.1: Schematic of the electrostatic velocity-filtering and guiding experiment. Molecules leave the effusive source through the exit hole and are funneled into the electric quadrupole guide. The guiding electric fields provide a two-dimensional trapping potential for transversely slow molecules, whereas filtering on longitudinal velocity is achieved by bending the guide. The slow, and hence cold, molecules are guided through differential pumping stages to an ultrahigh-vacuum region, where they are available for further experiments.

the slow molecules from the region where collisions with fast molecules from behind are most likely. The molecules are brought rapidly into an ultrahigh-vacuum region, where collisions are rare. These guiding ideas were successfully implemented in the Rempe group in the past years to create high-flux beams of slow polar molecules [Ran03, Jun04a, Rie06, Mot09a, Mot09b].

2.1 Theory of electrostatic velocity filtering of polar molecules

Velocity filtering of polar molecules is based on selection of the slowest molecules from a thermal gas, as schematically shown in Fig. 2.2. An electric guide collects slow molecules leaving an effusive source in an efficient way by accepting a large solid angle. Although, according to the Maxwell-Boltzmann velocity distribution, the relative fraction of slow molecules with energies below 1 K is only 10^{-4} for a thermal gas at room temperature, the absolute density of slow molecules can be quite high, when starting with sufficiently high gas density.

Using suitable electric-field gradients, forces can be exerted on polar molecules. The guiding and trapping potential for slow molecules is realized in the form of an electric quadrupole field, which is created by four high-voltage electrodes. Electrical fields achievable in the laboratory are on the order of 100 kV/cm. This results in trap depths on the order of a Kelvin for typical molecular Stark shifts of $\approx 1\,\mathrm{cm}^{-1}$ at these fields. Transversely slow molecules in low-field-seeking states are trapped within the region enclosed by high electric fields, whereas fast molecules escape the

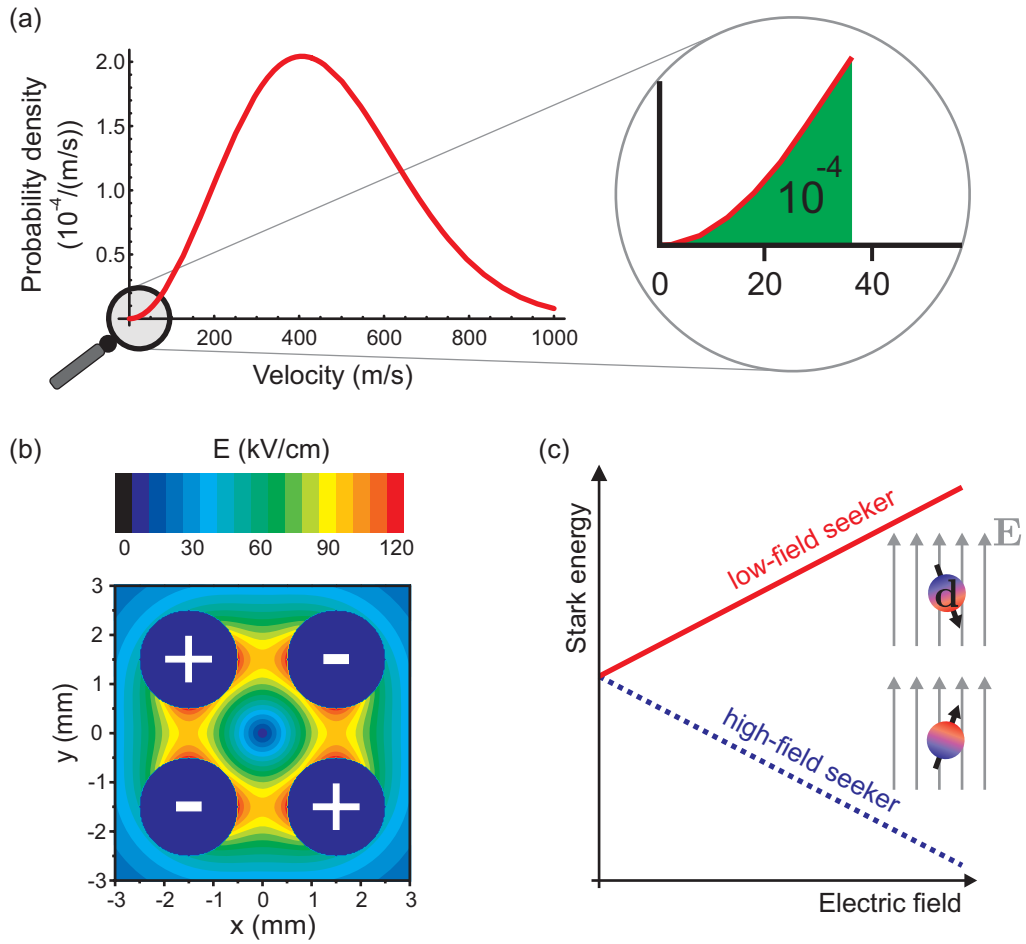

Figure 2.2: Idea of electrostatic velocity filtering. (a) Thermal velocity distribution of ammonia (ND_3) molecules. A considerable fraction, 10^{-4}, of the molecules has a velocity below $\approx 35\,\mathrm{m/s}$, corresponding to 1 K. (b) Electric-field distribution in the quadrupole guide for $\pm 5\,\mathrm{kV}$ electrode voltage. In the center an electric-field minimum is formed, surrounded by fields rising to at least $93\,\mathrm{kV/cm}$ in all directions. (c) Stark energy of an electric dipole. Depending on the orientation of the electric dipole moment **d** with respect to the external electric field **E**, the molecule will minimize its energy at small electric fields (low-field seekers, lfs) or high electric fields, respectively. Molecules in lfs states can be trapped and guided in a quadrupole potential such as the one shown in (b).

guide. Filtering on longitudinal velocity is achieved by bending the guide. When the centrifugal force exceeds the restoring force of the guiding quadrupole field, the fast molecules cannot follow the guide and are lost.

The total flux of guided molecules can be calculated from the number of molecules in the source which are in a guidable internal state and which have a sufficiently low energy to be trapped in the potential created by the electric fields. In the following, this flux of guided molecules is calculated for just one internal molecular state with a fixed Stark shift. The extension to a variety of states is then discussed in chapter 4.

2.1.1 Velocity distributions in the thermal source

Before calculating the flux of guided molecules, the velocity distributions of molecules in the thermal reservoir, from which they are extracted, must be considered. These are given by a three-dimensional (3D) Maxwell-Boltzmann velocity distribution

$$f_{3\mathrm{D}}(v)\,\mathrm{d}v = \frac{4}{\sqrt{\pi}\alpha^3}\,v^2\,\exp(-v^2/\alpha^2)\,\mathrm{d}v \tag{2.1a}$$

and by a one-dimensional (1D) velocity distribution

$$f_{1\mathrm{D}}(v_{x,y,z})\,\mathrm{d}v_{x,y,z} = \frac{1}{\sqrt{\pi}\alpha}\,\exp(-v_{x,y,z}^2/\alpha^2)\,\mathrm{d}v_{x,y,z} \tag{2.1b}$$

with most probable velocity $\alpha = \sqrt{2k_BT/m}$, velocity components v_i $(i = x, y, z)$ and total velocity $v = \sqrt{v_x^2 + v_y^2 + v_z^2}$.

2.1.2 Cutoff velocities in the electric guide

As was already described qualitatively in the introduction to this section, the flux of guided molecules is given by the part of the molecules injected into the guide with velocities below certain transverse and longitudinal cutoff velocities. These cutoff velocities depend on the Stark shift of the molecules, their mass m, and on the properties of the guide. The maximal transverse velocity $v_{\max} = \sqrt{2\Delta W^{\mathrm{s}}/m}$ is determined by the Stark shift $\Delta W^{\mathrm{s}}(E_{\max})$ reached at the maximum of the trapping field $E_{\max}$. If the transverse velocity $v_\perp = \sqrt{v_x^2 + v_y^2}$ of the molecule exceeds $v_{\max}$, it is lost from the guide. The maximal longitudinal velocity $v_{\mathrm{l,max}}$ can be obtained by equating the centrifugal force in the bend of radius R and the restoring force of the guide, resulting in $v_{\mathrm{l,max}} = \sqrt{\Delta W^{\mathrm{s}}(E_{\max})R/r\,m} = \sqrt{R/2r}\,v_{\max}$. Here, r is the free inner radius of the guide, at which the maximum of the trapping field is reached. In the used setup, the diameter the guide's electrodes is 2 mm, and the distance between neighboring electrodes is 1 mm. This results in r=1.12 mm. As almost every particle is guided if $v_{\mathrm{l}} < v_{\mathrm{l,max}}$ and $v_\perp < v_{\max}$, this yields higher efficiencies as compared to filtering by, e.g., rotating filter wheels and apertures.

2.1.3 Flux of guided molecules

To calculate the flux of guided molecules, the velocity distributions of molecules entering the guide from an effusive source are integrated to the cutoff velocities. In the limit of small cutoff velocities $v_{\max}$ and $v_{\mathrm{l,max}}$ compared to the thermal velocity α, the exponential $\exp(-v^2/\alpha^2)$ in the thermal velocity distributions Eq. (2.1) can be replaced by 1. Then, the flux Φ of guided molecules in a molecular state with a Stark energy ΔW^{s} is given by

$$\begin{aligned}\Phi &= \int_{v_x=-v_{\max}}^{v_{\max}} \int_{v_y=-v_{\max}}^{v_{\max}} \int_{v_z=0}^{v_{\mathrm{l,max}}} f_{\mathrm{1D}}(v_x) f_{\mathrm{1D}}(v_y)\, v_z\, f_{\mathrm{1D}}(v_z)\, \mathrm{d}v_x \mathrm{d}v_y \mathrm{d}v_z \\ &\propto v_{\max}^4 \propto (\Delta W^{\mathrm{s}})^2,\end{aligned} \tag{2.2}$$

where the dependence of the transverse velocity on the longitudinal cutoff velocity is neglected, and Φ is normalized to the flux of molecules out of the nozzle. The guided flux can hence be described by a function f which gives the fraction of guidable molecules for a given electric field, $\Phi = f(\Delta W^{\mathrm{s}}) \propto (\Delta W^{\mathrm{s}})^2$.

2.2 Experimental setup

The setup used for the experiments presented in this thesis is already described in [Mot09a, Mot09b]. Many parts of the setup, especially the quadrupole guide, are similar to or adopted from the ones used in the Rempe group for previous experiments and described in the thesis of Tobias Junglen [Jun05]. The quadrupole guide for polar molecules is located in three interconnected ultrahigh-vacuum chambers, as shown schematically in Fig. 2.3. The guide consist of four stainless-steel electrodes with a diameter of 2 mm, which are arranged in a quadrupole configuration. The individual electrodes are clamped to a ceramic insulator mount, which also maintains a spacing between adjacent electrodes of 1 mm. Applying voltages of ± 5 kV results in an electric field minimum in the center surrounded by trapping electric fields exceeding 93 kV/cm in all directions.

Molecules are continuously injected into the guide through a ceramic tube (⌀ 1.5 mm, length 9.5 mm) which is connected to a liquid-nitrogen reservoir and equipped with a heater element, such that its temperature can be adjusted in the range 100–400 K. To ensure thermalization, the Teflon tube for the molecular gas passes a meandering cooling stage of ≈ 0.3 m length before entering the ceramic tube. Through the rest of this thesis this ceramic tube with the attached cooling stage, which is schematically shown in Fig. 2.4 (a), is shortly called "nozzle". Figure 2.4 (b) shows the gas-handling system used to supply the molecular gas to the nozzle. By cooling the nozzle, the fraction of slow molecules increases, as the Maxwell-Boltzmann velocity distribution gets compressed and shifted to lower velocities. This increases the guided flux. Furthermore, the number of thermally occupied states is reduced,

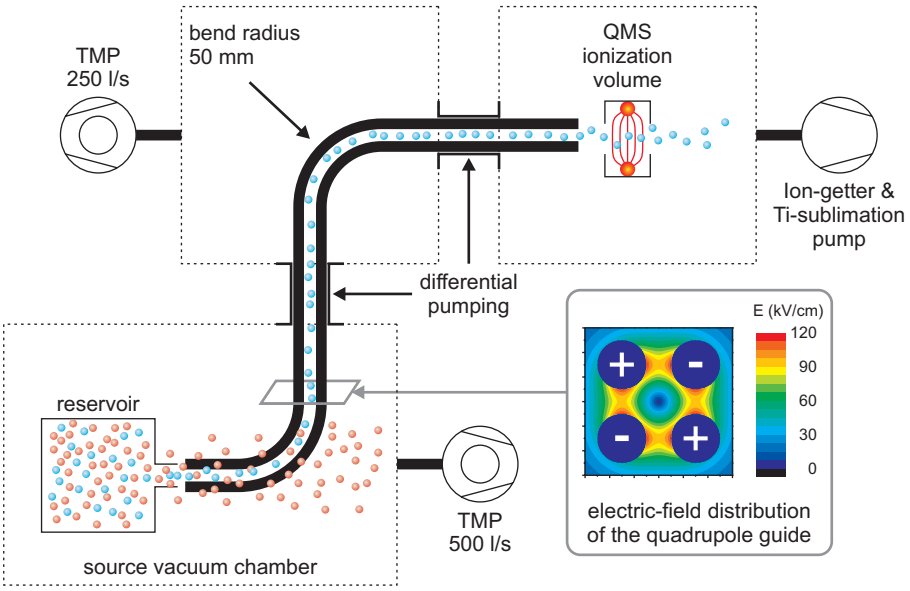

Figure 2.3: Experimental setup. Molecules from the thermal reservoir enter the electric guide through the ceramic nozzle. Slow molecules are trapped in the quadrupole field and guided through two differential pumping stages to an ultrahigh-vacuum chamber, where they are detected by the quadrupole mass spectrometer (QMS). The inset shows the electric-field distribution of the quadrupole guide for $\pm 5\,\mathrm{kV}$ electrode voltage, resulting in a trapping electric field exceeding $93\,\mathrm{kV/cm}$.

leading to an improved purity of the guided beam as shown by depletion spectroscopy [Mot07]. The nozzle is located in a vacuum chamber, in which a base pressure of $10^{-9}\,\mathrm{mbar}$ is achieved by a $500\,\mathrm{l/s}$ turbo molecular pump (TMP). When flowing gas, the pressure in the chamber rises to a typical value of a few $10^{-7}\,\mathrm{mbar}$. From this pressure rise and the known pumping speed the gas flow rate through the nozzle can be determined. For a typical reservoir pressure of $0.1\,\mathrm{mbar}$, which is used for many experiments, the gas flow rate through the nozzle is $1 \times 10^{-4}\,\mathrm{mbar{\cdot}l/s}$.

Compared to previous experiments, where a bend radius of $25\,\mathrm{mm}$ [Ran03, Jun04a] or only $12.5\,\mathrm{mm}$ [Rie05] was used, the current setup employs a larger bend radius of $50\,\mathrm{mm}$. This has the advantage of an increased flux, which is especially valuable when looking for small signals as, for instance, when performing experiments at very low reservoir pressure such as the ones described in chapter 3. The increase in flux is also very valuable for measurements with molecules exhibiting quadratic Stark shifts such as H_2O or D_2O [Mot09b], which are discussed in chapter 4, or when doing differential measurements such as in depletion spectroscopy [Mot07, vB09] presented in chapter 5. The molecules are guided around two bends and through two differential pumping stages to an ultrahigh-vacuum chamber, where they are finally detected by a quadrupole mass spectrometer (QMS, Pfeiffer QMG422). In the QMS, the guided molecules are ionized by electron impact in a cross-beam geometry. The ions are then mass filtered, before in the final stage single-ion counting using a secondary-electron

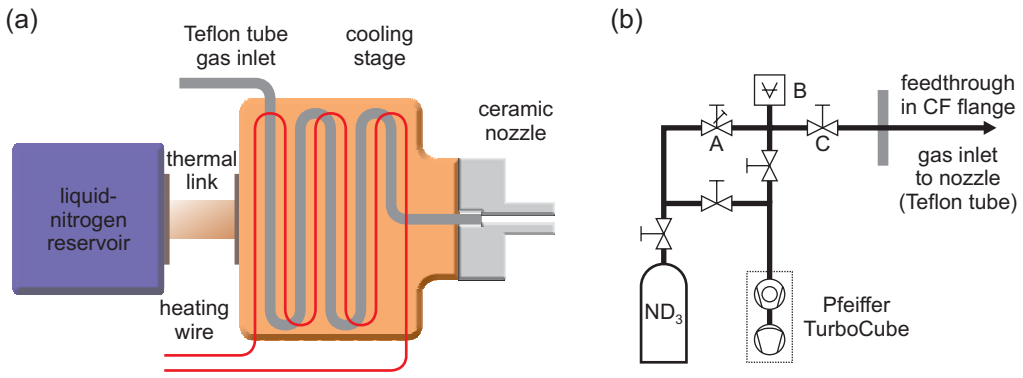

Figure 2.4: Gas-inlet system. (a) Nozzle assembly. The Teflon tube, through which the molecules are brought to the ceramic nozzle, meanders in the copper cooling stage for thermalization of the molecular gas. The temperature of the copper block is controlled by balancing the current through the heating wire with the thermal link to the liquid-nitrogen reservoir. In the experiments, temperatures in the range 150–300 K are used. To maintain a reasonable molecule flux out of the nozzle, a sufficiently high gas pressure is necessary. This limits the lowest operable temperature by the temperature dependence of the vapor pressure. (b) Gas from an ammonia (ND_3) bottle is supplied to the nozzle. The gas-handling system, consisting of stainless-steel tubes, is evacuated with the TurboCube to a pressure below 10^{-4} mbar before the molecular gases are introduced. A: Thermoelectrically-controlled flow valve. B: Pressure gauges (Pirani and Membrane). C: In-line valve, separating the UHV feedthrough from the gas-handling system.

multiplier is performed. The electronic signals are amplified, shaped to standard 0–5 V TTL pulses, passed through an isolating amplifier to avoid ground loops, and are finally recorded using a multichannel scalar card. This detection of the guided molecules by the QMS is not sensitive to the internal states. However, by combination with ultraviolet laser spectroscopy in the guide, state-sensitive detection can be achieved [Mot07]. The application of this depletion-spectroscopy technique to internal-state diagnostics in cold guided beams of formaldehyde is discussed in chapter 5.

2.3 Velocity-filtering experiments

The electrostatic velocity-filtering and guiding experiments are performed as a series of time-of-flight (TOF) measurements. Here, the high voltage (HV) applied to the electrodes, which produces the guiding quadrupole field, is switched on and off in a fixed timing sequence. Figure 2.5 shows a typical time-resolved signal measured with the QMS. The signal of guided molecules is determined from the difference in the steady-state QMS signal with HV applied to the guide and HV switched off, which permits subtracting contributions of background gas to the QMS signal.

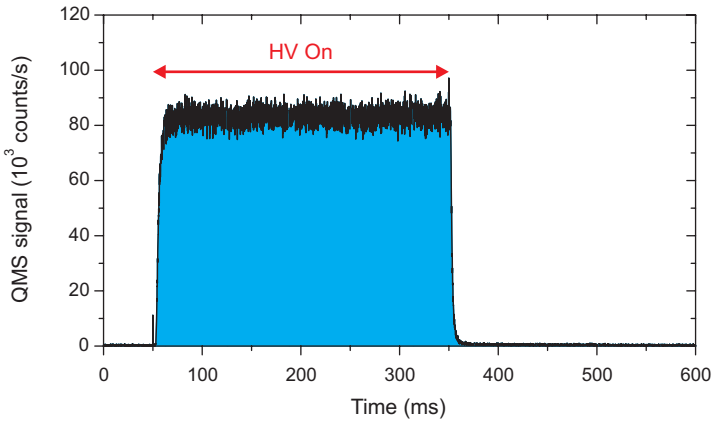

Figure 2.5: Time-resolved QMS signal. After applying high voltage (HV) to the guide's electrodes (at $t = 50\,\mathrm{ms}$), the signal rises and finally reaches a steady-state value. The density of guided ammonia (ND_3) molecules arriving at the QMS ionization volume is proportional to this steady-state value.

Figure 2.6 allows a closer look at the rising edge of the time-resolved QMS signal. In this figure, measurements for different electrode voltages are compared. The first feature to observe is the dependence of the steady-state value on the electrode voltage. This steady-state value is proportional to the density of guided molecules arriving at the QMS ionization volume, as will be shown in section 2.4. In section 2.1 it was explained that the flux and hence also the density of the guided molecules increases with the trap depth provided by the guide, i.e., with the electrode voltage. A detailed analysis of this steady-state signal of guided molecules allows insight into the dependence of the electrostatic guiding and velocity filtering on the molecular properties, as is discussed later on using the example of the different water isotopologs in chapter 4. As a second characteristic, the arrival time of the molecules can be considered. After switching on the guiding electric fields, it takes a while until the QMS signal starts rising, i.e., until the first molecules arrive. This delay corresponds to the time of flight of the fastest molecules from the nozzle to the QMS detection volume. Since the minimum time of flight is given by the longitudinal cutoff velocity, a dependence on the applied electrode voltage is observed. For increasing electrode voltage, the trap depth and, as a consequence, also the longitudinal cutoff velocity increases.

2.4 The flux-density mystery

In the preceding section 2.3 a short introduction to measurements with the electrostatic guide was given. However, one key question was not addressed so far: What is actually measured by the quadrupole mass spectrometer (QMS), which constitutes the detector for the cold guided molecules? For a uniform gas in thermal equilibrium

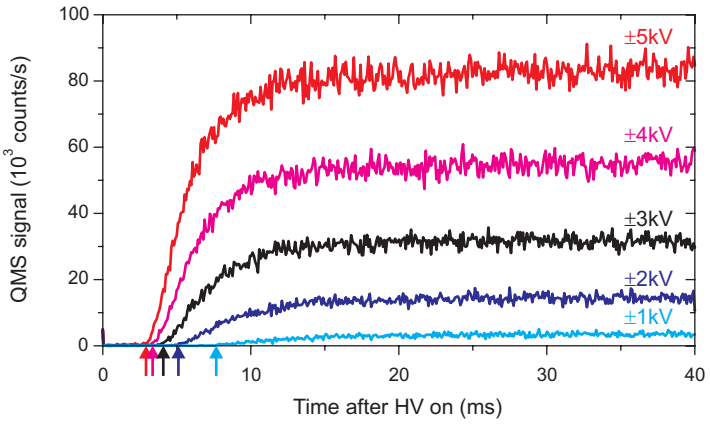

Figure 2.6: Time-resolved QMS signal for different electrode voltages. After switching on the guiding electric fields (at $t = 0$ ms), the QMS signal rises with a delay time, indicated by small arrows. This delay corresponds to the time of flight of the fastest guided ammonia (ND_3) molecules from the nozzle to the detector, which is determined by the longitudinal cutoff velocity. Finally, the signal reaches a steady-state value. The steady-state value, as well as the longitudinal cutoff velocity (observed via the arrival time of the fastest molecules), increases with the trapping electric field produced by the applied electrode voltage, as discussed in section 2.1.

a quadrupole mass spectrometer, which is nothing else but a residual-gas analyzer, measures the gas density [Wut04, dH08]. Figure 2.7 (a) shows schematically how the beam of cold molecules leaves the quadrupole guide and passes through the ionization volume of the QMS. In this configuration a maximal detector signal of guided molecules is obtained. However, it is a priori not clear if the QMS signal corresponds to the number density of molecules, since the molecules pass through the ionization volume with a preferred direction and forward velocity. For instance, a velocity-dependent saturation of the ionization yield might occur and lead to deviations from a density measurement and could even result in signals resembling a flux measurement.

To distinguish whether the QMS signal in this measurement configuration is proportional to the density or the flux (or probably something different) of guided molecules, it would be desirable to have a detector available with an output signal proportional to either the true flux or density of guided molecules. Optical absorption spectroscopy would allow a measurement of the optical density and hence of the number density of guided molecules. However, due to the limited densities in the guide as compared to the ones in typical molecular-beam spectroscopy experiments, this would be very challenging. Fortunately, a true flux measurement is possible with the QMS positioned out of the direct line of sight of the molecules leaving the guide in the detection chamber, as will be explained along the following lines. For this, the steady-state situation in the detection chamber is considered, as shown schematically in Fig. 2.7 (b). As can be seen from Fig. 2.6, already ≈ 20 ms after

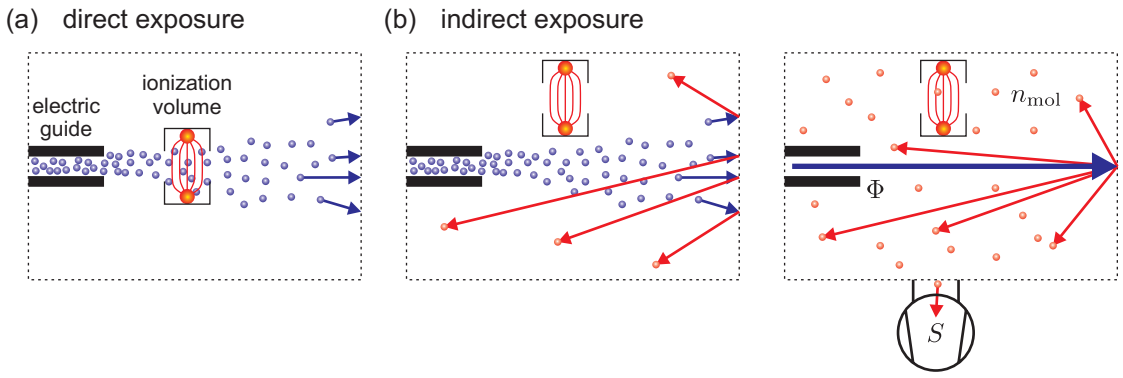

Figure 2.7: Detection of cold guided molecules by the QMS. (a) The QMS ionization volume is placed directly in the beam leaving the electric quadrupole guide for maximal detector signals. (b) The QMS ionization volume is placed out of the line of sight onto the beam of guided molecules. The molecules leave the guide, travel through the vacuum chamber, and finally thermalize by collisions with the walls. The steady-state number density n_{mol} of molecules in the detector chamber is given by the balance between the incident flux of molecules Φ and the pumping speed S. In this configuration the detector signal is therefore proportional to the flux of guided molecules.

switching on high voltage the electrostatic guide delivers a constant flux Φ of cold molecules into the detection chamber. These molecules thermalize by collisions with the walls of the vacuum chamber. The vacuum pump with a constant volume pumping speed S acts as a drain for these molecules accumulating in the vacuum chamber. In a steady state, the density n_{mol} of molecules is given by the balance between the incident flux of guided molecules into the detection chamber and the pumping speed, $n_{\mathrm{mol}} = \Phi/S$. By moving the QMS ionization volume out of the direct line of sight onto the guided beam, it can be operated as a residual-gas analyzer which monitors the increase of background gas density due to the cold molecules guided into the detection chamber. These molecules contributing to the background gas have thermalized by collisions with the wall, such that their velocity does not depend on the velocity of the molecules in the guided beam. Instead, their velocities are described by a uniform thermal velocity distribution. Since the QMS measures a density n_{QMS} for such a uniform gas distribution, one expects to find $n_{\mathrm{QMS}} = n_{\mathrm{mol}} \propto \Phi$, which results in a signal proportional to the flux of guided molecules into the detection chamber. Therefore, such a measurement without direct exposure of the QMS ionization volume to the guided beam displays the same parameter dependence as a flux measurement performed directly in the guided beam.

Figure 2.8 compares the electrode-voltage dependence of the QMS signal with direct exposure of the ionization volume to the beam of guided molecules to measurements with the ionization volume moved out of the direct line of sight, entitled indirect exposure. All data shown are normalized to the measured value at $\pm 6\,\mathrm{kV}$ electrode voltage. On an absolute scale, however, the count rates with direct expo-

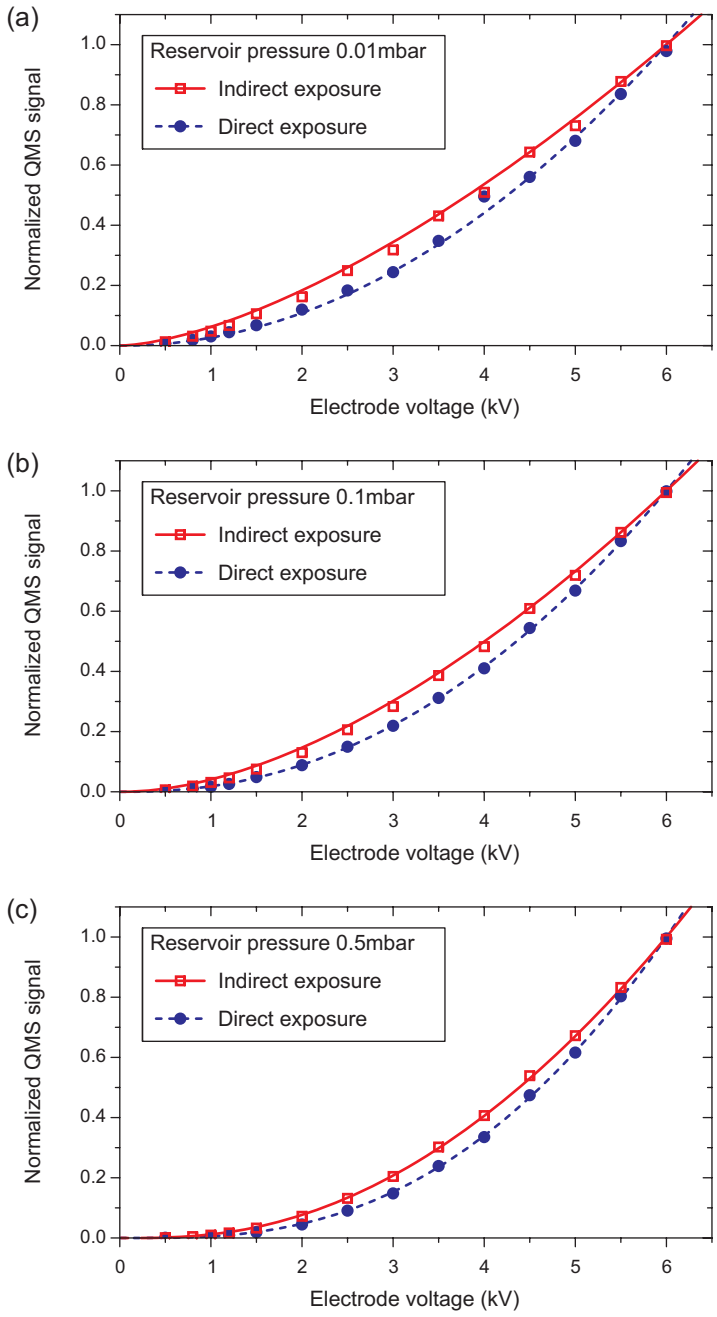

Figure 2.8: Measurements with direct and indirect exposure of the QMS ionization volume to the beam of guided ammonia (ND_3) molecules. With indirect exposure the electrode-voltage dependence of the flux of guided molecules is measured. The solid curve is a fit based on the model of velocity filtering described in section 3.3. The difference between direct and indirect exposure excludes the possibility of a flux measurement when the QMS ionization volume is directly exposed to the beam of guided molecules. The dashed curve are the model's predictions for the density of the molecules in the guided beam based on the fit values obtained from the flux measurement with indirect exposure.

sure are larger by a factor on the order of 100. A clear difference between the two types of measurements is observed. The measurement with the indirect exposure of the QMS to the guided beam, i.e., measuring the steady-state background-gas density caused by the guided molecules, shows the dependence of the flux of guided molecules on the electrode voltage as explained in the preceding paragraph. Due to the different electrode voltage dependence between direct and indirect exposure it can be ruled out that the QMS signal under direct exposure is proportional to the flux of guided molecules.

In section 3.3 a model will be developed for the electrode-voltage dependence of the signal of guided molecules taking into account collisions during the beam-formation process. The solid curves in Fig. 2.8 are fits of this model to the data taken with indirect exposure of the QMS ionization volume to the guided beam. Here, a flux measurement is assumed. To resolve the nature of the QMS signal under direct exposure of the QMS ionization volume to the guided beam of cold molecules, this measurement is used as a reference. Then, based on these fit values obtained from the flux measurement with indirect exposure, the model for the electrode-voltage dependence of the density of the guided beam is evaluated. For this, an additional factor $\sqrt{U} \propto v$ for the difference between the flux and the density of the guided beam is included, as will be discussed in section 3.3. The dashed curves are the predictions of this model for the electrode-voltage dependence of the density of guided molecules. The good agreement, independent of the reservoir pressure and hence the exact properties of the guided beam, confirms that indeed a density measurement is performed when the ionization volume is directly exposed to the guided beam, as is done for all the measurements discussed in this thesis unless otherwise stated.

2.5 Velocity distribution of guided molecules

To obtain additional information on the guided beam of polar molecules, a velocity distribution can be constructed from the time-resolved QMS signal. For that purpose, the arrival-time distribution of the molecules is analyzed. After switching on the high voltage the QMS signal rises to a steady-state value, as shown in Fig. 2.9. The height of this steady-state signal was used for the measurements discussed so far. However, more information about the guided beam can be obtained from this time-of-flight (TOF) signal. For this, the velocity of the molecules is calculated from the arrival times at the detector. For a given time t after switching on the guiding fields, molecules with velocities $v \geq d/t$ contribute to the signal, where d is the total length of the electric guide. Then, a binning of these velocities with a bin width of typically 5 m/s is applied. This value is chosen as a compromise between resolution and sufficient signal-to-noise ratio. In a next step, a post selection is applied to the data. As can be seen from the TOF trace in Fig. 2.9, the signal has already closely approached the steady-state value for late arrival times, corresponding to

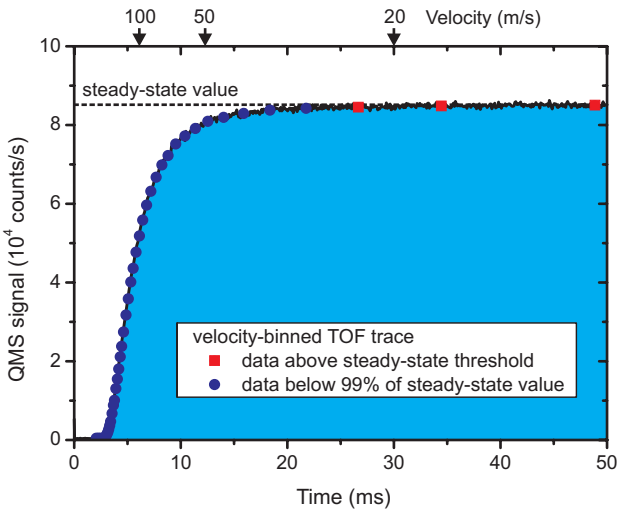

Figure 2.9: Time-of-flight trace of guided ammonia (ND_3) molecules. After switching on the high voltage applied to the guide's electrodes at $t = 0$ ms, the signal rises and finally reaches a steady-state value. To derive a velocity distribution, velocity-dependent count rates are calculated from the arrival times and binned with a resolution of 5 m/s (blue points). To avoid systematic effects, data above a given threshold of the steady-state value are dropped (red squares).

low velocities. These data might therefore be more affected by systematic errors, since a small effect on the count rate could already lead to a big difference in the velocity distribution. To avoid systematic effects, all the data above a given threshold, typically 99 %, of the steady-state value, is not considered in the evaluation of the velocity distribution. The exact value of this threshold can slightly influence the lowest-velocity data point. To finally derive a velocity distribution as the one shown in Fig. 2.10, a discretized differentiation is applied to the velocity-binned TOF trace (blue data points in Fig. 2.9).

Figure 2.10 shows a typical velocity distribution of guided ammonia (ND_3) molecules constructed from the time-resolved QMS signal. This distribution reflects, however, the velocity of molecules arriving at the detector, which is placed ≈ 2 cm behind the exit of the guide, and not directly the velocity of the guided sample. When leaving the guiding electrode structure, the beam of slow molecules spreads out [Jun04a, Som09]. Since the transverse extent of the ionization volume (Pfeiffer Vacuum specifies a volume of $\approx 2 \times 2 \times 2$ mm) is smaller than the spread of the molecules at this distance from the guide exit, the probability to enter the active volume of the detector increases with the molecules' velocity in forward direction. This causes a rise with velocity in the velocity distribution. In contrast, for a density measurement performed in the guide the velocity distribution would be constant from small velocities up to the maximum in the distribution. The slow decrease instead of a sharp cutoff on the high velocity side is caused by the contribution of several internal states with different Stark shifts and therefore different cutoff ve-

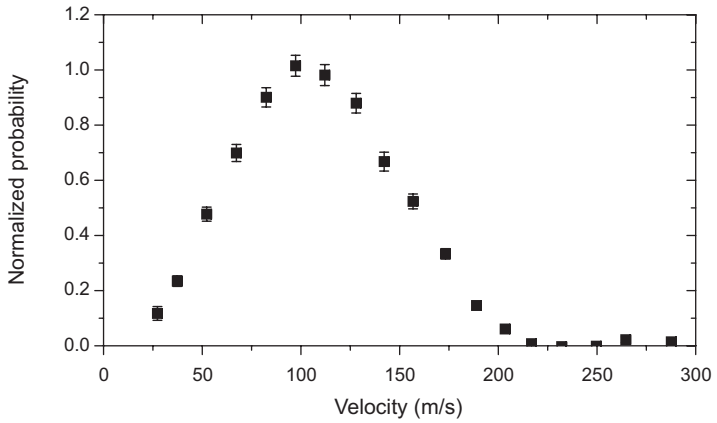

Figure 2.10: Velocity distribution of guided ammonia (ND_3) molecules arriving at the QMS ionization volume. The cutoff velocity, i.e., the velocity of the fastest molecules which can still be guided, is determined by the bend radius of the electrostatic quadrupole guide and by the Stark shifts of the molecular states populated in the guided beam.

locities to the guided beam, as well as by the dependence of the longitudinal cutoff velocity on the transverse velocity of the molecules [Jun04a].

The mean velocity of the guided beam in longitudinal direction is $v_z \approx 100\,\mathrm{m/s}$. This corresponds to a one-dimensional translational temperature of T of 12 K, using $E = mv_z^2/2 = k_B T$. For the molecules in the guide the transverse velocity is smaller, $v_\perp = \sqrt{2r/R} \approx 20\,\mathrm{m/s}$ as shown in section 2.1. Using $\langle v \rangle = \sqrt{v_z^2 + v_\perp^2}$ and $E = m\langle v \rangle^2/2 = 3/2\ k_B T$ a three-dimensional translational temperature of 8 K is obtained. These temperatures seem relatively high compared to previous results. As shown by T. Rieger *et al.*, molecules from a similar electrostatic guiding and velocity-filtering setup could be loaded into an electrostatic trap with a trap depth corresponding to a temperature of only 300 mK [Rie05]. It should, however, be noted that the temperatures derived above only represent the mean of the guided molecule sample. Due to the nature of the velocity-filtering process, also slower and hence colder molecules are present in the beam of guided molecules. Additionally, in the present setup a relatively large bend bend radius of 50 mm is used, which is beneficial in terms of total flux of guided molecules for experiments aiming at guiding of molecules with smaller Stark shifts. For species with relatively large Stark shifts such as deuterated ammonia (ND_3) or formaldehyde (H_2CO) this results in a higher temperature of the guided molecules.

Chapter 3

Collisional effects in the formation of cold guided beams of polar molecules

In this chapter, the influence of the beam-formation process on electrostatic velocity filtering and guiding is investigated. In a typical experiment, the flux of guided molecules can be increased by raising the pressure of the gas in the reservoir and thereby the number of molecules injected into the guide. However, when the reservoir pressure becomes too high, the low-velocity tail of the Boltzmann distribution is depleted by collisions between fast and slow molecules. Apart from the conceptual interest in revisiting the low-velocity tail of the Boltzmann distribution, this study has practical benefits since it explains how the cold polar molecule source can be optimized for a specific application demanding, for instance, molecules with energies below a given trap depth. The parameter range, in which collisional effects play a role and how they can be observed in the experiment, is discussed in section 3.1. In section 3.2, the dependence of the signal of guided molecules on the reservoir pressure is discussed, which allows first conclusions about effects of collisions on the beam formation. A model is developed for collision-induced losses of slow molecules from the beam, which is discussed in section 3.3. In section 3.4 it is shown how the model can reproduce the dependence of the signal of guided molecules on the electrode voltage. Finally, the effect of collisions is confirmed by the observation of shifts in velocity distributions of the guided molecules presented in section 3.5.

3.1 Measurements of collisional effects

For the description of the velocity-filtering process in section 2.1, a purely effusive source was assumed. This means that the velocity distribution of the molecules injected into the guide is assumed to directly reflect the thermal velocity distribution of molecules in the nozzle. As soon as collisions between molecules come into play,

i.e., the mean free path Λ of the molecules becomes comparable to the dimensions d of the nozzle $\mathcal{O}(\Lambda) \approx \mathcal{O}(d)$, this condition is no longer fulfilled.

From an experimental point of view it is therefore instructive to perform measurements for varying inlet pressures. Thereby, effects caused by collisions of molecules in the nozzle or in the higher-density region directly behind the nozzle can be investigated. Furthermore, such an experiment is also interesting for more practical reasons. When using the guide as a source for cold polar molecules one wants to operate the system in a parameter regime which results in the maximum flux of guided molecules. This optimal value depends on the requirements of the specific application. When a high flux of molecules with velocities of a few 10 m/s is needed, collisions removing predominantly the slowest molecules are of no concern. Therefore, a higher reservoir pressure can be chosen, resulting in a higher flux of molecules in the guide. This changes if one is interested in only the slowest molecules. Here, the use of a smaller reservoir pressure to minimize collisional losses seems advisable.

To investigate these effects, the reservoir pressure is varied between 0.01 mbar and 2.0 mbar, as measured by the Pirani pressure gauge used for pressure regulation. These pressures span a wide range around the reservoir pressure of 0.1 mbar used for most other experiments so far [Mot07, Mot09a, Mot09b]. To make these numbers comparable to other guiding experiments with similar setups, the gas flow rate through the nozzle is calculated from the pumping speed and the observed pressure rise in the source chamber. For a reservoir pressure of 0.1 mbar a gas flow rate of 1×10^{-4} mbar·l/s with the nozzle assembly at room temperature is determined.

Due to this large variation in pressure, count rates of the quadrupole mass spectrometer (QMS) also vary over a large range. By measurements with different emission currents of the QMS ionization unit it was assured that the observed effects are indeed caused by differences in the molecular flux and not related to saturation of the ionization process or to nonlinearities in the detection process. All data used throughout the rest of chapter 3 were taken with 0.10 mA emission current, except for the velocity distributions measured at ± 3 kV and 0.01 mbar reservoir pressure. Here, the emission current was increased to 0.20 mA to increase the count rates and reduce the necessary measurement times. Comparing velocity distributions measured at higher reservoir pressures for different emission currents it was made sure that the higher emission current of 0.20 mA does not introduce systematic shifts.

3.2 Pressure dependence of velocity filtering

Figure 3.1 shows the signal of guided ammonia (ND_3) molecules as a function of reservoir pressure. In these plots, measurements for different electrode voltages and source temperatures are combined. The curves are fits to the data based on the model for the beam formation which will be presented in section 3.3. The model reproduces very well the shape of the pressure dependence for all electrode voltages.

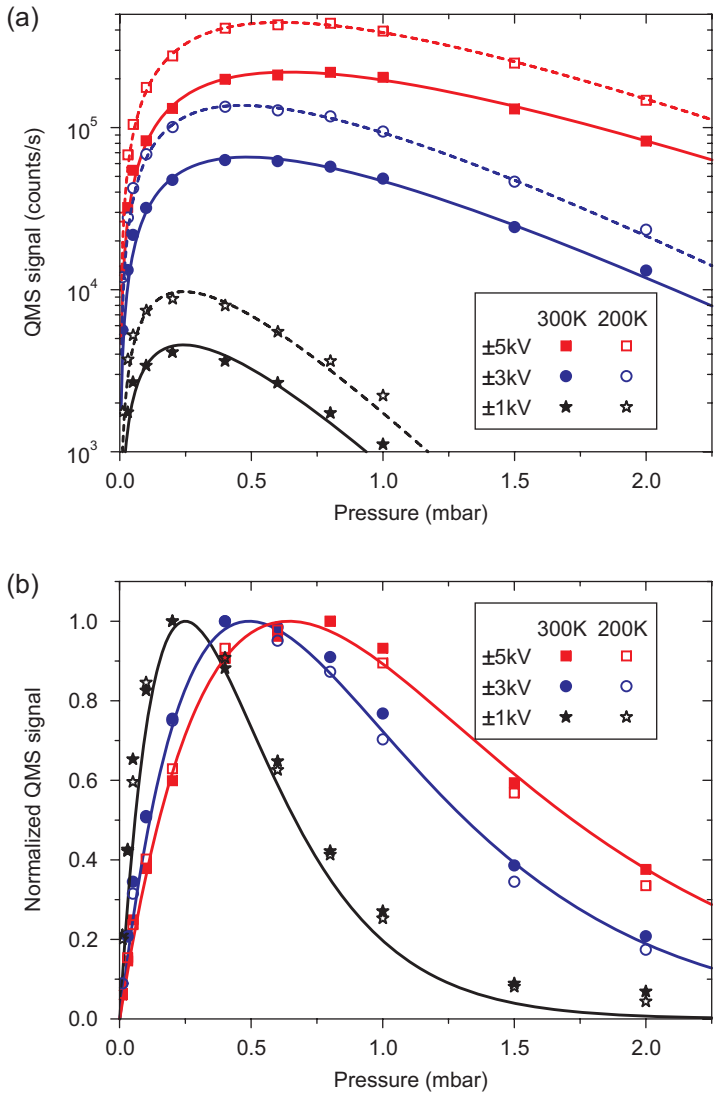

Figure 3.1: Signal of guided ammonia (ND_3) molecules as a function of reservoir pressure, measured for different combinations of electrode voltage and source temperature. The curves are individual fits to the data using the model for the beam formation including collisions in the high-pressure region, which is discussed in detail in section 3.3. The data of the ±1 kV measurements taken at a reservoir pressure ≥1 mbar are influenced by the rise of the background pressure in the detection chamber. In (a) absolute count rates are shown, while in (b) the same data are individually normalized for each electrode voltage and source temperature. This facilitates the visualization of the shift in the optimal pressure setting with the applied electrode voltage. Besides, it shows that the pressure dependence of the signal is independent of the source temperature.

Figure 3.1 (a) shows as well the good sensitivity of the detection by the QMS (guiding at only $\pm 1\,\mathrm{kV}$) with count rates of 10^3–10^5 counts/s.

The first feature to observe from Fig. 3.1 (a) is that, starting at zero pressure, the signal of guided molecules increases with reservoir pressure, reaches a maximum, and finally drops again. This behavior is expected considering the working principle of the guide described in section 2.1. The guide accepts molecules up to certain cutoff velocities, which depend on the molecules' mass and the Stark shift at the applied trapping field. For small pressures, an increase in pressure increases the number of molecules injected into the guide while the effusive character of the source is maintained. In contrast to this, for high pressures collisions in the nozzle and in the region behind the nozzle become important. Thereby, the slow molecules are eliminated from the beam. This leads to a decrease in the magnitude of the signal of guided molecules. The maximum is reached at a point where these two effects are balanced: Although more molecules are injected into the guide, the number of molecules with guidable velocities stays constant due to the reduced fraction of slow molecules. It should be noted that similar losses were observed by M. Gupta and D. Herschbach for beams of cold molecules as well. In their experiment, the cold molecules were produced in a supersonic expansion from a counterrotating nozzle, and the loss of slow molecules was described by an attenuation factor to account for collisions with a background gas [Gup99, Gup01].

A second feature to observe is the increase of the signal of guided molecules with applied electrode voltage [Ran03, Jun04a, Mot09b]. As shown in section 2.1, the cutoff velocities get larger when the electrode voltage is raised. For fixed reservoir pressure, this increases the fraction of molecules with guidable energies. The dependence of the signal of guided molecules on the applied electrode voltage will be discussed in more detail in section 3.4, since it allows to infer many details of the beam formation. Comparing measurements for fixed electrode voltage, it can be seen that cooling of the nozzle from 300 K to 200 K increases the signal of guided molecules by a factor of 2.2 [Jun04a].

Figure 3.1 (b) shows the normalized signal of guided molecules as a function of reservoir pressure. This figure allows to maximize the flux from the electric guide at a given electrode voltage. By choosing the optimal pressure setting, the number of guided molecules for a given electrode voltage, i.e., up to a certain cutoff velocity, is maximized. From this figure it can also be seen more clearly that the maximum of the curve shifts towards larger pressures when higher electrode voltages are used. This allows to infer the main feature of the model used to describe the beam formation. For higher electrode voltages, faster molecules can be guided. The increase of the optimal pressure with applied electrode voltage shows that for faster molecules collisions start playing a role only at higher pressures and thereby higher densities. This suggests that the collision probability scales with the time a molecule spends in the high pressure region or, equivalently, with $1/v$, where v is the molecule's velocity. In section 3.3, this assumption will be used as the basis of the model for the beam formation.

Comparing the measurements at 300 K and 200 K in Fig. 3.1 (b) it should be noted that not only the shape of the curves but also the optimal pressures for a given electrode voltage are identical. Measurements of the pressure in the vacuum chamber housing the nozzle, which have been performed at a constant reservoir pressure but for different temperatures of the cooling stage, indicate that the total line conductance is independent of the temperature of its last section (the nozzle). Hence, the gas flow through the nozzle for a given reservoir pressure does not depend on the temperature. The probability for a slow molecule to undergo a collision in the "high pressure region" is the same for the 300 K and 200 K measurement, since the same flux of molecules is streaming out of the nozzle. Therefore one observes the same dependence on reservoir pressure, independent of the nozzle temperature.

3.3 Model of velocity filtering including collisional losses

The effect of collisions is included into the theory of velocity filtering presented in section 2.1 as follows. The probability for a slow, in principle guidable molecule to undergo a collision with some fast molecule is proportional to the time t_c which the slow molecule spends in the region where collisions are most probable. In such a collision the velocity of a slow molecule is likely to increase. As a consequence, it cannot be guided anymore. Since no large variation of the gas density is expected over the transverse extent of the guide in each plane at a given distance from the nozzle, the transverse position and thereby the transverse velocity of the molecules has no influence on the collision probability. Hence, the probability for a slow molecule to be lost from the guided beam is inversely proportional to the molecule's longitudinal velocity v_z due to $t_c \propto 1/v_z$. To account for this velocity-dependent loss, an additional factor $\exp(-b/v_z)$ is included in the longitudinal velocity distribution. The model for velocity-dependent collisional losses results in a modified longitudinal velocity distribution $f_b(v_z)$

$$f_b(v_z)\,\mathrm{d}v_z = \frac{1}{N}\,\exp(-b/v_z)\,\exp(-v_z^2/\alpha^2)\,\mathrm{d}v_z, \tag{3.1}$$

where N is a constant such that the total flux coming out of the nozzle is normalized to $\int_0^\infty v_z\, f_b(v_z)\,\mathrm{d}v_z = 1$.

Figure 3.2 shows the effusive as well as the modified longitudinal velocity distributions of ammonia (ND_3) molecules emerging from the thermal source for different values of the parameter b. Because the collision probability depends linearly on the flux out of the nozzle, the parameter b is expected to depend linearly on the reservoir pressure. It can be seen that the fraction of slow molecules is more and more reduced for larger values of b. Figure 3.2 also shows that the rising slope of the velocity distribution of the molecules coming out of the nozzle shifts to larger velocities with b. Therefore, we shortly speak of a *boosting* of the beam and call b

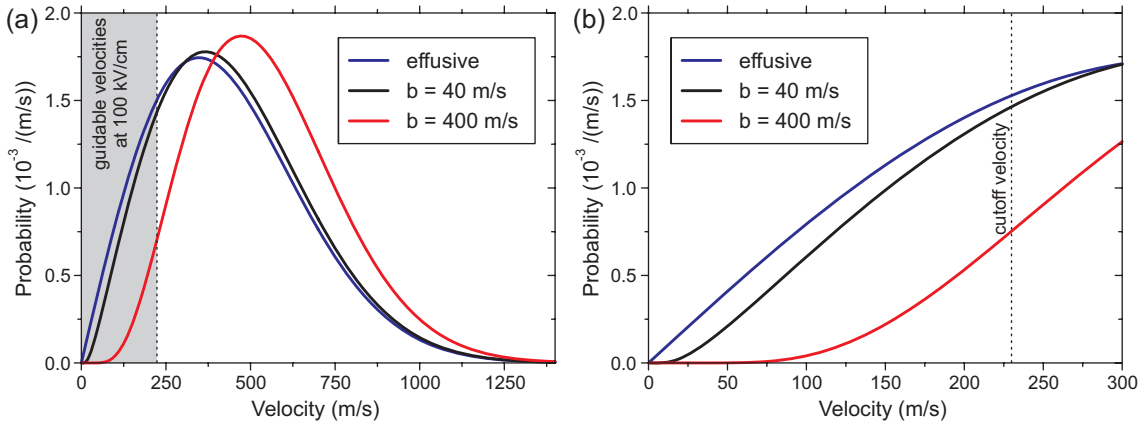

Figure 3.2: (a) Longitudinal velocity distributions including the boosting term $v_z\, f_b(v_z)$ of ammonia (ND_3) molecules emerging from the thermal source. Shown are distributions for different values of the boosting parameter b, corresponding to reservoir pressures of 0.1 mbar (b=40 m/s) and 1.0 mbar (b=400 m/s) in the experiment, in comparison to the velocity distribution of an ideal effusive source. Guidable velocities are indicated for a Stark shift of ΔW^s=2 cm^{-1} at an applied trapping electric field of 100 kV/cm, resulting in a longitudinal cutoff velocity of 230 m/s for ND_3. (b) is a zoom into the region of guidable velocities.

the *boosting parameter*. This effect is observable in experiments with small electrode voltages. At these settings only the slowest molecules which are most affected by the boosting are accepted by the guide, which strongly affects the measured signals. Boosting can also be observed for higher electrode voltages, when the reservoir pressure is increased. This results in larger boosting effects, which influence also faster molecules. At very high reservoir pressures, the resulting beam will have a narrow velocity distribution located at a high velocity. Such free-expansion beams [Pau00] have high intensity, but due to the lack of molecules with low velocity they are not compatible with the electrostatic velocity-filtering and guiding technique. Therefore, these experiments are performed in the near-effusive regime. There, the boosting is relatively small and a reasonable amount of slow molecules is present in the beam emerging from the source orifice.

The flux of guided molecules $\Phi(U)$ as a function of the electrode voltage U can be calculated by integration over the velocity distributions up to the longitudinal and transverse cutoff velocities as described in section 2.1. The factor $\exp(-v^2/\alpha^2)$ is neglected, since $v \ll \alpha$. This results in

$$\begin{aligned}\Phi(U) &= \int_{v_x=-v_{\max}}^{v_{\max}} \int_{v_y=-v_{\max}}^{v_{\max}} \int_{v_z=0}^{v_{\mathrm{l,max}}} f_{1D}(v_x) f_{1D}(v_y)\; v_z\; f_b(v_z)\; \mathrm{d}v_x \mathrm{d}v_y \mathrm{d}v_z \\ &\propto v_{\max}^2 \int_{v_z=0}^{v_{\mathrm{l,max}}} v_z\; \exp(-b/v_z)\; \mathrm{d}v_z \propto U \int_{v_z=0}^{v_{l,max}} v_z\; \exp(-b/v_z)\; \mathrm{d}v_z,\end{aligned} \tag{3.2}$$

where use has been made of $v_{\max}, v_{\mathrm{l,max}} \propto \sqrt{\Delta W^{\mathrm{s}}}$ and $\Delta W^{\mathrm{s}} \propto U$.

In the experiments, however, the QMS measures density, as discussed in section 2.4. Since the density n is connected to the flux by $n = \Phi/v$, the signal of guided molecules $S(U)$ is given by

$$S(U) \propto U \int_{v_z=0}^{v_{\mathrm{l,max}}} \exp(-b/v_z)\, \mathrm{d}v_z. \tag{3.3}$$

Without any boosting, i.e., assuming a perfectly effusive source ($b = 0$), this results in $S(U) \propto U^{3/2}$. For non-zero values of b the electrode voltage dependence of the signal of guided molecules is modified. This has been observed in previous experiments [Ran03, Jun04a, Rie06, Mot09b], where a dependence of the form $S(U) \propto U^2$ was extracted for molecules with linear Stark shifts and $S(U) \propto U^4$ for molecules with quadratic Stark shifts. This issue is addressed in more detail at the end of the following section.

3.4 Electrode-voltage dependence of velocity filtering

Figure 3.3 shows the signal of guided ammonia (ND_3) molecules as a function of the applied electrode voltage for different settings of the reservoir pressure. The data of the individual voltage scans is normalized to the fit value at ±6 kV electrode voltage. The solid curves are fits using Eq. (3.3) which takes into account the depletion of slow molecules from the guided beam due to collisions. The following boosting parameters are determined from these fits for the respective reservoir pressure: b=20 m/s (0.01 mbar), b=80 m/s (0.1 mbar), b=400 m/s (1.0 mbar). Several features can be observed from this figure and the fit results. Increasing the reservoir pressure results in more collisions and a larger boosting parameter. Therefore, a larger fraction of slow molecules is depleted, causing a relatively smaller signal at lower electrode voltages at which only the slowest molecules are guided. This causes the curve in the lin-lin plot, Fig. 3.3 (a), to bend stronger. From the log-log plot, Fig. 3.3 (b), the different character of the voltage dependencies can clearly be observed. For electrode voltages above ±(1–2) kV the fit curves for the 0.01 mbar and 0.1 mbar measurements are nearly straight lines in the log-log plot. However, the slope of the fit curve changes with reservoir pressure, indicating different power laws. The deviations for small electrode voltages may be explained by the behavior of the Stark shift: For small trapping electric fields the Stark energy of the ND_3 molecules becomes comparable to the inversion splitting, which leads to quadratic Stark shifts and therefore a smaller fraction of guided molecules.

The data shown in Fig. 3.3 are taken at 300 K source temperature. For a source temperature of 200 K exactly the same behavior is observed. The same effect, i.e., no influence of the source temperature, was already found in the pressure-dependence

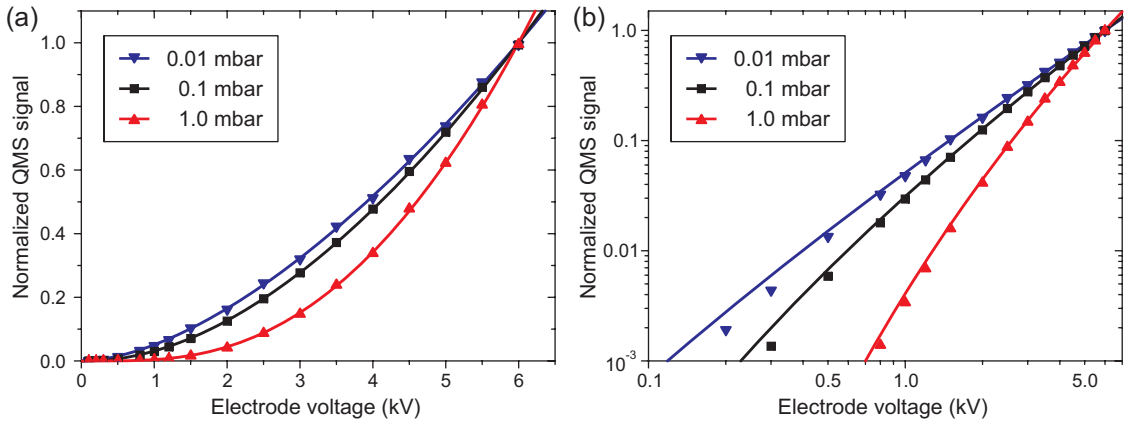

Figure 3.3: (a) Dependence of the signal of guided ammonia (ND_3) molecules on the electrode voltage for different reservoir pressures. The curves are individual fits using the model, Eq. (3.3), which accounts for collisions in the high-pressure region. The following boosting parameters are determined from these fits for the respective reservoir pressure: b=20 m/s (0.01 mbar), b=80 m/s (0.1 mbar), b=400 m/s (1.0 mbar). (b) shows the same data and fit curves with logarithmic axes to illustrate the good agreement between experimental data and the model over several orders of magnitude in reservoir pressure and signal.

study discussed in section 3.2. Since the flux of molecules out of the nozzle does not change with temperature in the present setup, the collision probability for a slow molecule shows the same dependence on the reservoir pressure, independent of the source temperature.

According to the developed model for the collisional losses, the boosting parameter b is expected to depend linearly on the flux of molecules out of the nozzle. As already discussed, the boosting parameter b increases with enlarged reservoir pressure (see Fig. 3.3). However, this increase is not linear. Especially at low electrode voltages the observed signal of guided molecules might be reduced by other effects than boosting, such as quadratic Stark shifts for small electric fields. This reduction of the molecule signal could result in too large fit values for the boosting parameter b.

To circumvent this problem, another approach is chosen to test the linear dependence of the boosting parameter on the reservoir pressure. For high reservoir pressures, resulting in a high flux of molecules out of the nozzle, relatively fast molecules are affected by the boosting as well. The boosting is therefore visible at higher electrode voltages, where a better signal-to-noise ratio of the signal of guided molecules is achieved. Furthermore, the absolute molecule loss due to collisional effects is larger, increasing the deviations from an ideal effusive source. Therefore, the measurement at the high reservoir pressure of 1.0 mbar is used as a reference. Then, the boosting parameter obtained from the fit to the data taken at 1.0 mbar is scaled linearly with reservoir pressure. Fig. 3.4 shows the electrode-voltage dependence of the signal of guided molecules together with curves of the model Eq. (3.3) using

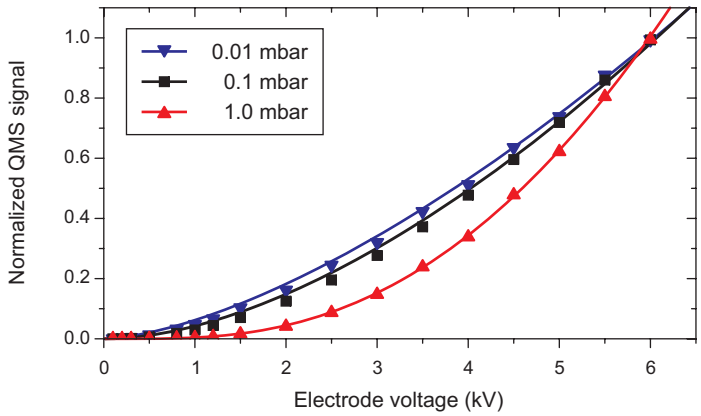

Figure 3.4: Dependence of the signal of guided ammonia (ND_3) molecules on the electrode voltage for different reservoir pressures. The same data are shown as in Fig. 3.3. To test the linear dependence of the boosting parameter on the reservoir pressure, the data at 1.0 mbar has been fitted with the model, Eq. (3.3), which takes into account collisions in the high-pressure region. This fit gives a boosting parameter b=400 m/s. For the other curves the boosting parameter determined at 1.0 mbar is scaled linearly with pressure, b=40 m/s (0.1 mbar) and b=4 m/s (0.01 mbar).

these scaled values of the boosting parameter b. The data are well described by the curves over the investigated range of reservoir pressures, which spans two orders of magnitude, thereby verifying the model of pressure-dependent collisional losses.

To connect the model for the signal of guided molecules $S(U)$, which includes collisions in the high-pressure region, to previous experiments, the data are fitted with $U^{3/2}$ and U^2 polynomials. Figure 3.5 (a) shows the dependence of the signal of guided molecules for very low reservoir pressure (0.01 mbar). For voltages above $\pm$(1–2) kV the data are well described by a $S(U) \propto U^{3/2}$ dependence represented by the solid line. This is exactly the electrode-voltage dependence expected for an ideal effusive source, as discussed in section 3.3.

Figure 3.5 (b) shows the signal of guided molecules at a medium pressure (0.1 mbar). For most experiments utilizing the guide, the source is operated in this range of pressures [Jun04a, Mot09b]. Here, the data are shown together with a fit of a $S(U) \propto U^2$ electrode-voltage dependence. In earlier experiments [Ran03, Jun04a, Rie06] the good agreement between the experimental data and the $S(U) \propto U^2$ model suggested a flux measurement in combination with an ideal effusive source. For calibrations of fluxes and densities of guided molecules, however, a QMS signal proportional to the density of molecules in the ionization volume was correctly assumed. The improved setup used for the experiments presented in this thesis allowed systematic measurements of the signal of guided molecules also for very small reservoir pressures. These studies confirm that the signal of the QMS is proportional to the density of the guided molecules in the ionization volume although it depends quadratically on the electrode voltage.

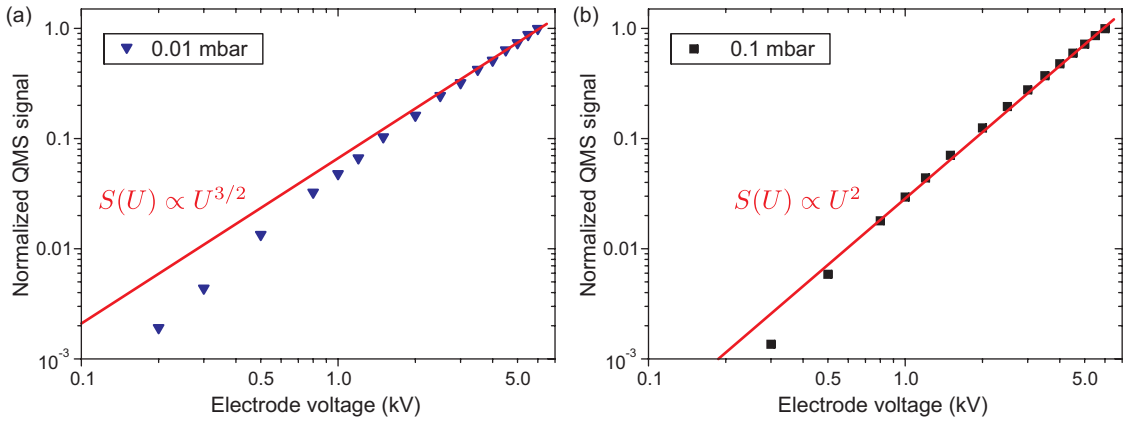

Figure 3.5: Dependence of the signal of guided ammonia (ND_3) molecules on the electrode voltage for different reservoir pressures. The same data are shown as in Fig. 3.3 and Fig. 3.4. The curves are fits using (a) $S(U) \propto U^{3/2}$ for the low pressure of 0.01 mbar and (b) $S(U) \propto U^2$ for the medium pressure of 0.1 mbar employed in most guiding experiments.

3.5 Velocity distributions of guided molecules

Additional information on the guided beam of polar molecules can be obtained from a velocity distribution, which is constructed from the time-resolved QMS signal as discussed in section 2.5. These velocity distributions represent another, even more direct, method to look at the boosting feature caused by collisions. This can be observed by comparing normalized velocity distributions determined for fixed electrode voltage but for different reservoir pressures in Fig. 3.6. For increasing reservoir pressures, the velocity distribution shifts to higher velocities. As expected, the cutoff velocity on the high-velocity side stays the same, because it depends only on the dominant Stark shift of the guided molecules and on the guide geometry. Molecules with a velocity exceeding this cutoff velocity cannot be guided. This also explains the shape of the pressure dependence curve discussed in section 3.2: For increasing reservoir pressure, larger and larger parts of the velocity distribution of molecules introduced into the guide are shifted beyond the cutoff velocity. Thereby, the fraction of molecules with velocities accepted by the guide decreases.

Comparing the velocity distributions for ±3 kV and ±5 kV electrode voltage in Fig. 3.6 (a) and Fig. 3.6 (b), one observes a shift in the cutoff velocity as well as in the position of the maximum of the distribution. The reason for this is the increase of the trapping field with electrode voltage. At larger trapping fields a larger velocity range of molecules is accepted by the guide as already discussed in section 2.1.

If one is interested only in the slowest molecules from the velocity distribution, increasing the pressure for an increase in guided signal is counterproductive. As discussed in section 3.2, the pressure for the optimal signal of guided molecules shifts to smaller values with reduced electrode voltage. This can be observed from the velocity distribution as well. For example, at a reservoir pressure of 1.0 mbar, the

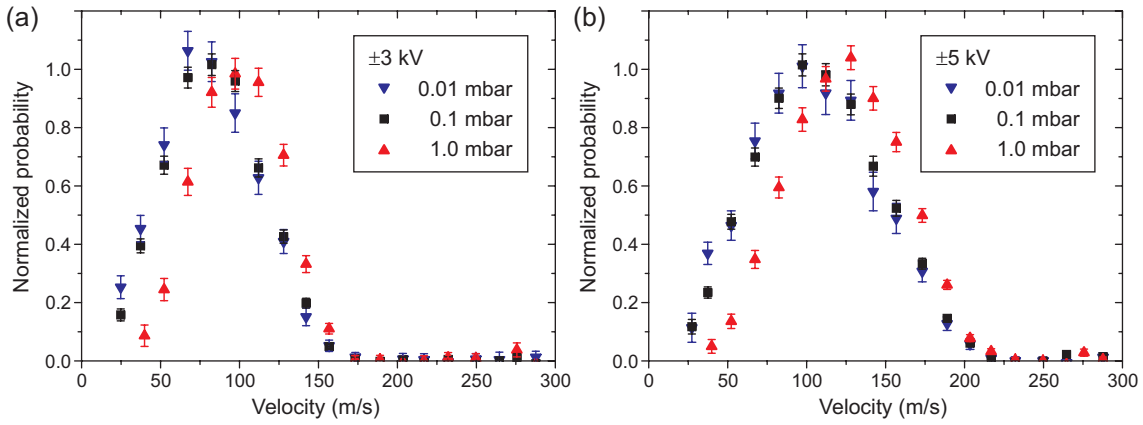

Figure 3.6: Normalized velocity distributions for different ammonia (ND_3) pressures in the reservoir. The effect of collisions is visible as a shift of the velocity distribution towards higher velocities for increasing reservoir pressure, while the cutoff velocity stays the same. Comparing the velocity distribution at (a) ±3 kV and (b) ±5 kV electrode voltage, the larger guiding electric field leads to an increase in the longitudinal cutoff velocity as well as to a shift towards higher velocities of the maximum of the distribution.

slowest molecules observed in the experiment have velocities of around 35–40 m/s, while at a reservoir pressure of 0.1 mbar molecules down to 25 m/s are observed. Especially in the ±3 kV measurement it can be seen that by decreasing the pressure from 0.1 mbar further to 0.01 mbar, the rising slope of the velocity distribution is slightly shifted to lower velocities. This is in agreement with the voltage dependencies shown in section 3.4, which also show an increase in the signal of guided molecules for low voltages, corresponding to slow molecules, when the pressure is reduced that way. Even for this very small reservoir pressure, extrapolation of the rising slope of the velocity distribution does not cut the velocity axis at zero velocity. Measurements of the electrode-voltage dependence for low (0.01 mbar) reservoir pressure show as well that for small electrode voltages less molecules are detected than expected from the $S(U) \propto U^{3/2}$ power law valid for a purely effusive source (see Fig. 3.5). This indicates that even for such reduced pressures collisions still play a role for the slowest molecules coming out of the nozzle. In the ±5 kV measurement this effect is less visible. This can be attributed to the very limited sensitivity of the time-of-flight (TOF) method on the low velocity side. For the lowest velocity in the distribution, the time-of-flight signal has already reached nearly 99 % of the steady state value. Therefore, the rising slope of the velocity distribution might be more susceptible to systematic errors even after rejecting the long-time data by the postselection.

For many applications the boosting should not be a problem. When the reservoir pressure is increased, the maximum of the velocity distribution does not shift too much: For an increase of the reservoir pressure from 0.1 mbar to 1.0 mbar the shift is only ≈ 25 m/s at ≈ 100 m/s peak velocity at ±5 kV. Nonetheless, this rise of the

reservoir pressure increases the flux of guided molecules and thereby the detector signal by a factor of five as shown in Fig. 3.1. This makes the source very attractive for, e.g., spectroscopic studies where a high density of cold molecules within a certain velocity interval is desirable.

3.6 Summary

In this chapter, the performance of the electric guide over a wide parameter range was described. This allows to verify a model for the beam formation taking into account collisions in and near the nozzle. In comparison to an ideal effusive source, these collisions reduce the fraction of slow molecules and thereby the efficiency for extraction of slow molecules from the reservoir. By operating in a dedicated pressure range, however, an optimized flux of molecules up to a given maximal velocity can be achieved. The effects of collisions in the formation of the beam are directly observed in the velocity distributions as well as in the characteristic shape of the electrode-voltage dependence of the signal of guided molecules. The results are in agreement with experiments employing a cryogenic helium buffer-gas cell for cooling of the molecules, where the source performance is limited only by the boosting for increasing helium densities [Som09, vB09]. Already with the room-temperature source, the beams produced by the electric velocity-filtering and guiding technique are well suited for collision experiments [Wil08a, Wil08b, Bel09a] or spectroscopic applications, since they combine a high continuous flux with a relatively high purity [Rie06, Mot07, Mot09b]. The detailed understanding of the electric guide as a source for cold polar molecules enables more insight for the design of future experiments, e.g., for loading of an electrostatic trap for molecules [Rie05]. There, further cooling of the molecules can be investigated. Proposed schemes include collision with simultaneously trapped ultracold atoms [Rie07a, Rie07b, Sch07b, Sch08] or combinations of suitably tailored trapping electric fields and infrared transitions [Zep09]. Also the development of a new source dedicated to experiments with only the slowest molecules benefits from these results. The electric guiding technique offers many prospects for future experiments by providing a starting point for new cooling schemes.

Chapter 4

Cold guided beams of water isotopologs

In this chapter, electrostatic velocity filtering and guiding is studied for the different water isotopologs H_2O, D_2O, and HDO. Although these molecules seem very similar at a first glance, when exposed to external electric fields they show a surprisingly different behavior due to their distinct Stark-shift properties. The reason for this is found in their different geometry with respect to the orientation of the electric dipole moment relative to the principal axes, as illustrated in Fig. 4.1.

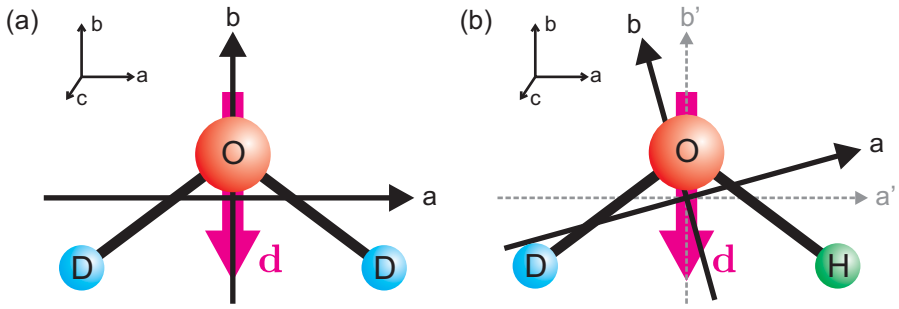

Figure 4.1: Orientation of the rotational axes in (a) D_2O and (b) HDO. The a- and b-axes lie in the plane spanned by the molecular bonds. In D_2O (and H_2O), the electric dipole moment $\mathbf{d}$ is oriented solely along the b-axis. Keeping the positions of the nuclei fixed, the principal axes (a, b) in HDO are rotated around the c-axis relative to the situation in D_2O (dashed axes, a', b'). As a result, a component of the dipole moment along the a-axis is present in HDO.

In chapter 2 it was shown how the efficiency of electrostatic velocity filtering and guiding depends on the ratio between the Stark shift and the mass of the molecules of interest. This parameter dependence of the velocity-filtering process can be studied in a distinguished way by experiments employing the different water isotopologs. Due to their similar chemical properties, no large influence of uncontrollable systematic effects on the measurement outcome is to be expected. These studies allow for

important conclusions on the influence of internal molecular states, and especially their Stark shift, on the efficiency of electrostatic velocity filtering and guiding. Furthermore, they illustrate the versatility of the electrostatic guide as a cold molecule source applicable to different species of polar molecules.

To describe the behavior of the different water isotopologs in external electric fields, the theory for the Stark shift of asymmetric-rotor molecules is presented in section 4.1. The results of numerical calculations of molecular Stark shifts for the water isotopologs are then discussed, and the characteristic differences are related to the specific rotational structure of the molecules. In section 4.2 it is shown how the calculated Stark shifts of H_2O, D_2O, and HDO, the filtering properties of the guide, and the thermal populations in the molecule source can be used to make predictions of the guided flux. The modifications made to the experimental setup to allow for systematic guiding experiments with the water isotopologs is briefly described in section 4.3. There, mainly the question is addressed how the contributions of the individual isotopologs to the guided beam can be obtained from the integrated mass spectrometer signal. After this discussion, the experimental results are compared to the theoretical predictions in section 4.4 and section 4.5. The differences in Stark shift between the isotopologs are directly evident from the characteristic dependence of the signal of guided molecules on the applied electrode voltage. Velocity distributions allow for an alternative point of view on these Stark-shift properties, and confirm the good agreement between the measurements and the theoretical predictions.

4.1 Stark shift of the water isotopologs

As shown in chapter 2, the flux of guided molecules in a certain rotational state is determined by the Stark shift of that state. The total flux is then given by the sum over the contributions of all the states which are thermally populated in the molecule source. To make a theoretical prediction for the fluxes of the different water isotopologs, their Stark shifts must be calculated. In section 4.1.1 it is shown how these Stark shifts are calculated by numerical diagonalization of the asymmetric-rotor Hamiltonian in the presence of an external electric field, following the procedure given by Hain *et al.* [Hai99]. For an introduction to the theoretical description of asymmetric-rotor molecules, the reader is referred to textbooks on molecular physics in general [Dem03b, Hak03] and on microwave spectroscopy in particular [All63, Bun05, Bun06, Gor70, Her45, Her50, Kro75, Tow75, Zar88]. Section 4.1.2 then illustrates how the symmetry properties and the orientation of the electric dipole moment of the different water isotopologs are displayed in the specific Stark shifts.

		H_2O	HDO	D_2O
Rotational	A	27.79	23.48	15.39
constants	B	14.50	9.13	7.26
(cm^{-1})	C	9.96	6.40	4.85
Dipole-moment	μ_A	0	0.66	0
components	μ_B	1.94	1.73	1.87
(Db)	μ_C	0	0	0

Table 4.1: Rotational constants and components of the electric dipole moment along the principal axes for the different water isotopologs H_2O, D_2O, and HDO [Tow75, Bri72], which have been used for the calculations.
During the composition of this thesis and after publication of M. Motsch *et al.*, Phys. Rev. A **79**, 013405 (2009), differing values for the dipole moment of H_2O were found in the literature: μ_B=1.94 Db [Gol48, Tow75], μ_B=1.86 Db [Bir52, Clo73, Dyk73, Lid90, Sho91]. These data suggest that the value μ_B=1.94 Db, which was extracted from A. L. Townes and C. H. Schawlow, Microwave Spectroscopy [Tow75], has been superseded by the value μ_B=1.86 Db. Since the Stark energy is determined by the product of the dipole moment and the electric field, this difference of 5 % in the value of the dipole moment only leads to a rescaling of the electric field at which a given Stark shift is reached. Due to the small magnitude, no significant influence on the results presented in this chapter is expected.

4.1.1 Calculation of Stark shifts

When a classical electric dipole $\mathbf{d}$ is subject to an external electric field $\mathbf{E}$, its energy ΔW^{s} depends on the relative orientation between the two vectors, $\Delta W^{\mathrm{s}} = -\mathbf{d} \cdot \mathbf{E}$ [Jac99, Dem99]. For parallel (antiparallel) orientation the dipole will minimize its energy for high (low) electric fields. Therefore, one refers to a dipole in the two situations as a high-field seeker (low-field seeker).

Considering a polar molecule, its dipole moment has a specific orientation relative to the body-fixed coordinate system. The molecule as a whole (and with it the body-fixed coordinate system) can rotate with respect to the space-fixed coordinate system, in which the external electric field is applied. This molecular rotation is described quantum-mechanically. Therefore, the orientation of the dipole moment in the space-fixed frame can be inferred from the molecular rotational state. The Stark shift of such a molecular rotational state is then calculated from the interaction between the molecular dipole moment and the external electric field. The molecular properties relevant for these calculations are listed in Tbl. 4.1. A, B, and C are the rotational constants along the principal axes of the molecule, where A (C) is oriented along the axis with largest (smallest) rotational constant, $A \geq B \geq C$. The orientation of the rotational axes in D_2O and HDO is illustrated in Fig. 4.1.

The Hamiltonian describing a rigid rotating molecule in the absence of external electric fields can be written as

$$H_{\mathrm{rot}} = \frac{1}{2}(A + C)\hat{J}^2 + \frac{1}{2}(A - C)H(\kappa), \tag{4.1a}$$

	Representation		
	I^r	II^r	III^r
x	b	c	a
y	c	a	b
z	a	b	c

Table 4.2: The three possible connections between the principal axes of the molecule (a, b, c) and the right-handed, body-fixed, coordinate system (x, y, z). X^r denotes the choice of right-handed coordinate systems, where X equals the representations I, II, or III. (Table adapted from [Kin43].)

	Representation		
	I^r	II^r	III^r
F	$\frac{1}{2}(\kappa - 1)$	0	$\frac{1}{2}(\kappa + 1)$
G	1	κ	-1
H	$-\frac{1}{2}(\kappa + 1)$	1	$\frac{1}{2}(\kappa - 1)$

Table 4.3: Coefficients used in the matrix elements of the reduced Hamiltonian, Eq. (4.2), for the different representations listed in Tbl. 4.2. (Table adapted from [Kin43].)

with the reduced Hamiltonian

$$H(\kappa) = \hat{J}_a^2 + \kappa \hat{J}_b^2 - \hat{J}_c^2. \tag{4.1b}$$

The constant $\kappa = (2B - A - C)/(A - C)$ is the so called asymmetry parameter, taking the value -1 in the limit of the prolate symmetric top ($A = B$) and $+1$ in the limit of the oblate symmetric top ($B = C$). $\hat{J}$ is the total-angular-momentum operator, and $\hat{J}_i$ $(i = a, b, c)$ are the projections of $\hat{J}$ on the figure axes, with $\hat{J}^2 = \hat{J}_a^2 + \hat{J}_b^2 + \hat{J}_c^2$. In the calculations, this Hamiltonian is evaluated in the symmetric-rotor basis. The non-zero matrix elements of the reduced Hamiltonian $H(\kappa)$, Eq. (4.1b), in the symmetric-top basis $\{|JKM\rangle\}$ are given by

$$\langle JKM|\, H(\kappa)\, |JKM\rangle = F\left[J(J+1) - K^2\right] + GK^2, \tag{4.2a}$$

$$\langle J, K \pm 2, M|\, H(\kappa)\, |JKM\rangle = H\left[f(J, K \pm 1)\right]^{1/2}, \tag{4.2b}$$

with

$$f(J, K \pm 1) = \frac{1}{4}\left[J(J+1) - K(K \pm 1)\right] \times \left[J(J+1) - (K \pm 1)(K \pm 2)\right]. \tag{4.2c}$$

The coefficients F, G, H are supplied in Tbl. 4.3. Only symmetric-rotor states with $\Delta K = 0, \pm 2$ are coupled by the asymmetric-rotor Hamiltonian as can be seen from

K_a	K_c	E	C_2^a	C_2^b	C_2^c	D_2
e	e	1	1	1	1	A
e	o	1	1	-1	-1	B_a
o	o	1	-1	1	-1	B_b
o	e	1	-1	-1	1	B_c

Table 4.4: Symmetry species of the asymmetric rotor. e and o refer to the parity (even or odd) of the quantum numbers K_a and K_c, respectively. E, C_2^a, C_2^b and C_2^c are the symmetry operations of the four group D_2, where E is the identity operation, and C_2^i performs a rotation by π around the i-axis. D_2 designates the symmetry species of the four group [Bun06].

Eq. (4.2). The eigenstates $A_{J\tau M}$ and energies $W_{J\tau M}$ of the asymmetric rotor can be found by diagonalization of the full asymmetric-rotor Hamiltonian, Eq. (4.1a), yielding

$$W_{J\tau M} = \frac{1}{2}(A+C)J(J+1) + \frac{1}{2}(A-C)W_{J\tau M}(\kappa) \tag{4.3}$$

and

$$A_{J\tau M} = \sum_K a_K^{J\tau M} \Psi_{JKM}. \tag{4.4}$$

In this expression, the eigenstates $A_{J\tau M}$ of the asymmetric rotor are expressed as linear superposition of symmetric-rotor wave functions Ψ_{JKM}. Note that the total-angular-momentum quantum number J and its projection on a space-fixed axis M are still good quantum numbers in the field-free asymmetric rotor, in contrast to K. This can already be seen from the asymmetric-rotor Hamiltonian which does not depend on M and which commutates with $\hat{J}^2$. The pseudo quantum number $\tau = K_a - K_c$ is used to label the asymmetric-rotor states in ascending order in energy. τ is directly related to the quantum numbers K_a and K_c in the limiting case of the prolate and oblate symmetric top. From these quantum numbers the symmetry properties of the asymmetric-rotor states can be derived. In Tbl. 4.4 the symmetry properties with respect to the symmetry operations of the four group D_2 [Bun06] (sometimes also referred to as $V(a,b,c)$ [Kin43]) are shown.

An external electric field lifts the degeneracy between the M sublevels of a state $|J,\tau\rangle$. Different J states are also coupled now, leaving M as the only good quantum number. In general, an asymmetric-top molecule can possess components of its dipole moment μ along all three principal axes in the body-fixed frame, $\boldsymbol{\mu} = \sum_g \mu_g \hat{e}_g$, $(g = a,b,c)$. As can be seen from Tbl. 4.1 and Fig. 4.1, the dipole moment is oriented along the b-axis in H_2O and D_2O, whereas components along the a- and b-axis are present in HDO. This is important for their Stark-shift properties, since different components promote couplings between rotational energy levels of different symmetry species. This aspect is discussed in more detail in section 4.1.2.

The electric field is defined to be directed along the Z-axis in the space-fixed frame ($F = X, Y, Z$), $\mathbf{E} = E_Z \hat{e}_Z$. Then, the interaction Hamiltonian is given by

$$H_{\mathrm{s}} = E_Z \sum_g \Phi_{Zg} \mu_g, \tag{4.5}$$

where the direction cosines Φ_{Fg} connect the space-fixed to the molecule-fixed frame. Since the direction cosines are tabulated for symmetric-rotor wave functions only (see Tbl. 4.5; note there are some misprints in the Φ_{Fg} tabulated in [Hai99] which are corrected here.), their matrix elements with respect to the asymmetric-rotor states have to be constructed. This can be done using the expansion of the asymmetric-rotor wave functions in terms of symmetric-rotor states, Eq. (4.4), and results in

$$\begin{aligned} &\langle J\tau M| \Phi_{Zg} |J'\tau' M'\rangle = \\ &\quad \langle J| \Phi_{Zg} |J'\rangle \langle JM| \Phi_{Zg} |J'M'\rangle \delta_{MM'} \times \sum_{KK'} a_K^{J\tau M} a_{K'}^{J'\tau' M'} \langle JK| \Phi_{Zg} |J'K'\rangle . \end{aligned} \tag{4.6}$$

Note that the Hamiltonian H_{s} describing the Stark interaction with the external electric field, Eq. (4.5), only couples states with $\Delta M = 0$, due to the choice of $\mathbf{E}$ along the Z-direction, $\mathbf{E} = E_Z \hat{e}_Z$. By diagonalization of the total Hamiltonian $H_{\mathrm{rot}} + H_{\mathrm{s}}(E_Z)$ the eigenstates and eigenenergies of the asymmetric rotor in the presence of an external field can be calculated. The Stark shift $\Delta W^{\mathrm{s}}(E_Z)$ is then given by the difference between the total energy in the external electric field and the zero-field energy.

	J'		
	$J+1$	J	$J-1$
$\langle J\,\vert\,\Phi_{Fg}\,\vert\,J'\rangle$	$\left[4\,(J+1)\,[(2J+1)\,(2J+3)]^{1/2}\right]^{-1}$	$[4J\,(J+1)]^{-1}$	$\left[4J\,(4J^2-1)^{1/2}\right]^{-1}$
$\langle JK\,\vert\,\Phi_{Fz}\,\vert\,J'K\rangle$	$2\left[(J+1)^2-K^2\right]^{1/2}$	$2K$	$-2\left[J^2-K^2\right]^{1/2}$
$\langle JK\,\vert\,\Phi_{Fy}\,\vert\,J',K\pm1\rangle$ $=\mp i\,\langle JK\,\vert\,\Phi_{Fx}\,\vert\,J',K\pm1\rangle$	$\mp\left[(J\pm K+1)\,(J\pm K+2)\right]^{1/2}$	$\left[(J\mp K)\,(J\pm K+1)\right]^{1/2}$	$\mp\left[(J\mp K)\,(J\mp K-1)\right]^{1/2}$
$\langle JM\,\vert\,\Phi_{Zg}\,\vert\,J'M\rangle$	$2\left[(J+1)^2-M^2\right]^{1/2}$	$2M$	$-2\left[J^2-M^2\right]^{1/2}$
$\langle JM\,\vert\,\Phi_{Yg}\,\vert\,J',M\pm1\rangle$ $=\pm i\,\langle JM\,\vert\,\Phi_{Xg}\,\vert\,J',M\pm1\rangle$	$\mp\left[(J\pm M+1)\,(J\pm M+2)\right]^{1/2}$	$\left[(J\mp M)\,(J\pm M+1)\right]^{1/2}$	$\mp\left[(J\mp M)\,(J\mp M-2)\right]^{1/2}$

Table 4.5: Direction cosine matrix elements $\langle J,K,M\,\vert\,\Phi_{Fg}\,\vert\,J'K'M'\rangle$ for the symmetric rotor. (Table adapted from [Cro44].)

4.1.2 Discussion of Stark shifts

The energies of the lowest-energetic rotational states of the different water isotopologs in an external electric field, calculated by the procedure described in section 4.1.1, are shown in Fig. 4.2 and Fig. 4.3. Several features are directly evident when comparing the different isotopologs. First of all, the calculations predict quadratic Stark shifts for H_2O and D_2O, while for HDO linear Stark shifts are found as well. This is caused by the different orientations of the electric dipole moments in the molecules with respect to the main axes of the molecule. In H_2O and D_2O the dipole moment is oriented along the b-axis. In HDO there is additionally a component along the a-axis. This is important, since in a more prolate asymmetric rotor, as is the case for the different water isotopologs (H_2O $\kappa = -0.49$, D_2O $\kappa = -0.54$, HDO $\kappa = -0.68$), the states with the same K_a quantum number within a manifold of states $\{|J, K_a, K_c\rangle\}$ with fixed J are near degenerate for increasing J and K_a quantum numbers. It is exactly these states which are coupled by a dipole moment along the a-axis in an external electric field. Hence, once the coupling between these states due to the electric field becomes larger than their asymmetric-rotor splitting, the Stark shift becomes linear. This behavior is illustrated in Fig. 4.3 for the lowest energy rotational states of HDO exhibiting a mainly linear Stark shift. For H_2O and D_2O the situation is completely different, here the Stark shifts stay quadratic and even become smaller with increasing rotational energy as can be seen from Fig. 4.4.

A second observation, which can be made from Fig. 4.2, Fig. 4.3, and Fig. 4.4, is that the magnitude of the Stark shifts of the isotopologs also differ. HDO exhibits the largest Stark shifts, as is to be expected because of their linear character. Besides, the Stark shifts of H_2O are significantly smaller than those of D_2O, although both molecules have similar size dipole moments and hence similar couplings between rotational states. The reason for this is also found in the rotational constants. Since D_2O has smaller rotational constants than H_2O, the energy levels are closer together, leading to larger Stark shifts for comparable couplings, as can be seen from perturbation theory.

The third observable feature is that the Stark shifts show a different behavior with increasing rotational energy for the different isotopologs. In HDO, the states $|J, \tau, M\rangle = |J, J, J\rangle$ exhibit the largest Stark shifts. As indicated in Fig. 4.4, the Stark shift approaches a constant value for these states. This value is reached for full alignment of the dipole-moment's component μ_a along the a-axis with the electric-field axis. The Stark shifts in H_2O and D_2O decrease with increasing rotational energy, as was already observed and described for D_2O by T. Rieger *et al.* [Rie06]. For these molecules the spacing between the rotational energy levels increases with increasing J and K quantum numbers, which reduces the Stark shifts.

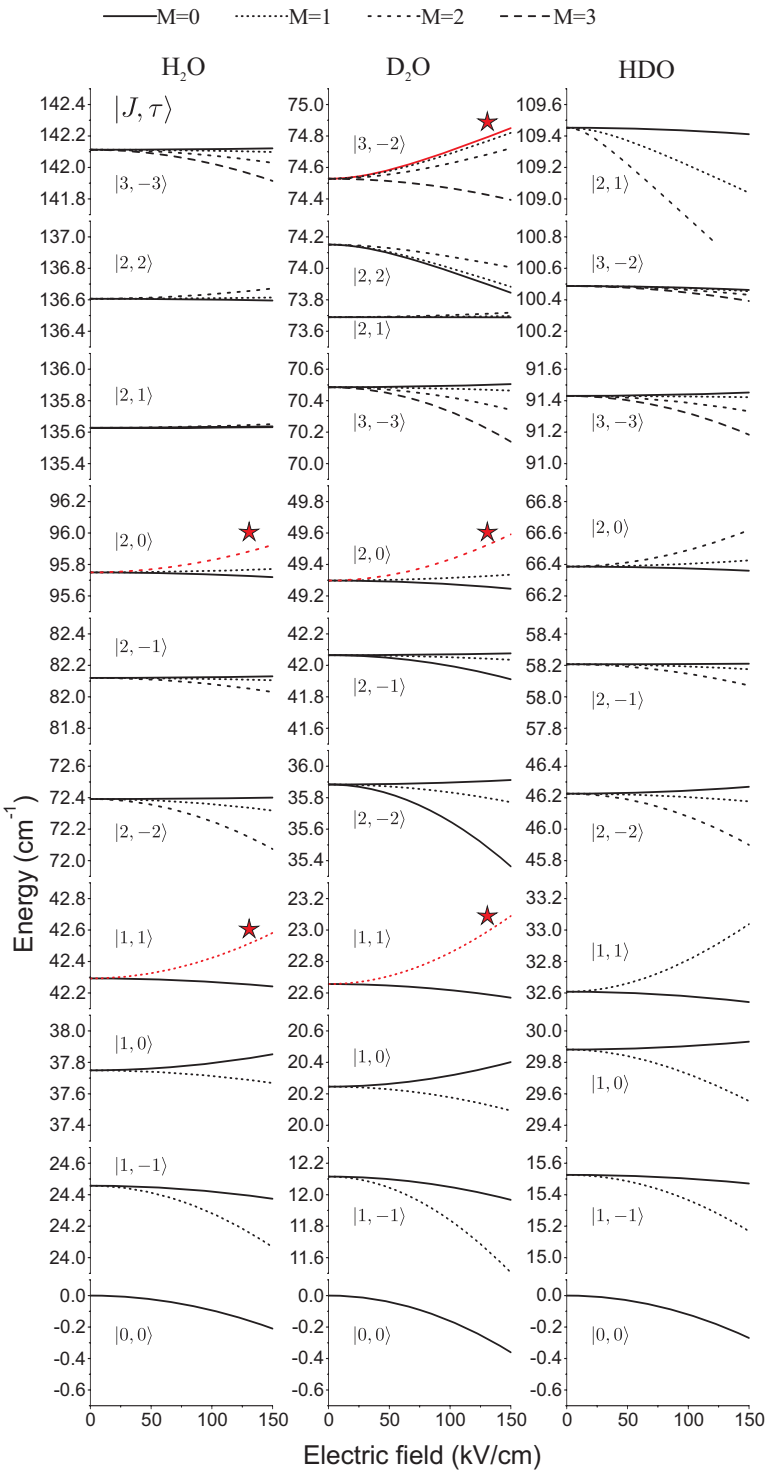

Figure 4.2: Lowest-energetic rotational states of the water isotopologs H_2O, D_2O, and HDO in an external electric field. The same vertical scale is used throughout the figure. States with contributions $> 5\,\%$ in the guided beam at a trapping electric field of 100 kV/cm (see Tbl. 4.8) are plotted in red and marked by a star.

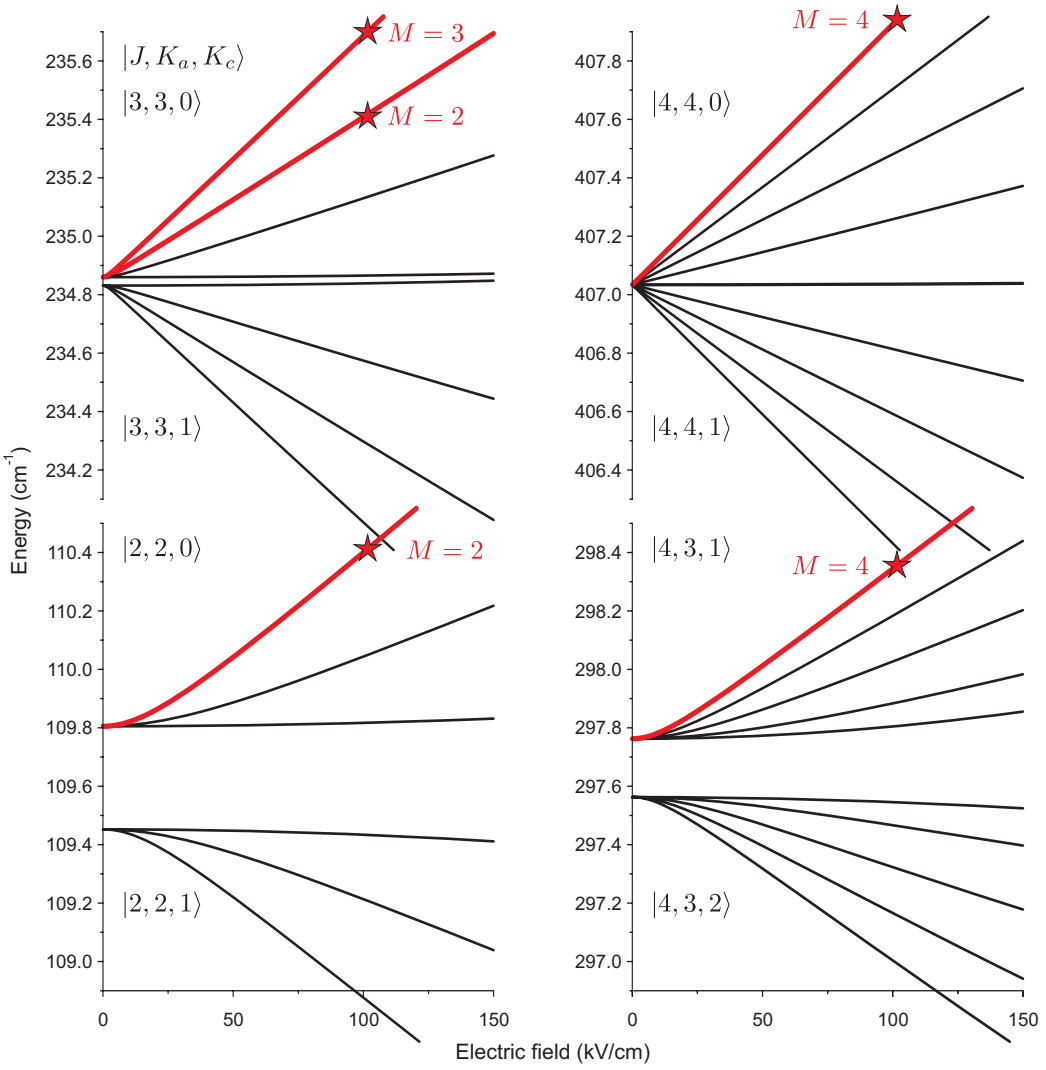

Figure 4.3: Lowest-energetic rotational states of HDO exhibiting mainly linear Stark shifts. The same vertical scale is used throughout the figure. States with contributions $> 5\,\%$ in the guided beam at a trapping electric field of 100 kV/cm (see Tbl. 4.8) are plotted with thick red lines and marked by a star. In this figure quantum numbers K_a and K_c are used to indicate the close connection to the prolate symmetric rotor. There, the asymmetric-rotor splitting between states with equal quantum numbers J and K_a disappears such that they are degenerate without external electric fields, giving rise to linear Stark shifts.

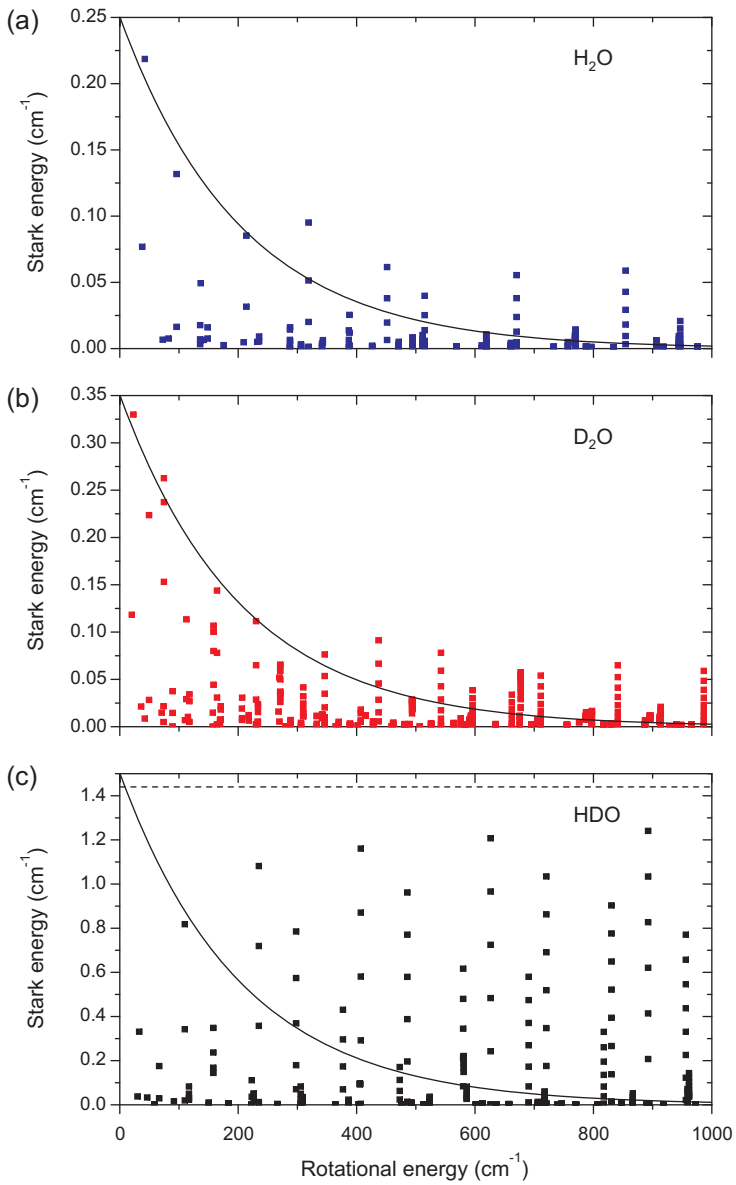

Figure 4.4: Stark shifts of the different water isotopologs H_2O, D_2O, and HDO at an electric field of 130 kV/cm. The solid curve indicates the Boltzmann factor $\exp(-E_{J\tau M}/k_BT)$ for a source temperature of 293 K. Only lfs states are shown. Note the different vertical scales. The different M states of a rotational state $|J, \tau, M\rangle$ all have the same rotational energy but different Stark shifts, thus forming a vertical sequence. Note that in the case of HDO the Stark shifts approach a saturation value for increasing rotational energy. This value, indicated by the dashed line, corresponds to the full alignment of the dipole-moment's component along the a-axis on the electric-field axis. In the case of the b-type rotors H_2O and D_2O the Stark shifts decrease with increasing rotational energy.

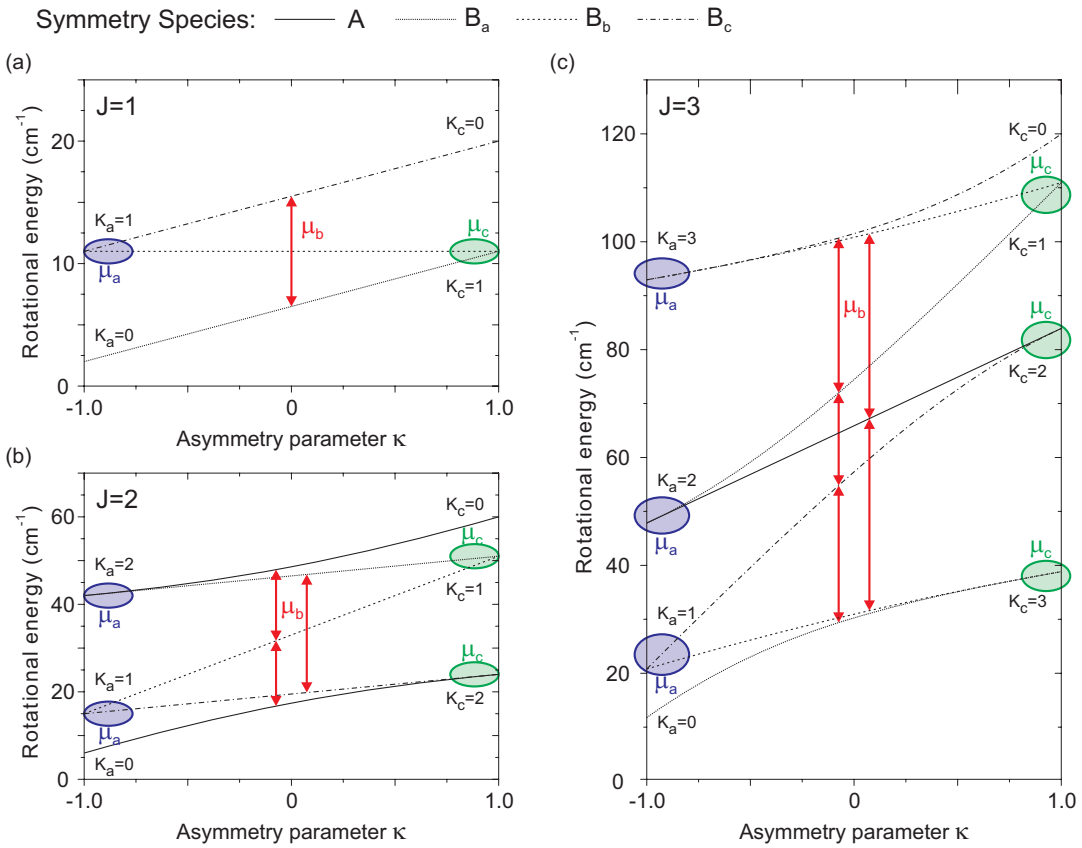

Figure 4.5: Couplings between the rotational energy levels of the asymmetric rotor, induced by the different components of an electric dipole moment. Shown are the energy levels of the asymmetric rotor for different J quantum numbers as a function of the asymmetry parameter κ. The symmetry of the rotational states, represented by the symmetry species of the four group D_2, is indicated by the dashing of the curves. A dipole moment μ_a along the a-axis mainly couples states which are degenerate in the prolate symmetric top, i.e., $\kappa = -1$, while a dipole moment μ_c along the c-axis mainly couples states degenerate in the oblate symmetric top, i.e., $\kappa = +1$. This near degeneracy gives rise to linear Stark shifts for these states. In contrast, states which are coupled by a dipole moment μ_b along the b-axis are always separated by an intermediate energy level, therefore never giving rise to a linear Stark shift. For this figure, rotational constants $A = 10\,\mathrm{cm}^{-1}$ and $C = 1\,\mathrm{cm}^{-1}$ were used, with $B = 1 \ldots 10\,\mathrm{cm}^{-1}$ varying linearly with κ.

More generally, the Stark-shift properties discussed above can be understood for an arbitrary asymmetric-top molecule by examining its rotational energy-level structure, the symmetry properties of its energy levels, and the couplings brought about by the different components of the molecular electric dipole moment. These couplings between rotational states of the different symmetry species are listed in Tbl. 4.6 for an external electric field along the Z-axis. Figure 4.5 shows the energy-level structure of an asymmetric-top molecule as a function of the asymmetry parameter κ for fixed values of total-angular-momentum quantum number J. The symmetry of the rotational energy levels, represented by the symmetry species A, B_a, B_b, B_c of the four group D_2, is indicated. The couplings induced by the different dipole-moment components μ_g according to Tbl. 4.6 are also shown in the figure.

As can be seen from Fig. 4.5, for a near-prolate asymmetric top, $\kappa \approx -1$, the energy levels with same K_a are near degenerate. These states are coupled by a dipole moment μ_a along the a-axis. This gives rise to linear Stark shifts, once the Stark interaction overcomes the splitting of these energy levels in the asymmetric rotor. Even in the most asymmetric case, $\kappa = 0$, the splitting between the states with highest rotational energy, $K_a = J$, $K_c = 0, 1$, decreases with increasing angular momentum, as can be seen by comparing the energy-level curves for increasing values of the J quantum number. This diminishing splitting gives rise to linear Stark shifts in the limit of large J for a dipole moment μ_a along the a-axis, even in this most asymmetric case.

Similar arguments hold for a near-oblate asymmetric top, $\kappa \approx +1$. Here, the energy levels with same K_c are near degenerate. These energy levels are coupled by a dipole moment μ_c along the c-axis, leading to linear Stark shifts as discussed for the near-prolate case. Once again, in the most asymmetric case, $\kappa = 0$, linear Stark shifts occur in the limit of large J, however for different rotational states. The states $K_a = 0, 1$, $K_c = J$, being coupled by a dipole moment μ_c along the c-axis, show a decreasing splitting with increasing J, which gives rise to linear Stark shifts.

The situation is, however, completely different for a dipole moment μ_b oriented along the b-axis. As can be seen from Fig. 4.5, the energy levels which are coupled by such a dipole moment are always separated by another energy level in between. Therefore, the splitting between states coupled by a dipole moment along the b-axis never approaches zero within one J system, independent of the value of the asymmetry parameter κ. More severely, the splitting between these energy levels coupled by a dipole moment μ_b along the b-axis even increases with increasing J. As can be seen from perturbation theory, this reduces the Stark shift for increasing rotational energy (large J). Of course, one could consider electric fields large enough to cause the Stark interaction to overcome this splitting of rotational states. Nonetheless, this generally does not lead to linear Stark shifts for low-field-seeking states. Coupling to other J states becomes relevant first, forcing all states to become high-field seeking.

Dipole-moment component	Coupled symmetry species	
μ_a	$A \leftrightarrow B_a$	$B_b \leftrightarrow B_c$
μ_b	$A \leftrightarrow B_b$	$B_a \leftrightarrow B_c$
μ_c	$A \leftrightarrow B_c$	$B_a \leftrightarrow B_b$

Table 4.6: Couplings between the different symmetry species of an asymmetric-rotor molecule by an external electric field applied along the space-fixed Z-axis. The molecular dipole moment may have components μ_g in the body-fixed frame, which promote the coupling to the external field. For a coupling between two asymmetric-rotor states $|i\rangle$ and $|f\rangle$ to occur, the matrix element $\mu_g E_Z \langle f| \Phi_{Zg} |i\rangle$ must not vanish. To give an example, if the dipole moment μ_a is oriented along the a-axis, the relevant component Φ_{Za} belongs to the symmetry species B_a. Assuming an initial state $|i\rangle$ with symmetry B_c, applying $\Phi_{Za} |i\rangle$ results in $B_a \circ B_c = B_b$. $\langle f| \Phi_{Zg} |i\rangle$ is nonzero only if its non-reducible representation contains E. Therefore, $|f\rangle$ must have symmetry B_b to fulfill this condition, since $B_b \circ B_b = E$. As a result, a state with symmetry B_c is coupled to a state with symmetry B_b for a dipole moment along the a-axis.

The Stark-shift properties examined in the preceding paragraphs can be understood from a purely classical point of view as well. For a classical rotating body, the rotation is stable around the axis of smallest and largest moment of inertia, i.e., the a- and c-axis. Around the axis of intermediate moment of inertia no stable rotation is possible. If the dipole moment is oriented along the a- or c-axis, there exists a non-zero expectation value of the projection of the dipole moment on the direction of the space-fixed electric field, except for a classical motion with the axis of rotation perpendicular to the external-field axis. The projection of the dipole moment directly interacts with the applied electric field, giving rise to a linear Stark shift. This situation is found in the the case of a symmetric top or for an a-type asymmetric rotor such as formaldehyde (H_2CO).

Conversely, if the dipole moment is oriented along the b-axis, i.e., the axis of intermediate moment of inertia, the expectation value of the projection of the dipole moment on the electric field axis is zero. Hence, the external electric field first has to hinder the rotation and orient the dipole, which becomes more and more difficult with increasing rotational energy and angular momentum. Therefore, the magnitude of the oriented dipole decreases with increasing rotational energy, in accordance with the description given by quantum mechanics. This oriented dipole moment can then interact with the electric field. This second-order interaction gives rise to a quadratic Stark shift for b-type rotors. The same argument holds for linear heteronuclear molecules with a permanent electric dipole moment, where the rotation averages out the projection of the dipole moment. Hence, linear molecules exhibit a quadratic Stark effect *unless* an electronic angular momentum parallel to the electric dipole moment $\boldsymbol{\mu}$ is present, such as, e.g., in Π states of NH, OH or CO^+.

However, note that in the case of accidental degeneracies also a b-type asymmetric rotor may show linear Stark shifts for certain states. For an example see,

K_aK_c	H_2O	D_2O	HDO
ee, *oo*	1	6	1
eo, *oe*	3	3	1

Table 4.7: Nuclear spin degeneracy factors g_I for the three water isotopologs H_2O, D_2O, and HDO [Tow75]. *e* and *o* refer to the parity (even or odd) of the quantum numbers K_a and K_c respectively.

e.g., the Stark-energy curves of the *b*-type asymmetric rotor CF_2H_2 in Fig. 2 in Hain *et al.* [Hai99]. There, the state $|J = 2, \tau = 2, M = 0\rangle$ is near degenerate with $|J = 1, \tau = 0, M = 0\rangle$, to which it is coupled by its dipole moment along the *b*-axis.. The mechanical analogue of these accidental degeneracies, if existing, is not evident. Overall one can summarize that even molecules such as the three water isotopologs H_2O, D_2O, and HDO, seeming very similar at a first glance, can show surprisingly different behavior when exposed to an external electric field.

4.2 Calculation of the flux of guided molecules

After having obtained the Stark shifts of the different water isotopologs, the fluxes of guided water molecules can be calculated. The total flux of guided molecules for a specific species is obtained by summing over the contributions of all the individual internal states to the flux, weighted with their thermal occupation in the source.

The thermal occupation of a rotational state $|J, \tau, M\rangle$ in the source is given by

$$p_{J\tau M} = \frac{1}{Z} g_M g_I \exp\left(-E_{J\tau M}/k_B T\right), \tag{4.7}$$

with the partition function $Z = \sum_{J\tau M} g_M g_I \exp\left(-E_{J\tau M}/k_B T\right)$. Here, $E_{J\tau M}$ is the rotational energy, T the source temperature, g_M the M degeneracy factor of the state, and g_I the nuclear spin degeneracy factor. Nuclear spin degeneracy factors for the different water isotopologs are listed in Tbl. 4.7.

The flux for a given guiding electric field can be expressed as

$$\Phi = N_0 \sum_{J\tau M} p_{J\tau M} f(\Delta W^{\mathrm{s}}_{J\tau M}), \tag{4.8}$$

with the guidable fraction of a rotational state $|J\tau M\rangle$ given by $f(\Delta W^{\mathrm{s}}_{J\tau M}) \propto (\Delta W^{\mathrm{s}}_{J\tau M})^2$ as shown in section 2.1, and N_0 the number of molecules injected into the guide per second. For molecules with only linear Stark shifts, $\Delta W^{\mathrm{s}}_{J\tau M}(E) \propto E$, the total flux of guided molecules is expected to show a quadratic dependence on the trapping electric field, $\Phi \propto E^2$, when an effusive source is assumed (see chapter 3). Similarly, for molecules with quadratic Stark shifts, $\Delta W^{\mathrm{s}}_{J\tau M}(E) \propto E^2$, a quartic dependence of the flux on the trapping electric field is expected, $\Phi \propto E^4$.

Figure 4.6 compares Stark shifts and calculated source populations of individual rotational states for H_2O and D_2O. From this figure it can already be anticipated

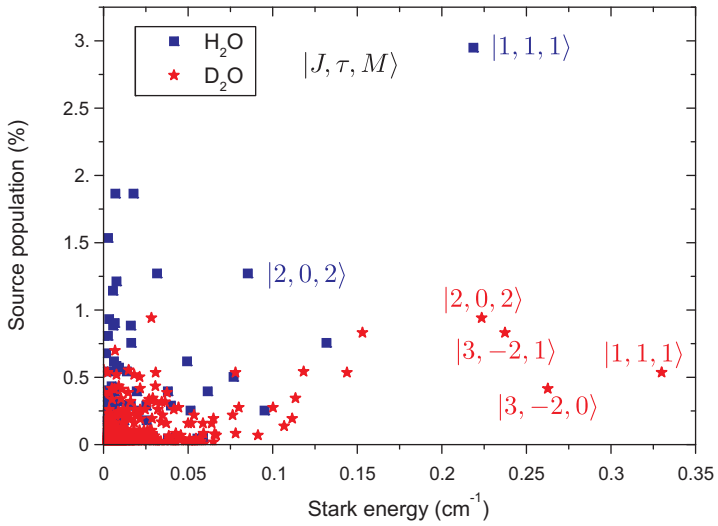

Figure 4.6: Calculated thermal populations in the source $p_{J\tau M}$ at a source temperature of 293 K, and Stark shifts $\Delta W^{\mathrm{s}}_{J\tau M}$ at an electric field of 130 kV/cm for the rotational states $|J, \tau, M\rangle$ of H_2O and D_2O. States with the largest contributions to the guided flux are labeled with quantum numbers.

that in the case of H_2O the state $|J = 1, \tau = 1, M = 1\rangle$ will contribute strongly to the guided flux. The reason for the large thermal population of this state in the reservoir, as compared to the $|J = 1, \tau = 1, M = 1\rangle$ state in D_2O, can be found in the different nuclear spin statistics of the two isotopologs. For such considerations based on symmetry properties it is advantageous to transform from $|J, \tau, M\rangle$ to the quantum numbers $|J, K_a, K_c, M\rangle$. For the state $|J = 1, \tau = 1, M = 1\rangle$ this results in the corresponding quantum numbers $|J = 1, K_a = 1, K_c = 0, M = 1\rangle$. According to Tbl. 4.7, this state is favored due to the nuclear spin statistics in H_2O by 3 : 1, while it is unfavored in D_2O by 3 : 6.

The expected guided fluxes of the different isotopologs calculated this way are depicted in Fig. 4.7 as a function of the guiding electric field. The guided fluxes of the different isotopologs differ remarkably in magnitude. Furthermore, not only its amount but also the electric-field dependence of the flux of guided molecules is clearly different. While H_2O and D_2O show a quartic dependence of the guided flux, caused by quadratic Stark shifts, the electric-field dependence of HDO shows a mainly quadratic behavior, indicating the presence of linear Stark shifts.

The calculations allow not only predictions of the magnitude and electrode-voltage dependence of the fluxes of guided molecules. Furthermore, it is possible to deduce the populations of individual rotational states in the guided beam. For the water isotopologs, populations of individual rotational states with contributions larger than 5% of the total flux of the considered isotopologs are listed in Tbl. 4.8. Remarkably, the single state $|J = 1, \tau = 1, M = 1\rangle$ of H_2O contributes $\approx 80\,\%$ to the guided flux using a room temperature source. Similarly, in D_2O the most populated state

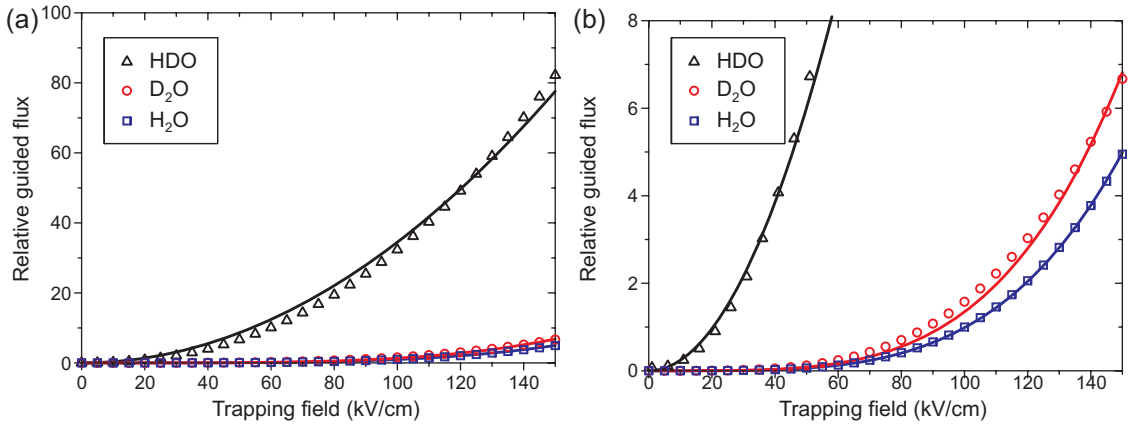

Figure 4.7: (a) Calculated guided fluxes of the different water isotopologs as a function of the trapping electric field. The results of the calculation described in section 4.2 are shown by the symbols, whereas the solid curves are quartic and quadratic fits to the calculated flux. Guided fluxes are normalized to the flux of H_2O at a trapping field of 100 kV/cm. The guided flux of HDO shows a quadratic dependence on the trapping electric field, whereas for H_2O and D_2O a quartic dependence is found. (b) is a zoom-in to compare the calculations of the guided flux for H_2O and D_2O to a quartic curve.

$|J = 1, \tau = 1, M = 1\rangle$ contributes $\approx 21\,\%$ to the total flux. The reason for these large populations as compared to a molecule such as formaldehyde (H_2CO) [Mot07] with similar size rotational constants but mainly linear Stark shifts can be found in the quadratic Stark shift behavior. As can be seen from Fig. 4.4, the size of the Stark shift decreases with rotational energy for a molecule with a quadratic Stark shift, leaving only few low-energetic states with largest Stark shifts for guiding [Rie06]. In chapter 5 it is shown how such calculated state populations are experimentally verified by collinear ultraviolet spectroscopy in a cold guided beam of formaldehyde [Mot07].

4.3 Experimental procedure

To verify the theoretically obtained relative fluxes of the different water isotopologs, experiments with H_2O, D_2O, and HDO were performed. The same experimental setup as the one described in section 2.2 was used. In this section, the key features of the setup and some experimental procedures for determination of the contributions of the individual isotopologs are highlighted. Water molecules in the gas phase are injected into the quadrupole guide through a ceramic tube with diameter 1.5 mm and a length of 9.5 mm. The pressure in the reservoir is kept at a fixed intermediate value of 0.10 mbar via a thermoelectrically controlled flow valve, resulting in a gas flow of 1×10^{-4} mbar·l/s. Since water has a sufficiently high vapor pressure of $\approx$ 25 mbar at room temperature [Lid90], no heating of its container is necessary. The constituents of the gas injected through the tube are monitored by a residual-

J	τ	M	E_{rot} (cm^{-1})	p_{S} (%)	ΔW^{s} (cm^{-1})	p_{G} (%)
1	1	1	42.3	2.9	0.13	79.3
2	0	2	95.7	0.8	0.08	7.4
3	1	3	213.6	1.3	0.05	5.1

(a) H_2O

J	τ	M	E_{rot} (cm^{-1})	p_{S} (%)	ΔW^{s} (cm^{-1})	p_{G} (%)
1	1	1	22.7	0.54	0.20	21.3
3	-2	1	74.5	0.83	0.16	21.2
2	0	2	49.3	0.94	0.13	17.1
3	-2	0	74.5	0.42	0.18	13.2
3	-2	2	74.5	0.83	0.10	8.0

(b) D_2O

J	τ	M	E_{rot} (cm^{-1})	p_{S} (%)	ΔW^{s} (cm^{-1})	p_{G} (%)
3	3	3	234.9	0.45	0.83	15.0
2	2	2	109.8	0.83	0.59	14.3
4	4	4	407.0	0.19	0.89	7.5
3	3	2	234.9	0.45	0.55	6.6
4	2	4	297.8	0.33	0.58	5.5

(c) HDO

Table 4.8: Properties of selected rotational states (population in the guide>5 %) of the three water isotopologs H_2O, D_2O, and HDO. E_{rot}: Zero-field rotational energy. p_{S}: Source population for a temperature of 293 K. ΔW^{s}: Stark shift at an electric field of 100 kV/cm. p_{G}: Population in the electric guide at an applied electric field of 100 kV/cm.

gas analyzer placed in the source vacuum chamber. This allows a determination of the contributions of the different isotopologs during each measurement, as is further explained in appendix A.

As shown in section 2.1, transversely slow molecules in a lfs state are trapped by the enclosing high electric fields. A longitudinal cutoff velocity is obtained by the bends in the guide. Slow molecules are guided around two bends and through two differential pumping stages to an ultrahigh-vacuum chamber, where they are detected by a quadrupole mass spectrometer (QMS). The molecules are ionized by electron impact in a cross-beam ion source and mass selected in the analyzer. In the final stage of the QMS single-ion counting is performed.

For guiding experiments with H_2O and D_2O, respectively, pure H_2O or D_2O are used. For measurements employing HDO, mixtures of liquid H_2O and D_2O with a ratio of 1:1 and 4:1 are prepared in the container. These result in a HDO fraction

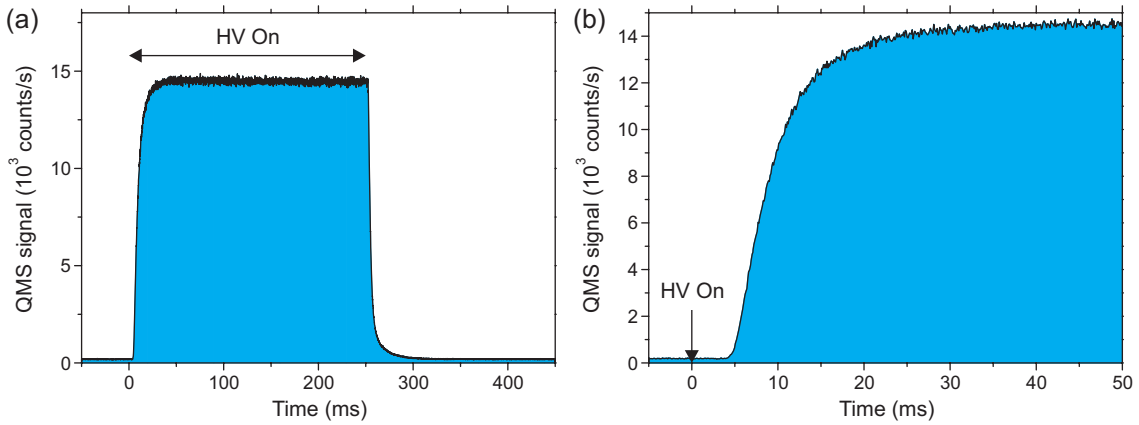

Figure 4.8: (a) Time-of-flight trace measured with HDO at an electrode voltage of ±5 kV. High voltage (HV) is switched on for an interval of 250 ms, with a 50 % duty cycle. (b) Zoom into the rising slope of the signal, from which a velocity distribution can be derived. These plots show raw data, i.e., no background subtraction has been applied. The excellent signal-to-noise ratio illustrates the wide applicability of electrostatic velocity filtering and guiding to different types of molecules. Note that for molecules with mainly linear Stark shifts such as, for instance, ND_3 or H_2CO, the QMS signal of guided molecules is even larger by one order of magnitude.

of ≈ 48 % and ≈ 27 %, respectively, coming from the source as measured with the residual-gas analyzer. When using these mixtures in the source, all three isotopologs are guided simultaneously. However, due to its much larger Stark shift for some rotational states (see section 4.1, and Fig. 4.4), HDO is preferentially guided.

To extract the relative molecule signals of the different isotopologs from these measurements, some corrections are necessary, which are explained in more detail in appendix A. First of all, the measured ion count rate of the individual isotopologs is corrected for their relative contribution to the gas injected into the guide as monitored by the residual-gas analyzer in the source chamber. Secondly, the fragmentation of the guided molecules during the electron-impact ionization in the QMS has to be taken into account.

The experiments are performed as a series of time-of-flight measurements. Here, the high voltage (HV) is switched on and off repeatedly in a fixed timing sequence. To subtract background contributions, the signal of guided molecules for the different isotopologs is determined from the difference in the steady-state QMS signal with HV applied to the guide and HV switched off, as explained in detail in section 2.3. A typical time-of-flight trace obtained with HDO is shown in Fig. 4.8. Although for molecules with mainly linear Stark shifts such as, for instance, ND_3 or H_2CO, the QMS signal of guided molecules is larger by one order of magnitude, an excellent signal-to-noise ratio is achieved.

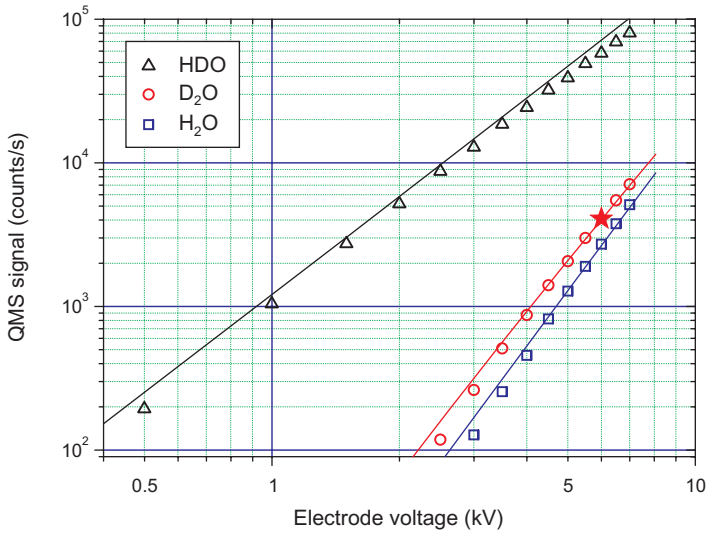

Figure 4.9: Signal of guided H_2O, D_2O, and HDO molecules as a function of applied electrode voltage. Shown as solid curves are the theoretically predicted signal dependencies, adjusted to fit D_2O data at $\pm 6\,\mathrm{kV}$ electrode voltage. This data point is marked by a star. Note that only one global scaling factor is used for all theory curves. The different slopes of the curves in the double logarithmic plot directly indicate the different Stark-shift properties. H_2O and D_2O show a quartic dependence of the signal of guided molecules on the applied electric field, indicating quadratic Stark shifts, whereas for HDO a mainly quadratic dependence indicating linear Stark shifts is found.

4.4 Electrode-voltage dependence

Figure 4.9 compares the measured electrode-voltage dependencies for the different water isotopologs to the outcome of the calculations discussed in section 4.2. The calculations are scaled by only one global scaling factor to account for detection efficiencies and the amount of gas injected through the nozzle into the guide. Note that *no relative scaling factor* between the calculations for H_2O, D_2O, and HDO has been employed. In this figure, the detector signal of the guided water molecules is compared to the calculated flux of guided molecules, albeit the QMS signal is proportional to the density of guided molecules arriving at the ionization volume as observed in section 2.4. However, due to the boosting of the beam, the electrode-voltage dependence changes as compared to an ideal effusive source. As explained in section 3.4, in the intermediate pressure regime, which was used for the measurements with the water isotopologs, a similar dependence of the detector signal on the electrode voltage is expected as for a flux measurement employing an ideal effusive source. In particular, $S(U) \propto U^2$ ($S(U) \propto U^4$) is expected for molecules with linear (quadratic) Stark shifts. Due to the smaller signals, no experiments at a reduced reservoir pressure of 0.01 mbar were performed, where no strong effect of the boosting on the electrode-voltage dependence would be expected.

As shown in Fig. 4.9, the electrode-voltage dependence of the molecule signals is well described by the calculations over more than two orders of magnitude. This excellent agreement between experiment and theory verifies that the filtering process is well described by the model of electrostatic velocity filtering presented in section 2.1, using the Stark shifts of the water isotopologs calculated in section 4.1 and deducing the total guided flux from the contributions of the different internal states as discussed in section 4.2.

HDO shows the largest molecule signal of all three water isotopologs, as predicted from calculations. Experimentally a ratio of detector signals between HDO and D_2O of 16.4 (18.9) is determined at a guiding field of 130 (100) kV/cm, where the calculations predict 14.7 (20.5). This is well within the overall uncertainty given e.g. by the determination of the relative contributions of isotopologs injected through the nozzle as derived from the residual-gas-analyzer signal. The measurements done with different HDO amounts give count rates agreeing to within 5–10 %, which allows an estimate for the uncertainty of the residual-gas-analyzer corrections applied. Furthermore, the guided flux of HDO largely stems from rotational states at higher rotational energies. These are therefore more strongly affected by centrifugal distortion corrections not included in the rigid rotor approximation being used, leading to energy level shifts and hence changes of Stark shifts which can affect the accuracy of the calculations.

The measured signals of guided H_2O and D_2O show a quartic dependence on the applied electrode voltage, as was shown for D_2O already in a previous experiment [Rie06]. The electrode-voltage dependence for the molecule signal of HDO is best described by a quadratic behavior, confirming the main contributions from states with linear Stark shifts predicted by calculations. This different dependence of the guided signal on the applied electric field is directly evident from different slopes in the double logarithmic plot shown in Fig. 4.9.

The detector signals of the water isotopologs can be roughly compared to other molecules used so far. For deuterated ammonia ND_3, count rates on the order of 3×10^5 counts/s were observed in the same setup at an electrode voltage of ± 5 kV, using a reservoir pressure of 0.1 mbar with the nozzle assembly at room temperature. With the QMS used in the experiment, ND_3 is detected at mass 20 amu with a fragmentation probability of 53 %. Therefore, one arrives at a total signal of guided ND_3 molecules of 6×10^5 counts/s. When a 1:1 mixture of H_2O and D_2O is prepared and a reservoir pressure of 0.1 mbar is maintained, a signal of 1.5×10^4 counts/s for guided HDO molecules is observed at mass 19 amu. Here, a fragmentation probability of 74 % for detection at mass 19 amu must be taken into account, as well as the purity of ≈ 48 % for HDO injected through the nozzle into the guide. Putting all together, this results in a total signal of 4×10^4 counts/s for HDO, assuming the same number of molecules were injected into the guide. The reason for this smaller flux can be found in the fact that for HDO only few states exhibit linear Stark shifts and hence contribute to the guided flux, whereas ND_3 exhibits mainly linear Stark shifts. Furthermore the Stark shifts of HDO are smaller due to the

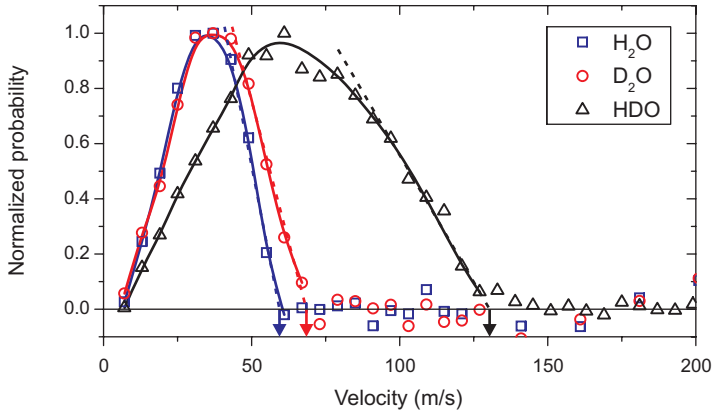

Figure 4.10: Normalized velocity distributions for the water isotopologs H_2O, D_2O, and HDO at an electrode voltage of $\pm 5\,\mathrm{kV}$. The velocity distributions are derived from the rising slope of time-of-flight measurements such as the one shown in Fig. 4.8. The solid curves are a guide to the eye. Vertical arrows indicate the cutoff velocities obtained by linear extrapolation (dashed lines) of the high-velocity side.

smaller dipole-moment component along the a-axis (0.66 Db [Bri72]) as compared to the dipole moment of ND_3 (1.5 Db [Hal67, DL81, Gan87]). Nevertheless, the fact that molecules with so different Stark-shift properties can be efficiently filtered out of a thermal gas illustrates the wide applicability of the velocity-filtering technique. For chemically stable polar molecules which can be supplied to the nozzle via the Teflon tube, it is sufficient to bring them into the gas phase in a reservoir at a pressure in the 0.1–1 mbar range. At smaller pressures guiding is still possible, however at the expense of reduced signals. Chemically very reactive molecules such as molecular radicals (typical examples are OH and NH) are in principle also guidable. Beams of molecular radicals can be loaded into a buffer-gas cell, where they thermalize by collisions with the cryogenic helium gas [Cam07]. The translationally and internally cooled down molecules can then be extracted by an electrostatic quadrupole or magnetic guide [Pat07, Som09, vB09] and made available for further experiments.

4.5 Velocity distributions

The different Stark-shift properties of the various water isotopologs are also illustrated by their velocity distributions. The cutoff velocity, i.e., the velocity of the fastest molecules which can still be guided around the bends of the quadrupole, is given by the ratio between the molecules' mass and its Stark shift. Hence, it depends on the rotational state of the molecule. Since for molecules from a thermal source many states contribute to the guided flux, the cutoff velocity is given by the state with the largest Stark shift. In the experiment, the cutoff velocity is determined from a linear extrapolation of the high-velocity side of the velocity distribution to-

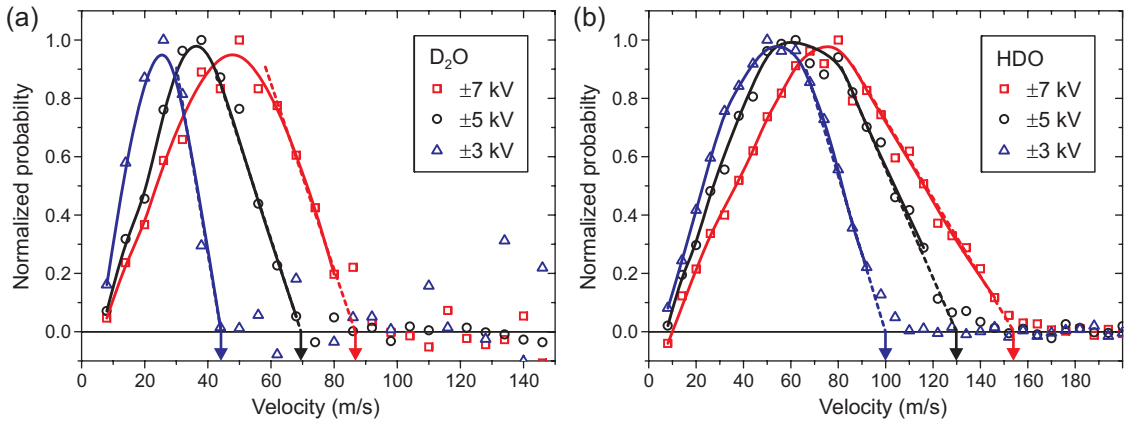

Figure 4.11: Normalized velocity distributions for D_2O and HDO as a function of electrode voltage (±3 kV, ±5 kV, ±7 kV). The solid curves are a guide to the eye. The vertical arrows indicate the cutoff velocity, which is determined from a linear approximation (dashed lines) to the high-velocity side.

wards zero. From the measurements performed at an electrode voltage of ±5 kV it can be seen in Fig. 4.10 that the maximum of the distribution as well as the cutoff velocity shifts towards higher velocities from H_2O to D_2O and HDO. This is caused by the much larger Stark shifts of HDO as compared to H_2O and D_2O (see Fig. 4.4). The wide velocity distribution for HDO is caused by the large Stark shifts found for this isotopolog and by the used bend radius of 5 cm. Experimentally, cutoff velocities of 60 m/s for H_2O, 69 m/s for D_2O, and 130 m/s for HDO are determined at an electrode voltage of ±5 kV. Calculated Stark shifts of states contributing to the guided flux (similar to Tbl. 4.8, but for a guiding field of 93 kV/cm reached at ±5 kV electrode voltage) result in cutoff velocities of 57 m/s for H_2O, 67 m/s for D_2O and 125 m/s for HDO. These are in good agreement with the measurements. For HDO states with large Stark shifts of up to 0.80 cm^{-1} at ±5 kV electrode voltage are predicted to contribute ≈ 20% to the guided flux. These states might be responsible for the small but non-zero signal in the HDO velocity distribution between 130 m/s and 150 m/s, being supported by the fact that a cutoff velocity of 150 m/s corresponds to a Stark shift of 0.80 cm^{-1}. Note that this signal exceeding the linear extrapolation to the falling slope of the velocity distribution is present in all three velocity distributions of HDO shown in Fig. 4.11 (b). On the low-velocity side of the velocity distribution a linear extrapolation does not cut the horizontal axis at zero velocity. This can be attributed to collisions of the molecules in the vicinity of the effusive source, which removes the slowest molecules from the thermal distribution. This effectively leads to a boosting of the molecules entering the guide and hence to a shift of the velocity distribution, as explained in chapter 3.

Measurements of velocity distributions for different electrode voltages (±3 kV, ±5 kV, ±7 kV) were performed for D_2O and HDO, and are shown in Fig. 4.11. In the data, a shift of the maximum of the distribution and of the cutoff velocity, i.e.,

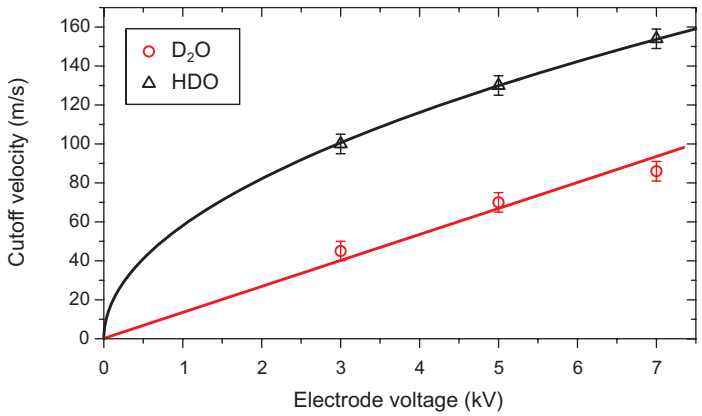

Figure 4.12: Voltage dependence of the longitudinal cutoff velocity for D_2O and HDO. For D_2O the solid line represents a linear fit, while for HDO the solid curve is a fit of a square-root dependence. These dependencies are expected for quadratic (D_2O) and linear (HDO) Stark shifts respectively.

the maximal velocity of molecules which can still be guided, can be seen. This is to be expected, since larger voltages applied to the guide electrodes result in a deeper trapping potential. Hence, faster molecules are guided. The dependence of the cutoff velocities on the applied electrode voltage is shown in Fig. 4.12. A linear dependence in the case of D_2O and a square-root dependence in the case of HDO is observed. As was shown in section 2.1, the cutoff velocity depends on the square-root of the Stark shift at the applied guiding field. Hence, a linear dependence such as the one observed for D_2O is found for molecules with only quadratic Stark shifts, whereas a square-root dependence is found for molecules such as HDO where states with linear Stark shifts dominate the flux of guided molecules.

4.6 Summary

Cold guided beams of the water isotopologs H_2O, D_2O, and HDO are produced in an efficient way by electrostatic velocity filtering. The signals of the different isotopologs show quartic and quadratic electrode-voltage dependencies, respectively, caused by quadratic Stark shifts for H_2O and D_2O, and by linear Stark shifts of the states contributing most to the guided flux in HDO. These different Stark-shift properties are also evident from the dependence of the cutoff velocity on the applied guiding electric field as measured for D_2O and HDO.

For a theoretical description, the influence of molecular parameters on the behavior of the molecules in an external electric field is investigated. More specifically, the magnitude of the rotational constants and the orientation of the electric dipole moment with respect to the rotational axes determines the molecules' Stark shift. Based on this discussion of molecular Stark shifts, predictions for the efficiencies of

electrostatic velocity filtering for the different isotopologs are made. Excellent agreement between the experimentally observed signals and the calculations of fluxes of guided molecules is found, confirming that the velocity-filtering process is well described by the presented model. Furthermore, these calculations allow to deduce populations of individual rotational states in the guided beam, which can be as high as 80 % in the case of H_2O for a room-temperature source. In the next chapter, a direct method for internal-state diagnostics, depletion spectroscopy, is described and applied to cold guided beams of formaldehyde molecules [Mot07].

Chapter 5

Internal-state thermometry by depletion spectroscopy in a cold guided beam of formaldehyde

In this chapter, an experimental tool for measurements of the internal-state distribution in guided beams of polar molecules is presented. In the experiments with the different water isotopologs discussed in chapter 4, this internal-state distribution could be inferred only indirectly from the specific electrode-voltage dependence of the signal of guided molecules as well as from their velocity distributions. These data yielded information about the Stark-shift character of the internal states dominating the flux of guided molecules.

Complementing electrostatic guiding by depletion spectroscopy, the internal-state distribution of electrostatically guided formaldehyde (H_2CO) molecules is directly accessible. Formaldehyde exhibits a rich-structured electronic spectrum in the near-ultraviolet (280–360 nm) region [Can90, Mot08], permitting direct excitation with narrow-bandwidth cw-lasers. The molecules are excited in the $2_0^1 4_0^3$ rovibrational band of the $\tilde{A}^1A_2 \leftarrow \tilde{X}^1A_1$ transition around 330 nm [Clo83]. Since the $\tilde{A}^1A_2$ excited state of formaldehyde predissociates [Moo83], molecules pumped to this state are lost from the guided beam. Hence, the depletion induced by the laser beam is a direct measure for the population of a state, even when only the integrated signal is accessible to the detector. By addressing individual rotational states, the internal-state distribution of the guided formaldehyde molecules is inferred and can be compared to theoretical predictions.

In section 5.1, the experimental setup used for these experiments is presented. Here, mainly the continuous-wave laser system in the near-ultraviolet spectral region is described. As a prerequisite for depletion spectroscopy, the transition frequencies from the states of interest in the guided beam are needed. Therefore, room-temperature absorption spectroscopy of formaldehyde in the wavelength range 30140–30790 cm^{-1}, covering two rovibrational bands ($2_0^1 4_0^3$ and $2_0^2 4_0^1$), has been performed [Mot08]. The rotational constants derived from a fit to this data using genetic

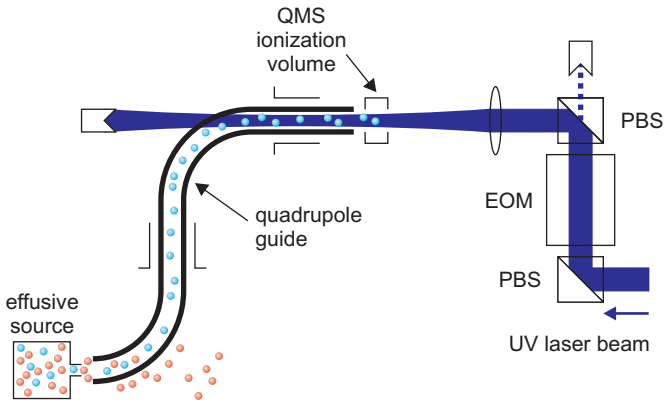

Figure 5.1: Experimental setup. Formaldehyde molecules from an effusive source are injected into the electrostatic quadrupole guide and led to the QMS cross-beam ionization volume. The ultraviolet (UV) laser beam is overlapped with the molecular beam in the last 15 cm long straight section of the guide. The light is switched on and off by an electro-optical modulator (EOM) placed between two polarizing beamsplitter cubes (PBS).

algorithms [Mee04, Mee06a, Mee06b] is then used for calculations of the spectrum, allowing line identification and prediction of line positions for guided states. In section 5.2 this room-temperature spectroscopy experiment is discussed. The actual experiment to determine state populations by depletion spectroscopy in the cold guided formaldehyde beam is discussed in section 5.3. There, the measurements are also compared to the expected contributions of individual internal states calculated by the procedure described for the water isotopologs in chapter 4. To show that cooling of the reservoir indeed increases the purity of the guided beam depletion spectroscopy was performed for source temperatures ranging from 150–300 K.

5.1 Experimental setup

The experimental setup is shown in Fig. 5.1. Gaseous formaldehyde (H_2CO) is produced by heating paraformaldehyde powder (Sigma-Aldrich) to a temperature of 80–90 °C. To clean the dissociation products and remove unwanted water and polymer rests, the gas is led through a dry-ice cold trap at a temperature of ≈-80°C [Spe35]. The formaldehyde gas is then injected into the quadrupole guide through the ceramic nozzle described in section 2.2. The temperature of the liquid-nitrogen cooled nozzle can be varied in the range 100–300 K by a heater. Similar to ammonia, temperatures between 150–300 K can be used to maintain a reasonable pressure of formaldehyde at the nozzle. For lower temperatures the vapor pressure is too small, such that no useful molecule flux out of the nozzle into the guide is achieved anymore.

The slow molecules are guided around two 50 mm radius bends and through two differential pumping stages to the cross-beam ionization unit of a quadrupole mass spectrometer (QMS) in the same setup as discussed in section 2.2. In the straight

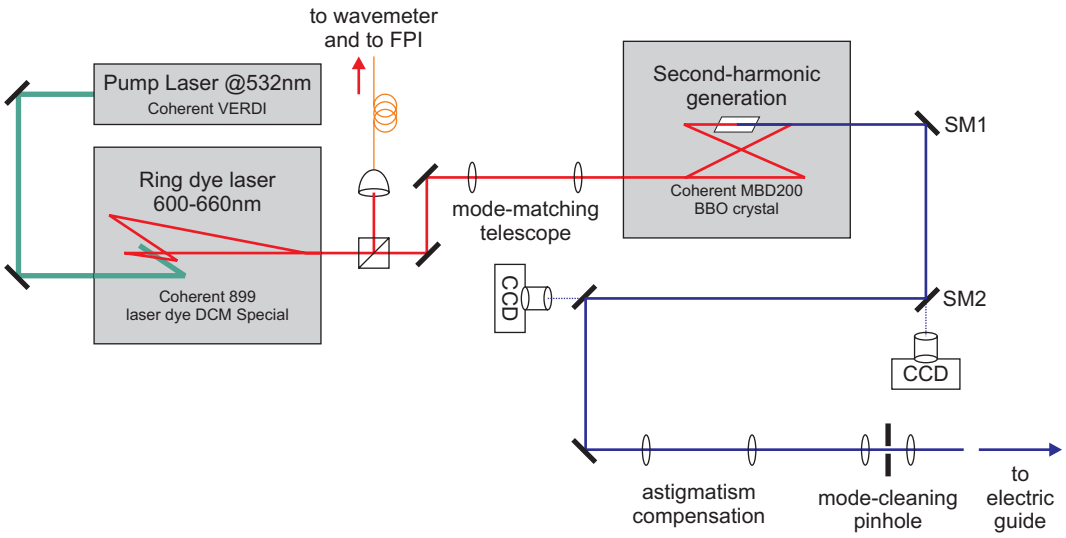

Figure 5.2: Laser setup. Tunable, narrow-bandwidth, continuous-wave (cw) laser light in the 330 nm wavelength range is produced by second-harmonic generation of the output of a ring dye laser. For wavelength control, a small part of the fundamental is coupled into single-mode optical fibers and sent to a wavemeter (HighFinesse WS7) and to a Fabry-Perot interferometer. A BBO crystal is placed in the focus of an enhancement cavity for the fundamental. To achieve phase matching between the fundamental and the second-harmonic radiation, the angle of the crystal relative to the propagation direction of the laser light is adjusted. The resonance frequency of the enhancement cavity is locked to the frequency of the fundamental by the Hänsch-Couillaud method [Hän80]. Since the beam-pointing of the produced UV light varies with wavelength, two CCD cameras are used to monitor the beam position. A beam-pointing deviation from the reference is then corrected with two steering mirrors (SM). To obtain a high-quality Gaussian beam profile, which can be properly aligned through the guide, the light is sent through two cylindrical lenses for astigmatism compensation and mode cleaned by a pinhole.

section before the QMS ionization unit the ultraviolet (UV) laser beam is overlapped with the guided molecular beam over a length of ≈ 15 cm.

The continuous-wave (cw) narrow-bandwidth tunable UV laser light is created by second-harmonic generation of light from a ring dye laser in an external enhancement cavity. The dye laser is locked to a temperature-stabilized reference cavity and its output frequency is monitored by a wavemeter. A schematic of the laser setup is shown in Fig. 5.2. After beam shaping and laser power switching by an electro-optical modulator, around 100 mW laser light at a wavelength of 330 nm is available for the experiment. The laser beam is focussed into the guide counter-propagating the molecules. The beam waist of 150–200 μm is optimized for minimal scattering of UV light on the high-voltage electrodes, which would lead to a pressure rise and consequently an increase in background count rate. After careful alignment no significant influence of the UV light on the QMS count rate is observed. Numerical simulations of the motion of molecules in the trapping field show a typical diameter

of the guided beam of $\approx 0.8\,\mathrm{mm}$, independent of the rotational state, causing most molecules to pass through the laser beam on their orbit.

5.2 Room-temperature absorption spectroscopy of formaldehyde

The ultraviolet spectrum of formaldehyde (H_2CO) has been extensively investigated already around the birth of molecular spectroscopy [Die34]. As one of the simplest polyatomic molecules it can be considered a model system for molecular physics. A variety of studies has been carried out to experimentally determine key parameters for formaldehyde photochemistry such as photodissociation quantum yields and absolute absorption cross sections. These numbers are relevant for atmospheric science, for which formaldehyde is an important molecule. Formaldehyde is present in the atmosphere at concentration of $\sim 50\,\mathrm{pptv}$ (parts per trillion by volume) in clean tropospheric air [Rie99] and up to 10–70 ppbv (parts per billion by volume) in the air in urban centers [Gro83, Wil96]. By excitation of the $\tilde{A}^1A_2 \leftarrow \tilde{X}^1A_1$ transition in the 260–360 nm wavelength range two dissociation channels [Moo83, Bow06] with high quantum yields [McQ69, Cla78, Hor78a, Hor78b, Rei78, Moo78] are open:

$$H_2CO + h\nu \rightarrow H_2 + CO \tag{5.1a}$$

$$H_2CO + h\nu \rightarrow H + HCO \tag{5.1b}$$

The reaction channel (5.1a) opens at wavelengths $<360\,\mathrm{nm}$, and the reaction channel (5.1b) opens at wavelengths $<330\,\mathrm{nm}$. The reaction products can then further react with other species present in the Earth's atmosphere. This UV-light-induced dissociation is used for the depletion spectroscopy, since it offers an internal-state-dependent loss mechanism for guided formaldehyde molecules.

5.2.1 Formaldehyde-spectroscopy setup

The experimental setup used for the absorption-spectroscopy measurements is standard [Dem03a]. However, due to the small absorption cross sections of formaldehyde ($\sigma \sim 10^{-19}\,\mathrm{cm}^2$), measurements must be performed at relatively high densities and long optical path lengths. As shown in Fig. 5.3, a home-made multipass setup using two spherical UV mirrors placed outside the vacuum chamber and one additional retroreflection mirror was used.

Vacuum-chamber setup

Connected to the vacuum chamber are a turbo molecular pump, a pressure gauge (Pfeiffer Vacuum, Compact Full Range Gauge PKR261), a flow valve for formaldehyde input, and a flow valve allowing analysis of the chamber's contents by a residual-gas analyzer (Pfeiffer Vacuum, Prisma QMS200). The effective pumping

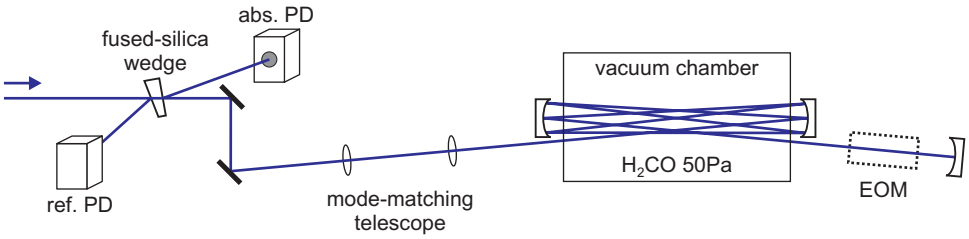

Figure 5.3: Room-temperature absorption-spectroscopy setup. A formaldehyde pressure of 50 Pa is maintained in the vacuum chamber which is used as an absorption cell. To achieve a large ($\approx$3.15 m) optical path length, a multipass, retroreflection configuration is utilized. For that purpose, curved mirrors refocus the beam into the spectroscopy chamber in a cavity-like manner. An additional curved mirror is used for retroreflection. Before being mode matched into the "cavity", part of the UV light is split off by a fused-silica wedge and directed on a UV-sensitive Si photodiode serving as a laser power reference (ref. PD). To obtain the absorption signal, the same fused-silica wedge sends a part of the backreflected light on another photodiode (abs. PD). An electro-optical modulator (EOM) can be placed in the backreflected beam for Doppler-free frequency-modulation spectroscopy [Zep07].

speed of the turbo molecular pump can be reduced by an angle valve placed between the recipient and the pump to avoid excess pumping of formaldehyde. With the turbo molecular pump the spectroscopy chamber is evacuated to a base pressure in the 10^{-6} mbar range.

Gaseous formaldehyde is prepared the same way as for the guiding experiments (see section 5.1). Since formaldehyde molecules dissociate upon UV excitation, a stable flow of formaldehyde is maintained by slightly opening the valve between the turbo pump and the vacuum chamber. The partial pressures of formaldehyde and its dissociation products are monitored with the residual-gas analyzer and the formaldehyde input flow rate as well as the flow to the turbo molecular pump are optimized for a constant ratio. This way measurements are performed at a constant formaldehyde concentration. In the experiment a constant pressure of 50 Pa ($= 5 \times 10^{-2}$ mbar) is maintained in the vacuum chamber, with a formaldehyde fraction estimated to be $\geq$50 %.

Optical setup, detection of the absorption signal, and laser-frequency tuning

To achieve a large optical path length in a relatively compact setup, a multipass and retroreflection configuration is used. The UV laser beam is initially focussed into the vacuum chamber with the beam parameters mode-matched to the effective cavity mode generated by the two multipass mirrors. Two curved mirrors with a radius of curvature (RoC) of 200 mm outside the vacuum chamber refocus the beam into the vacuum chamber, allowing 7 passes. All curved mirrors are positioned such

that their radius of curvature matches the Gaussian mode leaving the spectroscopy setup. By an additional retroreflection mirror (RoC = 500 mm), the effective path length can even be doubled, yielding ≈ 3.15 m in a compact ≈ 22.5 cm length vacuum chamber.

For detection a fused-silica wedge is placed near normal incidence which allows picking up part of the original beam used as power reference and part of the retroreflected beam containing the absorption signal. The picked-up beams are focussed on UV-sensitive Si photodiodes (Thorlabs PDA36EC).

To tune the laser frequency, a linear voltage ramp is applied to the external scan input of the dye laser. Thereby, the laser frequency is swept over 20 GHz in the fundamental with a scan speed of ≈ 45 GHz/s. For each of these sweeps the central frequency of the fundamental is measured with the wavemeter before and after the sweep, giving agreement within $0.001\,\mathrm{cm}^{-1}$ in the fundamental. For calibration of the scan speed, the transmission signal of a Fabry-Perot interferometer (FPI) is recorded. Subsequent scans are performed with a central-frequency difference of 10 GHz in the fundamental, giving 50 % overlap for concatenating individual sweeps.

Data acquisition and data analysis

A four-channel digital oscilloscope is used for data acquisition. Simultaneously, the external ramp, the FPI transmission peaks, the reference and absorption photodiode signals are recorded. For later data analysis the channels are rebinned to a resolution of 100 MHz in the UV, which was chosen such that individual rotational transitions, which are Doppler-broadened to 2.4 GHz, are well resolved. Overlapping adjacent scans using the central frequencies measured with the wavemeter show good overlap between lines present in both scans and confirm the central wavelength measurements with the wavemeter.

Modifications for Doppler-free measurements

The experimental setup used for Doppler-free measurements and the developed analytical model for the amplitude of Doppler-free peaks is described in detail by Martin Zeppenfeld et al. [Zep07]. Here only the modifications to the spectroscopy setup are summarized. To ease the detection of weak Doppler-free signals, frequency modulation (FM) spectroscopy [Bjo80, Bjo83] is performed. For this an electro-optical modulator (EOM, Leysop EM400K), resonantly driven with a frequency of 15.8 MHz for the creation of sidebands, is placed in the retroreflected beam (see Fig. 5.3). Since a demodulation of the signal at 15.8 MHz is necessary, fast photodiodes with a sufficiently high bandwidth are used for detection (Thorlabs PDA155). Furthermore, since the $\tilde{A}^1A_2 \leftarrow \tilde{X}^1A_1$ electronic transitions in formaldehyde are weak, high laser powers are needed to reach a significant saturation and discriminate the Lamb dips against the Doppler-broadened background. After careful tuning of the laser system, UV laser powers of 250–350 mW are available for the saturation-spectroscopy experiment.

5.2.2 Results and discussion

Previous measurements of the $\tilde{A}^1A_2 \leftarrow \tilde{X}^1A_1$ rovibrational band of formaldehyde aimed at the determination of absolute temperature-dependent absorption cross sections [Can90, Pop05, Smi06]. Other experiments studied the quantum yield of the dissociation processes following the UV excitation [McQ69, Cla78, Hor78a, Hor78b, Rei78, Moo78]. These cross sections and quantum yields are important parameters for the description of photochemistry in the atmosphere induced by the sunlight as discussed in the introduction. These measurements have been performed using either broadband light sources and spectrometers ([Can90] and references therein) with resolutions above $1\,\mathrm{cm}^{-1}$ or pulsed lasers with spectral resolutions of, e.g., $0.35\,\mathrm{cm}^{-1}$ [Pop05, Smi06]. An exception to this are the measurements by D. T. Co *et al.* [Co05] with a resolution of $0.027\,\mathrm{cm}^{-1}$, spanning the long wavelength range (351–356 nm) of the $\tilde{A}^1A_2 \leftarrow \tilde{X}^1A_1$ band, and the measurements of the $2_0^1 4_0^1$ and $2_0^2 4_0^1$ rovibrational band by M. Schulz [Sch04]. Except for these two experiments the resolution of previous measurements is not high enough to resolve individual rotational lines with a Doppler width of 2.4 GHz at room temperature.

Comparison to previous studies

The improvement in resolution compared to previous studies [Smi06] with a resolution of $0.35\,\mathrm{cm}^{-1}$ is shown in Fig. 5.4, where the region around the band heads of the ${}^rR\,K_a''=3$ progression at $\approx 30389\,\mathrm{cm}^{-1}$ and the ${}^rR\,K_a''=4$ progression at $\approx 30397\,\mathrm{cm}^{-1}$ with many lines close together are shown. Individual rotational lines are well resolved and accurate line positions as well as intensities can be determined. For the figures shown the measured data is binned to a resolution of 100 MHz = $0.003\,\mathrm{cm}^{-1}$ which is sufficient to resolve the Doppler-broadened lines.

C. A. Smith *et al.* [Smi06] used a lineshape function with a full width at half maximum (FWHM) of $0.45\,\mathrm{cm}^{-1}$ to reproduce their measured spectra from simulations. This was surprising since the UV linewidth of their laser sources was expected to be $\leq 0.20\,\mathrm{cm}^{-1}$ as calculated from the measured linewidth of the fundamental. It was speculated that this could either be explained by extremely short excited state lifetimes not in agreement with literature values [Moo83] or by an additional technical broadening. From our data a width of 2.4 GHz FWHM is determined for isolated lines across the whole frequency range, being in good agreement with a Doppler-broadened line profile at room temperature (293 K). Therefore, these extremely short lifetimes can be ruled out, and their assumption of a larger laser linewidth is confirmed.

Fit of the $2_0^1 4_0^3$ and $2_0^2 4_0^1$ rovibrational band

For the fit of the molecular parameters to the experimental spectrum, Watson's A-reduced Hamiltonian [Wat67, Wat68] including quartic and sextic centrifugal distortion terms has been used with a genetic algorithm (GA) as optimizer. Details

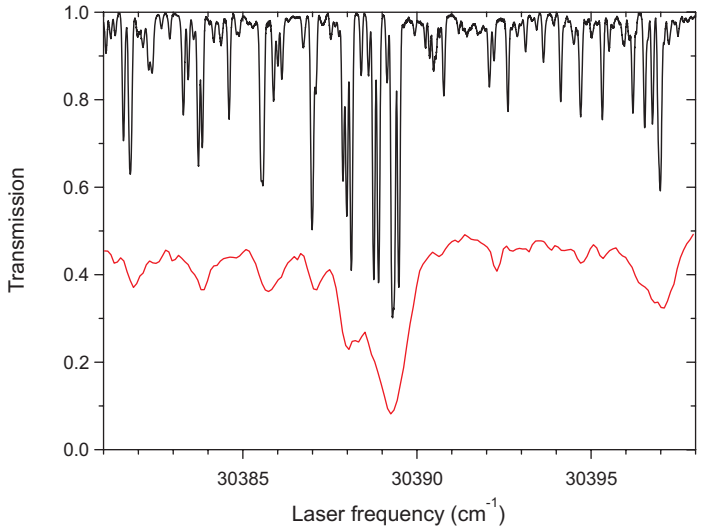

Figure 5.4: Comparison in resolution of our absorption data (top) to previous measurements (bottom). The measurements by C. A. Smith *et al.* [Smi06] with the so-far reported highest resolution in this wavelength range are chosen as reference. A wavelength range with many lines close together, converging to the bandheads of the ${}^{r}R\,K_a''=3$ progression at $\approx 30389\,\mathrm{cm}^{-1}$ and ${}^{r}R\,K_a''=4$ progression at $\approx 30397\,\mathrm{cm}^{-1}$, was selected to show how individual lines can be resolved now. The data of C. A. Smith *et al.* are offset by 0.5 for clarity.

about the GA and the cost function used for evaluation of the quality of the fit can be found in Refs. [Mee04, Mee06b, Mee06a]. Table 5.1 compiles the so-determined parameters and compares them to the previous parameters for the ground state [Clo83] and the excited vibronic states [Smi06]. The ground-state parameters are in excellent agreement with the values that have been deduced from microwave frequencies and combination differences in infrared and electronic spectra, weighted by appropriate factors [Clo83]. The parameters for the $2_0^1 4_0^3$ and $2_0^2 4_0^1$ vibronic bands are compared to the values given by C. A. Smith *et al.*. To improve the quality of the fit, the experimental data above $30390\,\mathrm{cm}^{-1}$ have been excluded from the fit of the $2_0^1 4_0^3$ vibronic band, since strong perturbations of the line positions between 30390 and $30404\,\mathrm{cm}^{-1}$ were observed. The reason why exclusion of a part of the data was necessary might be an interference with the weak vibronic $2_0^1 4_0^1 6_0^1$ band with its origin at $30395\,\mathrm{cm}^{-1}$. Although this band was included with the molecular parameters from [Ape85] as starting values in our fit, no improvement of the cost function could be obtained by this combined fit. Due to the high temperature, high J-states are populated and sextic centrifugal distortion terms in the fit have shown to be necessary. The appropriate nuclear spin statistics (K_a even levels = 1; K_a odd levels = 3) have been taken into account. For comparison, parts of the simulated and the measured absorption spectrum around the band origin are shown in Fig. 5.5.

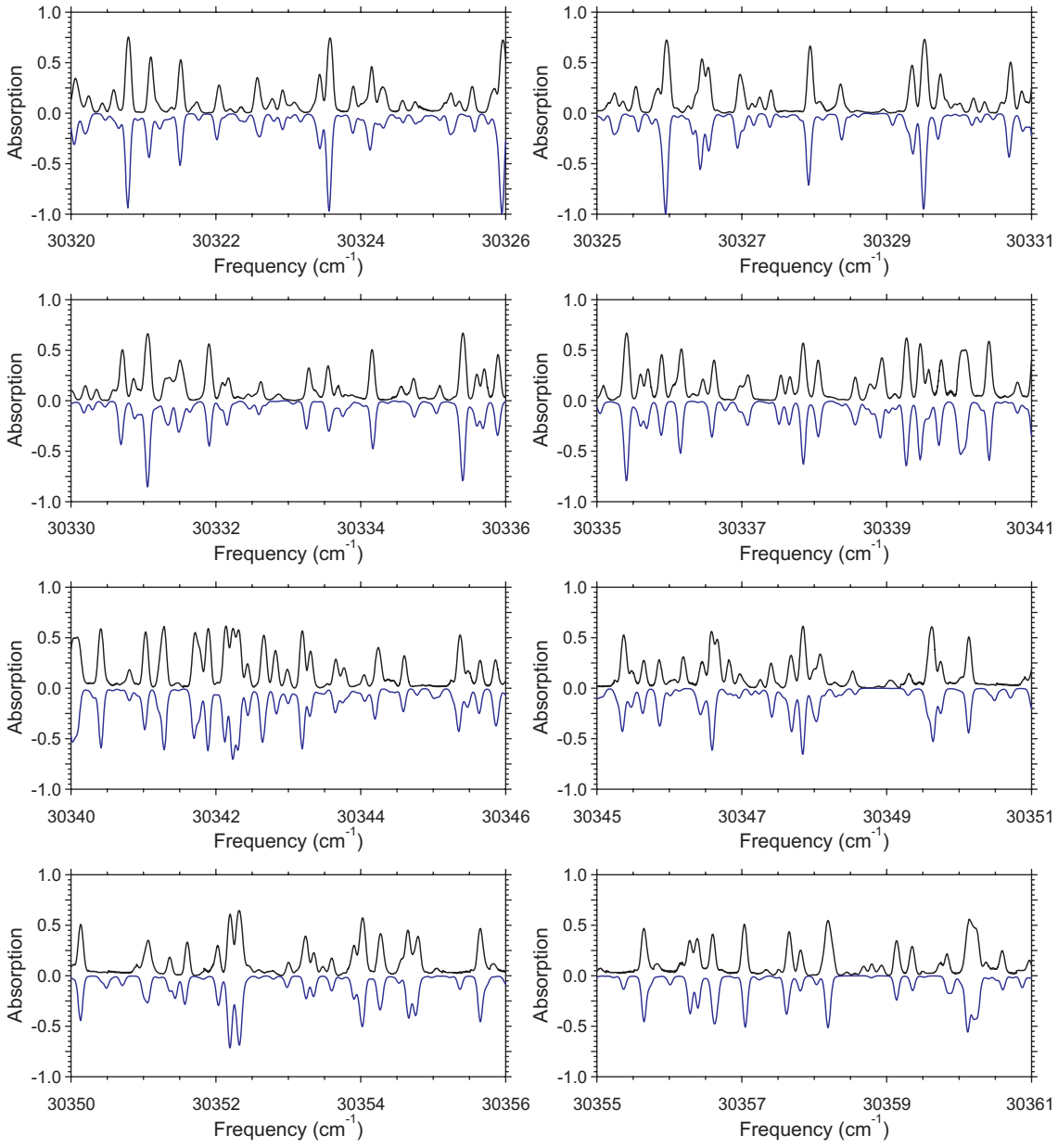

Figure 5.5: Comparison between the measured absorption spectrum (top) and the simulation (inverted, bottom) around the origin of the $2_0^1 4_0^3$ vibrational band at 30340.08 cm^{-1}.

Table 5.1: Molecular parameters of the ground state and the $\tilde{A}^1$ excited state of formaldehyde from a GA-Fit of the $2_0^1 4_0^3$ and $2_0^2 4_0^1$ vibronic bands. All values are given in MHz.

	GA-Fit $2_0^1 4_0^3$	GA-Fit $2_0^2 4_0^1$	Ref. [Clo83]	$2_0^1 4_0^3$Ref. [Smi06]	$2_0^2 4_0^1$Ref. [Smi06]
A''	281970.85(27)	281971.44(43)	281970.572(24)	-	-
B''	38836.53(27)	38836.14(25)	38836.0455(13)	-	-
C''	34002.67(16)	34002.57(25)	34002.2034(12)	-	-
$10^3 D''_J$	75.38(7)	75.61(11)	75.295(21)	-	-
$10^3 D''_{JK}$	1290.24(20)	1290.00(29)	1290.50(37)	-	-
$10^3 D''_K$	19424.6(6)	19424.1(6)	19423(7)	-	-
$10^3 d''_J$	9.85(24)	10.30(25)	10.4567(9)	-	-
$10^3 d''_K$	1028.39(60)	1027.68(66)	1026.03(25)	-	-
$10^9 H''_J$	33.5(16)	34.1(20)	31(21)	-	-
$10^9 H''_{JK}$	29021(1)	29022(1)	29019(690)	-	-
$10^9 H''_{KJ}$	-112184(3)	-112179(3)	-112000(280000)	-	-
$10^9 H''_K$	4470000(2500)	4470000(4100)	4500000(200000)	-	-
$10^9 h''_J$	45.3(14)	40.1(9)	42.3(17)	-	-
$10^9 h''_{JK}$	15592(5)	15612(6)	15665(310)	-	-
$10^9 h''_K$	1372119.6(24)	1372119.5(36)	1372000(18000)	-	-
ν_0	909572633(41)	919120592(48)	-	909571763(1110)	919120745(690)
A'	246402.8(40)	259111.6(43)	-	246669(90)	259090(21)
B'	33158.0(19)	32952.3(33)	-	33194(21)	32918(16)
C'	30268.8(23)	29764.4(39)	-	30277(21)	29837(14)
$10^3 D'_J$	145.9(44)	89.6(9)	-	188(17)	99(12)
$10^3 D'_{JK}$	3204(52)	1617(14)	-	4886(450)	1484(45)
$10^3 D'_K$	-43024(63)	9474(98)	-	-48237(1919)	9383(33)
$10^3 d'_J$	-9.8(40)	23.1(27)	-	49(14)	10(12)
$10^3 d'_K$	16350(700)	190(380)	-	11892(4497)	-6175(959)
$10^9 H'_J$	6480(9970)	16(18)	-	-	-
$10^9 H'_{JK}$	-20000(12000)	30000(5400)	-	-	-
$10^9 H'_{KJ}$	150000(80000)	158000(88000)	-	-	-
$10^9 H'_K$	8770000(620000)	3240000(640000)	-	-	-
$10^9 h'_J$	-24100(8500)	51(12)	-	-	-
$10^9 h'_{JK}$	28100(2100)	14200(6200)	-	-	-
$10^9 h'_K$	3130000(490000)	1490000(107000)	-	-	-

Rotational state $\lvert J, \tau, M\rangle$	ΔW^{s} (cm^{-1})	p_{S} (%)	p_{G} (%)
$\lvert 3, 3, 3\rangle$	2.86	0.252	8.52
$\lvert 4, 2, 4\rangle$	2.28	0.230	4.93
$\lvert 1, 1, 1\rangle$	1.29	0.531	3.62
$\lvert 3, 3, 2\rangle$	1.82	0.252	3.46
$\lvert 2, 2, 2\rangle$	2.42	0.134	3.22
$\lvert 5, 1, 5\rangle$	1.90	0.205	3.05

Table 5.2: Properties of selected rotational states $|J, \tau, M\rangle$ of formaldehyde with a population $\geq 3\%$ in the guided beam. ΔW^{s}: Calculated Stark shift at an electric field of 100 kV/cm. p_{S}: Thermal population in the effusive source at a temperature of 150 K. p_{G}: Population in the guided beam at an applied trapping electric field of 100 kV/cm. Note the increase of population of these rotational states in the guided beam relative to their contribution in the source by a factor of 10 to 35.

5.3 Internal-state distribution of guided formaldehyde molecules

The internal-state distribution of guided molecules is determined by the thermal population in the effusive source, including nuclear spin statistics, and by the Stark shift of the rotational states in the applied guiding fields, as explained for the water isotopologs in section 4.2. For formaldehyde, which is also an asymmetric rotor, the Stark shift ΔW^{s} can be calculated the same way as described for the water isotopologs in section 4.1. The measurements with formaldehyde are performed with a reservoir pressure of 0.1 mbar, i.e., in the medium pressure regime, same as for the water isotopologs. At this intermediate pressure setting, the contribution of a rotational state $|J, \tau, M\rangle$ to the signal of guided molecules is proportional to the square of its Stark energy $(\Delta W^{\mathrm{s}}(E_{\mathrm{max}}))^2$ at the maximal trapping field E_{max}. The Stark shifts at a typical trapping field of 100 kV/cm and the populations of rotational states in the guide are listed in Tbl. 5.2 for those states which contribute more than 3 % to the total flux at a source temperature of 150 K.

5.3.1 Depletion spectroscopy of individual rotational states

With the detailed understanding of the formaldeyhde spectrum gained by the room-temperature absorption-spectroscopy experiment described in section 5.2, individual rotational states in the guided beam are accessible. Table 5.3 lists the transitions used to address the highest-populated states in the guided beam. Mainly the R-branch out of the $2_0^1 4_0^3$ vibrational band is used, because the frequency difference between transitions originating from different initial states is smallest for this branch, allowing easier tuning of the laser. Upon excitation with the UV light the molecules dissociate and a decrease in the QMS signal is detected as shown in Fig. 5.6. At the

$\lvert J, \tau\rangle$	$\tilde{X}^1A_1 \rightarrow \tilde{A}^1A_2$ $\lvert J'', K_a'', K_c''\rangle \rightarrow \lvert J', K_a', K_c'\rangle$	Frequency (cm^{-1})
$\lvert 1, 1\rangle$	$\lvert 1, 1, 0\rangle \rightarrow \lvert 2, 2, 1\rangle$	30364.38
$\lvert 2, 2\rangle$	$\lvert 2, 2, 0\rangle \rightarrow \lvert 3, 3, 1\rangle$	30377.26
$\lvert 3, 3\rangle$	$\lvert 3, 3, 0\rangle \rightarrow \lvert 4, 4, 1\rangle$	30387.98
$\lvert 4, 2\rangle$	$\lvert 4, 3, 1\rangle \rightarrow \lvert 5, 4, 2\rangle$	30388.76
$\lvert 5, 1\rangle$	$\lvert 5, 3, 2\rangle \rightarrow \lvert 5, 4, 1\rangle$	30376.62
$\lvert 5, 5\rangle$	$\lvert 5, 5, 0\rangle \rightarrow \lvert 6, 6, 1\rangle$	30403.84

Table 5.3: Transitions used to address the highest-populated states in the guided beam.

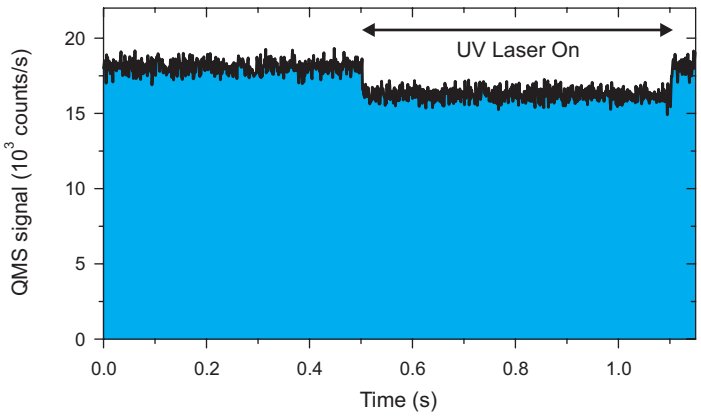

Figure 5.6: Depletion in the QMS signal of guided formaldehyde molecules at an electrode voltage of ±1 kV. The UV light is switched on between 0.5 and 1.1 s. The laser light is tuned to the maximum of the transition $|3, 3, 0\rangle \rightarrow |4, 4, 1\rangle$ at this guiding electric field. This frequency was determined by a line-shape measurement as the one shown in Fig. 5.7 (a).

wavelengths of ≈ 330 nm used for the experiments, the efficiency for dissociation is >90 % [Moo83].

When scanning the laser frequency around the frequency of the transition in zero electric field, an asymmetric line shape is observed as shown in Fig. 5.7 (a). In the guided beam, several effects lead to line broadenings and line shifts of the depletion signal. Since the molecules move with a typical velocity on the order of 100 m/s, they experience on average a Doppler shift of -300 MHz. Additionally, the lines are broadened due to the velocity spread of the molecules in the guided beam. However, the main effect on the line shape originates from the radial position dependence of the electric field experienced by the molecules and the resulting differences in Stark shifts. Taking into account the radial distribution of the molecular beam determined from simulations and the measured laser beam diameter, the line shape can be reproduced as shown by the solid curve in Fig. 5.7 (a). In the diploma thesis

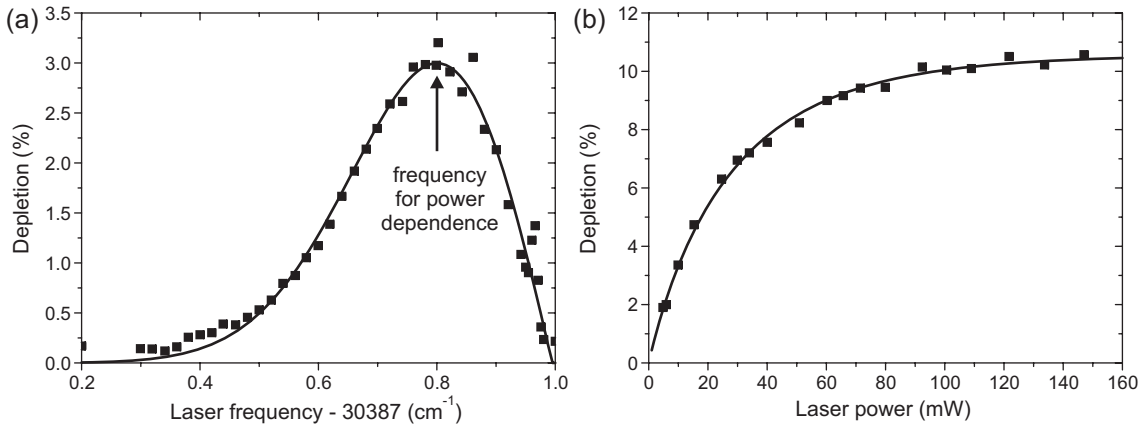

Figure 5.7: (a) The transition $|3,3,0\rangle \rightarrow |4,4,1\rangle$ measured at an electrode voltage of $\pm 5\,\mathrm{kV}$. The solid curve is a fit to the data taking into account the laser beam profile as well as the distribution of the guided molecules in the inhomogeneous electric fields present in the spectroscopy section. For the power-dependence measurements, the laser frequency is set to the maximum of the curve as indicated. (b) Laser-power dependence of the depletion signal. The laser frequency is fixed to the maximum of the transition $|3,3,0\rangle \rightarrow |4,4,1\rangle$ measured at an electrode voltage of $\pm 1\,\mathrm{kV}$. The solid curve is a fit using the model for $\Delta(P)$ described by Eq. (5.2).

of Markus Schenk, these effects are discussed in detail and measurements for the different addressed states are shown [Sch07a].

Since the electric fields in the quadrupole guide vary in strength and direction, it is not possible to irradiate the molecules with a well-defined polarization with respect to the guiding electric field. If for a given state $|J,\tau\rangle$ more than one M component contributes to the flux of guided molecules, this leads to additional line broadening and makes it impossible to depopulate the different M states independently. Instead, a signal integrated over all guided M states of the state $|J,\tau\rangle$ is measured.

To obtain the saturated depletion signal, which is a measure for the population of a rotation state, the laser frequency is fixed to the maximum of the transition in the guiding field as indicated in Fig. 5.7. Then, the laser power is varied and the value of the depletion reached in the limit of high laser power is extracted as shown in Fig. 5.7 (b). To reach saturation with the available laser power, the electrode voltage is set to a relatively small value of $\pm 1\,\mathrm{kV}$, resulting in smaller line broadenings. Since the interaction time with the laser beam is velocity dependent, the absorption probability for low laser intensities scales as $1/v$. Taking this velocity-dependent absorption probability into account, the laser-power dependence of the depletion signal can be described by

$$\Delta(P) = N_0 \cdot \left[1 - \int_0^{v_{\mathrm{l,max}}} n(v)\exp(-\alpha P l/v)dv\right], \tag{5.2}$$

where N_0 represents the relative population of the specific state addressed by the laser, $n(v)$ is the normalized longitudinal velocity distribution, P is the laser power,

α is a transition strength factor and l is the interaction length. In the diploma thesis of Markus Schenk detailed measurements of the laser-power dependence for all the addressed transitions are presented [Sch07a].

5.3.2 Internal-state distribution in the guided beam

As discussed in section 4.2, the contribution of individual internal states to the total flux in the guided beam is determined by the Stark shift of the specific state and its population in the effusive source. The population $p_{J\tau M}$ of a rotational state $|J, \tau, M\rangle$ in the thermal source depends on the source temperature T as

$$p_{J\tau M} = \frac{1}{Z} g_M g_I \exp\left(-\frac{E_{J\tau M}}{k_B T}\right). \tag{5.3}$$

Here, Z is the partition function $Z = \sum_{J\tau M} g_M g_I \exp\left(-E_{J\tau M}/k_B T\right)$, $E_{J\tau M}$ is the rotational energy, g_M the M degeneracy factor of the state, and g_I the nuclear spin degeneracy factor. The contribution of a rotational state with Stark shift $\Delta W^{\mathrm{s}}_{J\tau M}$ at the applied trapping field $E_{\max}$ to the flux of guided molecules is expressed as

$$f_{J\tau M} = \frac{1}{N} p_{J\tau M} \left(\Delta W^{\mathrm{s}}_{J\tau M}\right)^2, \tag{5.4}$$

where N assures normalization of the total flux, $N = \sum_{J\tau M} p_{J\tau M} \left(\Delta W^{\mathrm{s}}_{J\tau M}\right)^2$.

Figure 5.8 (a) shows the calculated temperature dependence of the contribution of individual states $|J, \tau\rangle$ to the guided beam. In this figure, the populations of the individual M states $|J, \tau, M\rangle$ contributing to a given state $|J, \tau\rangle$ are summed up, since these are not resolved in the experiment. As expected, decreasing the source temperature increases the contributions of the individual rotational states, as long as their rotational energy is smaller as or comparable to the source temperature. Only for the state $|5, 5\rangle$, which has a high rotational energy of $241.2\,\mathrm{cm}^{-1}$, reducing the temperature decreases the population in the thermal source and hence its contribution to the guided beam.

The experimentally determined population of individual guided states for $\pm 1\,\mathrm{kV}$ electrode voltage are shown in Fig. 5.8 (b). As a measure for the population of a rotational state the steady-state value of the depletion signal obtained at high laser power is used, as shown in Fig. 5.7 (b). For each temperature of the source, the data is normalized to the state with maximal contribution, $|3, 3\rangle$. Without this normalization, the measured magnitude of the depletion signal is systematically lower by 20% as compared to the calculated populations of the rotational states. This value was found to be independent of the addressed state. This difference is attributed to molecules spiraling in elliptic orbits which never become resonant with the laser beam or which never traverse the laser beam, and to molecules which do not dissociate and can still be guided after decaying back to a guidable state in the electronic ground state. By varying the temperature between 150 and 300 K, the internal state distribution of the formaldehyde molecules as well as their velocity distribution in

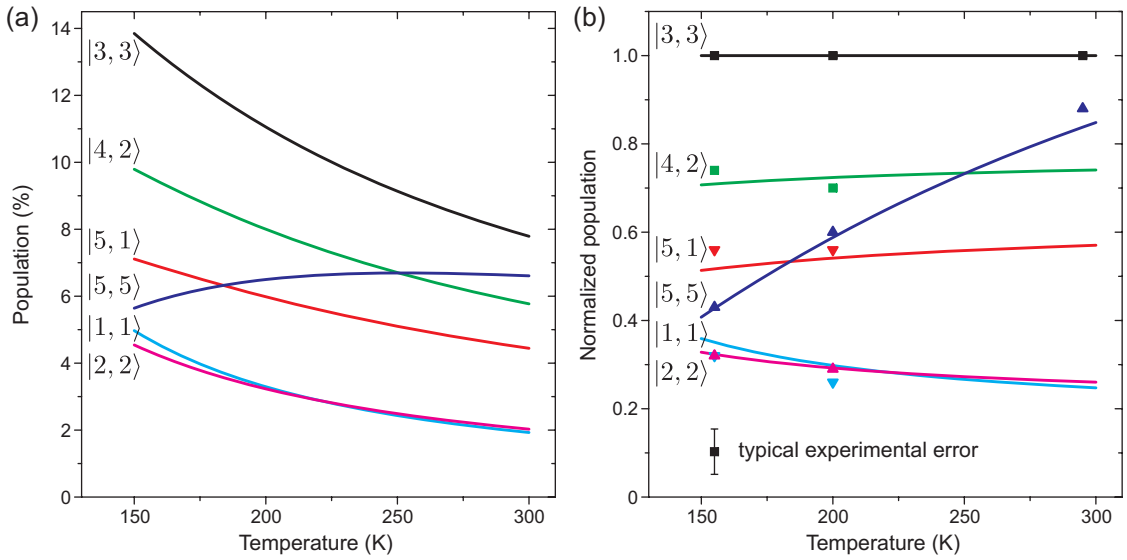

Figure 5.8: Temperature dependence of the population in the states $|J, \tau\rangle$ with largest contributions to the guided beam. In this figure the sum over all M states is taken, since these are not resolved in the experiment. This is in contrast to Tbl. 5.2, which lists the contribution of individual states $|J, \tau, M\rangle$. (a) Calculated population of rotational states for a guiding electric field of 20 kV/cm. (b) Experimentally determined and calculated populations, normalized to the population of the state $|3, 3\rangle$. The data were taken at ± 1 kV electrode voltage, and for the calculations a guiding electric field of 20 kV/cm was assumed.

the source is modified. For decreasing source temperature, the reduction of the molecules' mean velocity is directly evident from an increase in guided flux. The good agreement between the data and the calculated temperature dependence of the internal state distribution confirms thermalization of the molecules' rotational temperature in the cooling stage attached to the ceramic nozzle. An interesting feature visible in the experimental data is the increasing contribution of the state $|5, 5\rangle$ for higher temperature. As already discussed for the calculations shown in Fig. 5.7 (a), due to its high rotational energy of 241.2 cm^{-1} this state is less occupied at low temperatures as compared to the other states which were studied. For higher temperatures, the relative thermal population of this state increases. Furthermore, this state contributes strongly to the guided beam due to its many M states with moderate or even large Stark shifts.

To characterize the internal state distribution, it would be desirable to use just one basic quantity such as a temperature. Finding a good description of the internal temperature of the guided beam is, however, non-trivial. For a source temperature of 150 K the mean rotational energy of the guided beam is 163.6 cm^{-1}, which is determined from the calculated state populations. This correspond to the internal temperature of a thermal ensemble at a temperature of 155 K. The mean rotational energy is, however, not a good measure for the purity of the beam, because the

filtering process relies on the Stark shifts of the internal states of the molecules. Therefore, the guided ensemble is non-thermal. Hence, as a measure for the purity of the guided beam the entropy $S = -\sum p_i \log p_i$ is determined from the calculated populations p_i of all guided states. This entropy of the guided ensemble is then compared to the entropy of a thermal ensemble. In this calculation states up to J=12 are included, which was found to be sufficient. The temperature, at which a thermal gas has the same entropy, can then be defined as entropic temperature T_e of the guided beam. For a source temperature T of 150 K one finds $T_e \approx 31$ K, for $T = 200$ K one finds $T_e \approx 38$ K, and for $T = 300$ K one finds $T_e \approx 47$ K. For molecules with quadratic Stark shifts, such as H_2O or D_2O, the number of contributing states is even smaller due to stronger selection in the filtering process as discussed in section 4.2 [Rie06, Mot09b]. Therefore, even when then molecules are extracted from a thermal reservoir the purity of the guided beam in terms of populated internal states is already considerably improved.

5.4 Summary

Depletion spectroscopy constitutes a powerful tool to experimentally access the internal state distribution of guided molecules. As shown for guided formaldehyde molecules, the experimentally measured rotational-state distribution and theoretical predictions based on thermal source populations and calculations of Stark shifts are in good agreement. Measurements for varying source temperature show that by reducing the temperature of the reservoir, from which the molecules are extracted, the purity of the guided beam can be improved. Depletion spectroscopy as a method for internal-state diagnostics in a cold guided beam is not restricted to formaldehyde and should be applicable to other molecular species as well.

Furthermore, depletion spectroscopy is not only a tool for internal state diagnostics. For example, it can be used for spectroscopy of species which are hard to study in the gas phase. Collinear spectroscopy in a cold guided beam has the advantage of long interaction times and good overlap with the slow molecular beam, making it a good choice for studies of weak transitions. Since the electrostatic guide produces a continuous flux of molecules, it is a natural choice for combination with narrow-band cw lasers. Using a higher-order multipole guide, it should be possible to probe molecular transitions in more homogeneous electric fields, resulting in narrow lines, and allowing for example measurements of dipole moments of electronically excited states. Moreover, by applying a DC electric bias field, spectroscopy of oriented polar molecules should be possible.

Chapter 6

Cavity-enhanced Rayleigh scattering

In this chapter, the effect of an optical cavity on Rayleigh scattering [Ray99, vdH81, Boh83] is discussed. The motivation for this work is twofold: First of all, studying the influence of an optical cavity on the Rayleigh-scattering rate of some polarizable particle allows to investigate the classical nature of the Purcell effect [Pur46], to which often some "quantumness" is ascribed. This aspect is interesting mainly from a conceptual point of view. Secondly, the experiment constitutes a first step towards non-destructive, in-situ detection of cold molecules by an optical cavity, being an extension of the efficient detection of single atoms by an optical cavity [Mün99a, Mün99b].

In the electrostatic velocity-filtering and guiding experiments described in chapter 2–5 of this thesis, the cold molecules were ionized by electron impact. The produced ions were then mass filtered and counted after having been amplified by a secondary-electron multiplier. Although being a very general approach, which is even extendable by depletion spectroscopy to a state-specific detection method, it has the disadvantage of being generically destructive. This is a problem common to other experiments producing cold molecules as well. For example, molecules produced from ultracold atomic ensembles utilizing a Feshbach resonance must be converted back to atom pairs for imaging with laser light resonant with an atomic cycling transition [Lan08]. Alternatively, the molecules can be photoionized, such that subsequent single-ion detection can be performed [Dei08b].

Cavity-enhanced Rayleigh scattering might represent an alternative to these destructive detection techniques. Since the laser light is far detuned from any molecular resonance, the molecules behave completely classically. Therefore, the scattering process can be described as light scattering from a classical oscillating dipole, bearing the advantage of being nonsensitive to the specific molecular level structure and therefore widely applicable. Since far-detuned light scattering, i.e., Rayleigh scattering, is weak as for instance compared to resonant scattering in alkali atoms, collecting a large fraction of scattered light is essential. This is most straightforwardly

achieved using a lens with a large numerical aperture, thereby covering a large solid angle. An alternative and more powerful approach is to couple the scattering object to an optical resonator, even if the relevant light mode of the cavity covers only a small solid angle. The potential offered by the resonator comes from the Purcell effect [Pur46], generally associated with the enhancement of the spontaneous emission rate of an excited particle by means of mirrors. Although spontaneous emission is a quantum-mechanical phenomenon, it was argued that the modification of its rate by the resonator can be explained classically as a light interference effect [Kas62, Mil73, Dow93]. It therefore appears natural that the Purcell enhancement is a universal phenomenon, occurring both for light scattering from quantum objects (with discrete energy levels) and classical objects (oscillating dipoles). However, while quantum-mechanical experiments on the Purcell effect exist, the effect of a cavity on the classical light-scattering properties has been hardly studied. In a recent experiment, a subwavelength object was placed in the vicinity of a microresonator [Maz07]. Here, the scattering of far-detuned light into the cavity mode was described by a semiquantum model for the interaction between the classical oscillating dipole and the quantized modes of the light field. But this leaves open the question about the classical nature of the Purcell effect. Equally important, a demonstration of the Purcell effect for the detection of extremely weak signals in this classical regime is still lacking.

The experimental setup used to investigate the cavity enhancement of Rayleigh scattering is presented in section 6.1. First data showing the dependence of the light scattered from the polarizable particles on the detuning of the cavity with respect to the pump beam are discussed in section 6.2. In section 6.3 a model for the cavity enhancement based on the interference of classical scattered electromagnetic fields is developed, showing that no quantum effects are needed to explain an enhanced emission rate in a resonator. The actual experimental verification of cavity enhancement is presented in section 6.4. Here, the influence of the cavity on the power of the light scattered from thermal atomic (Xe), homonuclear (N_2) or heteronuclear (CF_3H) molecular gases is discussed. For different values of the cavity finesse, the Rayleigh-scattering rate is measured and compared to the predictions of a completely classical model based on the interference of intracavity light waves. This proves that the Purcell effect is classical and that an explanation in terms of a modified local mode density is not needed. The power of the light scattered into the cavity is also compared to that scattered into the same solid angle in free space, resulting in an enhancement by a factor of up to 38. The ability to enhance extremely small light scattering rates opens up new perspectives, e.g., for ultracold molecules research, which are discussed in section 6.5.

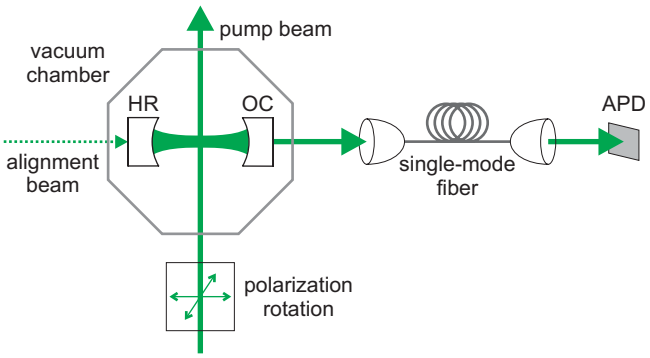

Figure 6.1: Experimental setup. The cavity consists of a high-reflective mirror (HR) and an output-coupling mirror (OC) in a vacuum chamber, which can be filled with various gases. The polarization direction of the linearly-polarized pump beam is rotated by a Pockels cell. The beam waist is adjusted to match the waist of the fundamental cavity mode TEM_{00}. Scattered light leaking out of the cavity through the OC is mode matched into a single-mode fiber, and then detected by an avalanche photodiode (APD).

6.1 Experimental setup

A schematic drawing of the experimental setup is shown in Fig. 6.1, whereas Fig. 6.2 shows some photographs of the actual experimental setup used. In the experiment, a 10 W single-frequency laser at a wavelength λ=532 nm was used. This wavelength was chosen as a compromise between the λ^{-4} dependence of the Rayleigh scattering cross section on the laser wavelength, available laser power, and sufficient detuning from deep-ultraviolet electronic transitions of the used species. The cavity is 0.6 cm long and the mirrors' radius of curvature is 4.5 cm. This combination results in a spacing of transverse modes of 4.1 GHz, larger than the observed Doppler widths. The cavity length is tuned by a piezoelectric tube separating the mirrors. To modify the cavity finesse, the mirror on the outcoupling side is exchanged, while on the opposite side the high-reflectivity mirror (HR, R=99.7 %) is used for all measurements. For the various combination of mirrors with measured intensity reflectivities R=(99.7 %, 98.9 %, 95.9 %), a cavity finesse of $\mathcal{F}$=(1000, 400, 100) is determined from the cavity line width as observed in transmission. The cavity is placed inside a vacuum chamber, which is pumped out to 10^{-2} mbar before various gases consisting of atoms (Xe), homonuclear (N_2) or heteronuclear molecules (CF_3H) are introduced via a valve. The focus of the pump beam was measured to be $\approx 50\,\mu$m, comparable to the calculated cavity-mode diameter $w_0 \approx 45\,\mu$m. Since the scattering particles are pumped with a power of up to 5 W and a scattered power into the cavity mode of a few fW is expected, suppression of stray light is crucial. Towards this end, light leaving the cavity on the output side is coupled into a single-mode fiber, which is aligned for optimal transmission of the TEM_{00} fundamental cavity mode. Behind the fiber, the light is detected by an avalanche photodiode operated in single-photon-counting mode.

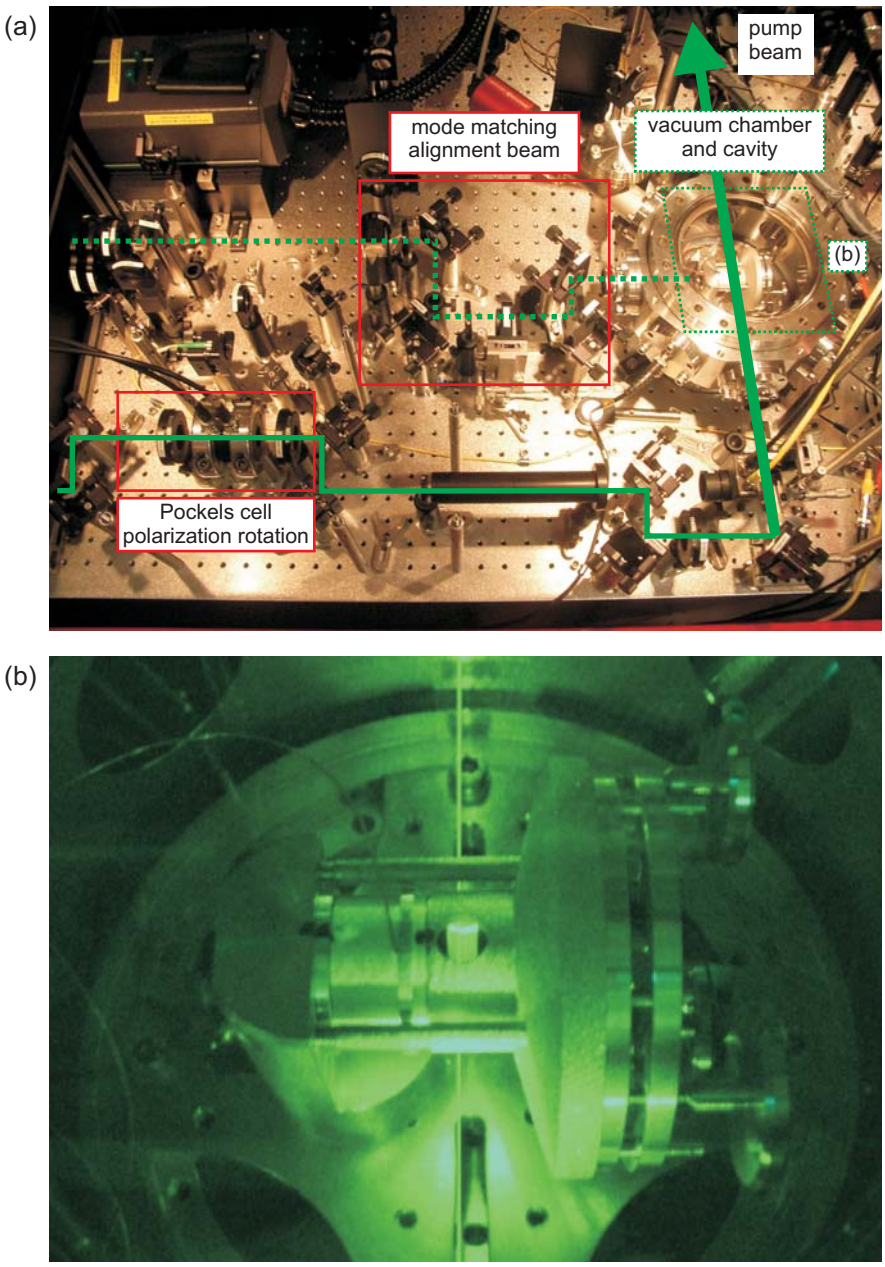

Figure 6.2: Photographs of the experiment. (a) The mode-matching setup for the alignment beam coupled into the cavity on-axis, and the Pockels cell for polarization rotation of the pump beam are highlighted. Since the light is reflected off dielectric mirrors between the Pockels cell and the viewport of the vacuum chamber, correct polarization rotation was verified after the pump beam had passed through the vacuum chamber. (b) Close-up of the cavity with the pump beam passing between the two mirrors. On the right-hand side, the adjustable mirror mount for the outcoupling mirror can be seen. Apart from easing the alignment, this allows to set the cavity length to the desired value, e.g., to achieve a confocal configuration. The piezoelectric tube permitting fine tuning of the cavity length is located left of the intersection between the pump beam and the cavity axis.

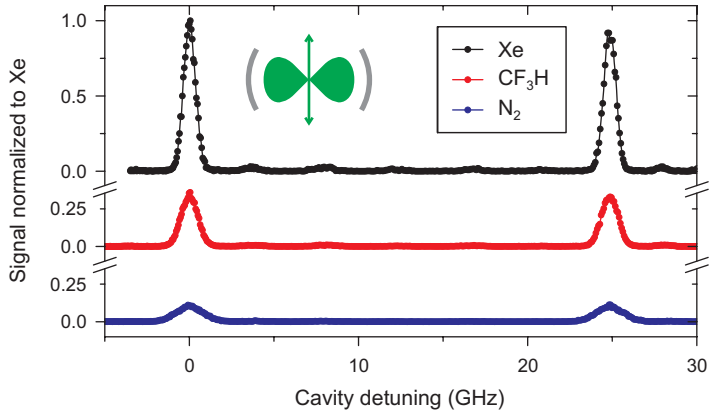

Figure 6.3: Cavity output measured behind the single-mode fiber. The signal of the individual gases is normalized to the signal obtained with Xe. The line profile originates from the Doppler broadening of the light scattered by the thermal gases.

6.2 Cavity mode spectrum

In the experiment, the pump beam is aligned perpendicular to the cavity axis as indicated in Fig. 6.1, the cavity is scanned over at least one free-spectral range, and the intensity of the light leaking out of the cavity is monitored. As shown in Fig. 6.3, mainly light scattered into the TEM_{00} mode, which is selected by the single-mode fiber, is observed. Some residual signal of light scattered into other cavity modes is present due to imperfect mode matching into the fiber. For the various gases used, the peaks show different heights and widths. The different widths originate from the differing masses of the thermal gases and, hence, the differing Doppler broadenings of the thermal gases. The different heights are caused by the specific polarizabilities of the differing scattering particles as well as by the frequency overlaps of the cavity mode with the Doppler profiles. Within experimental accuracy, the background signal observed in the measurements with N_2 and CF_3H agrees with the one obtained for Xe. Doppler broadening and the multitude of thermally populated internal molecular states prevents the resolution of the Raman spectrum, which could benefit from a cavity enhancement as well [Mor07].

A signature of Rayleigh scattering is the characteristic $\sin^2\theta$ polarization dependence when driven by linearly-polarized light. Using a Pockels cell, the polarization direction of the pump beam is rotated with respect to the cavity axis. Figure 6.4 shows the polarization dependence of light scattered into the TEM_{00} mode of the cavity. It follows a $\sin^2\theta$ dependence, as expected for emission from a classical oscillating dipole. When the polarization direction is aligned with the cavity axis ($\theta = 0°$), no Rayleigh scattering into the cavity mode is expected due to the small solid angle of the cavity covering only the nodal line of the dipole pattern. The residual signal amplitude of 1–2 % can be explained by imperfect linear polarization

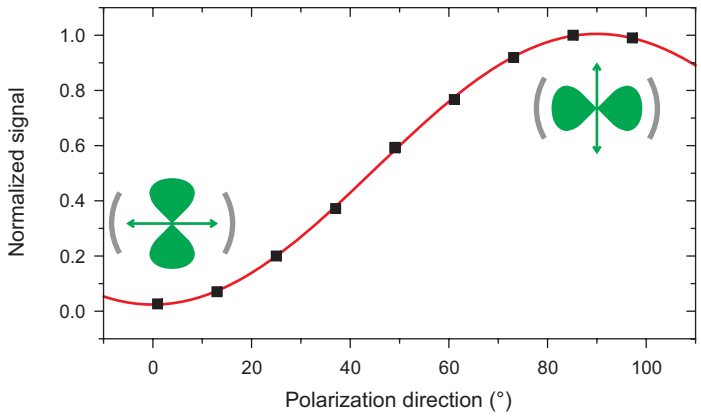

Figure 6.4: Polarization dependence of the Rayleigh-scattered light from any of the three gases used. When the polarization direction of the pump beam is aligned with the cavity axis, no scattering into the cavity occurs. In the opposite case, polarization direction perpendicular to the cavity axis, the maximal amount of light is scattered into the cavity. The solid curve is a fit of a $\sin^2\theta$ polarization dependence to the data. For light scattering from a classical oscillating dipole, such a $\sin^2\theta$ polarization dependence is expected.

of the pump beam. This $\sin^2\theta$ dependence observed for all gases is the characteristic feature for a scattering process involving an oscillating dipole.

As shown in Fig. 6.5, the line shape is determined by Doppler broadening for low densities. Due to the 90° scattering geometry, a Doppler width $\alpha_{obs} = \sqrt{2}\,\alpha_D$ is observed, with α_D being the standard Doppler width of absorption spectroscopy. By varying the pressure, a linear dependence of the scattered power on the gas density is oberved, thereby ruling out scattering off surfaces as the signal source. Also, the expected linear dependence of the Rayleigh scattered light on the pump beam power over the entire examined range of 0.1–5 W is found. However, when increasing the gas pressure from 100 mbar, where the experiment is typically operated, to values of up to 1 bar, the appearance of substructure on the Doppler-broadened peaks is observed. These sidebands are caused by Brillouin scattering on density waves in the gas [GM80, Pan02].

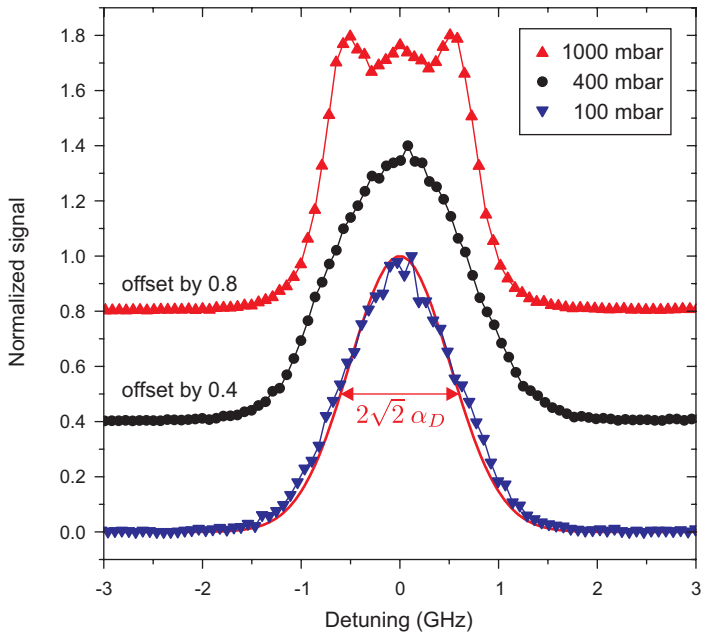

Figure 6.5: Doppler-broadened line profiles for CF_3H. The data of the cavity scans obtained for the different pressures have been individually normalized to the maximal value. In the measurement with lowest pressure, the theoretically predicted Doppler profile is shown in red. At higher pressure, sidebands caused by Brillouin scattering appear.

6.3 Classical wave-interference model of cavity enhancement

To model the experiment, the scattering from a polarizable particle, a classical oscillating dipole, into a single cavity mode is considered. As indicated in Fig. 6.6, the particle is pumped from the side by the electric field E_p. The electric field scattered by the particle into the cavity mode traveling in one direction is expressed as $E_\mathrm{sc} = \alpha E_\mathrm{p}$, with α being a proportionality factor (which equals, except for numerical prefactors, the polarizability). To derive an expression for the intracavity field and finally the power scattered into the cavity mode, all possible contributions to the intracavity light field are taken into account. These contributions modifying the intracavity light field on one roundtrip are light scattering from the pump beam into the cavity mode and losses by transmission of the intracavity field through the mirrors.

6.3.1 The intracavity field

The different contributions to the intracavity light field are schematically shown in Fig. 6.6. The scatterer emits an electromagnetic field into a right and a left-traveling

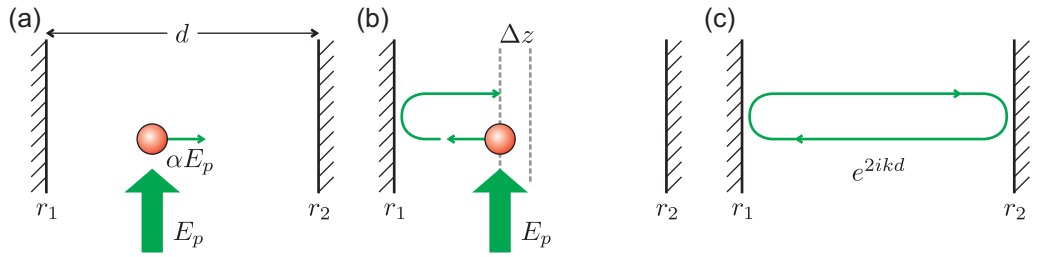

Figure 6.6: Theory sketch. Different contributions to the right-traveling intracavity field at the position of the scattering particle. (a) Field scattered into the right direction. (b) Field scattered to the left, after one reflection at the mirror. (c) Intracavity field after one round trip.

wave, which can interfere. The right-running intracavity field E_c at the position of the scatterer is found by adding up all contributions, leading to

$$E_\mathrm{c} = \alpha E_\mathrm{p} + r_1 e^{ik(d+2\Delta z)} \alpha E_\mathrm{p} + r_1 r_2 e^{2ikd} E_\mathrm{c}, \tag{6.1}$$

where r_i are the mirror's amplitude reflection coefficients ($r_i^2 = R_i$ is the mirror reflectivity). The cavity length is denoted by d, and $k = 2\pi/\lambda$ is the wave number of the light field. The additional phase factor $e^{2ik\Delta z}$ accounts for a translation Δz of the scatterer along the cavity axis. By solving Eq. (6.1) self-consistently, the field scattered into the cavity is found to be given by

$$E_\mathrm{c} = \alpha E_\mathrm{p} \frac{1 + r_1\, e^{ikd}\, e^{2ik\Delta z}}{1 - r_1 r_2\, e^{2ikd}}. \tag{6.2}$$

In the following, a resonant cavity is assumed, $e^{2ikd} = 1$. To calculate the intensity running in the right direction

$$I_\mathrm{c} = \frac{c\epsilon_0}{2} \left| E_\mathrm{c} E_\mathrm{c}^* \right| \tag{6.3}$$

for a randomly-distributed gas, an average over the position of the particles, i.e., $-\lambda/2 \leq \Delta z \leq \lambda/2$, must be taken, resulting in

$$I_\mathrm{c} = \alpha^2 I_\mathrm{p} \frac{1 + r_1^2}{(1 - r_1 r_2)^2}. \tag{6.4}$$

For high mirror reflectivities, $R_i = r_i^2 \approx 1\,(i = 1, 2)$, this can be approximated by

$$I_\mathrm{c} \approx 2\alpha^2 I_\mathrm{p}\, (\mathcal{F}/\pi)^2 \tag{6.5}$$

with the cavity finesse $\mathcal{F} = \pi \sqrt[4]{R_1 R_2}/(1 - \sqrt{R_1 R_2}) \approx \pi/(1 - \sqrt{R_1 R_2})$. In an intuitive picture, $\mathcal{F}/\pi$ is the number of reflections in the resonator. The electric field increases linearly with this number, hence $I_\mathrm{c} \propto (\mathcal{F}/\pi)^2$.

For the following discussion, it is convenient to convert all intensities I into powers P using the area of the cavity mode as a reference. From Eq. (6.5), the power leaving the cavity through the right mirror is found to be given by

$$P_\mathrm{t} = T_2 \times P_\mathrm{c} \approx 4\,T_2/(T_1+T_2)\,\alpha^2 P_\mathrm{p}\,\mathcal{F}/\pi, \tag{6.6}$$

when $r = \sqrt{R} = \sqrt{1-T}$ and the Taylor-series expansion

$$\begin{aligned}\frac{\mathcal{F}}{\pi} &\approx \frac{1}{1-\sqrt{R_1 R_2}} = \frac{1}{1-\sqrt{(1-T_1)(1-T_2)}} \\ &= \frac{1}{1-\sqrt{1-(T_1+T_2)+T_1T_2}} \approx \frac{2}{T_1+T_2}\end{aligned} \tag{6.7}$$

are inserted. For the symmetric-cavity case ($T_1 = T_2 = T$), this simplifies to

$$P_\mathrm{t} \approx 2\,\alpha^2 P_\mathrm{p}\,\mathcal{F}/\pi. \tag{6.8}$$

Therefore, the enhancement of the detectable scattered power into one output mode, i.e., leaving the cavity through one of the mirrors, compared to the situation without the cavity, is given by $2\,\mathcal{F}/\pi$. Since half of the light leaks out of the left cavity mirror, the total power scattered into the cavity mode is given by

$$P_\mathrm{cav} = 2\,P_\mathrm{t} \approx 4\,\alpha^2 P_\mathrm{p}\,\mathcal{F}/\pi. \tag{6.9}$$

For particles maximally coupled to the cavity, i.e., no averaging over particle position, an additional factor 2 comes in

$$P_\mathrm{cav} = 8\,\alpha^2 P_\mathrm{p}\,\mathcal{F}/\pi. \tag{6.10}$$

This has to be compared to the total power scattered into free space into the mode defined by the cavity but without the cavity enhancement, which is

$$P_\mathrm{fs}^{\Omega_\mathrm{cav}} = 2\,\alpha^2 P_\mathrm{p}. \tag{6.11}$$

Therefore, the cavity enhances the power scattered into the same mode of the electromagnetic field by a factor $4\,\mathcal{F}/\pi$ as compared to the free-space situation.

6.3.2 Comparison to free-space scattering: The Purcell factor

So far, only a single mode of the electromagnetic field was considered. Thereby, the power scattered into the cavity mode was compared to the power scattered into the same mode in the free-space situation. Such a scenario is often faced in the experiment, where one is only interested in the light scattered into a single mode which can, e.g., be efficiently coupled into a single-mode optical fiber for detection. It is, however, also interesting to compare the power P_cav scattered into the cavity to the power P_fs scattered into the full 4π solid angle.

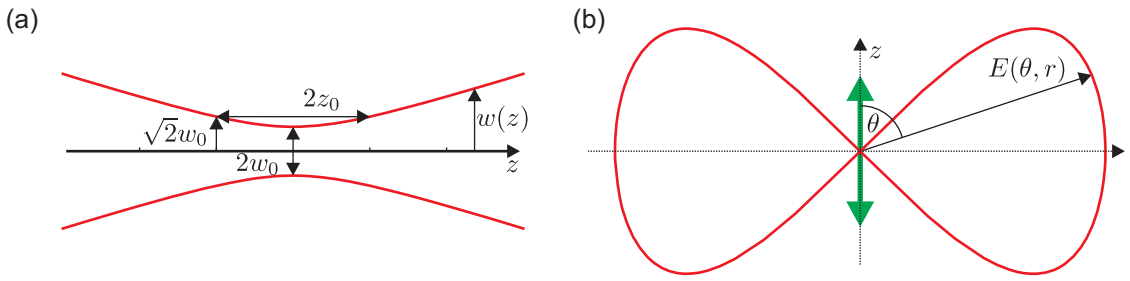

Figure 6.7: (a) Beam width $w(z)$ of the lowest-order transverse Hermite-Gaussian cavity mode TEM_{00} along its propagation direction z. w_0 is the beam waist, and $z_0 = \pi w_0^2/\lambda$ is the Rayleigh length. (b) Emission pattern of the classical oscillating dipole oriented along the z-axis.

Overlap between dipole emission pattern and cavity mode

For this, the overlap integral between the intensity-normalized electric fields of the dipole mode and the cavity mode are evaluated. The cavity mode and the dipole emission pattern are schematically shown in Fig. 6.7. The scalar dipole mode $E_{\mathrm{dip}}(\theta, r)$ can be defined in in spherical coordinates as

$$E_{\mathrm{dip}}(\theta, r) = \sqrt{\frac{3}{8\pi}} \frac{1}{r} \sin(\theta), \tag{6.12}$$

where the phase variation $\exp(ikr)$ along the propagation direction $\mathbf{r}$ has been omitted. The dipole mode is normalized to its intensity,

$$\iint E_{\mathrm{dip}}(\theta, r)^2 \, r^2 \sin(\theta) \mathrm{d}\theta \mathrm{d}\varphi = 1. \tag{6.13}$$

In the experiment, the lowest-order transverse Hermite-Gaussian mode TEM_{00} was used. The electric field of the fundamental cavity mode $E_{\mathrm{cav}}(r, z)$ in cylindrical coordinates is given by

$$E_{\mathrm{cav}}(r, z) = \frac{1}{N_{\mathrm{cav}}(z)} \exp\left(-\frac{r^2}{w(z)^2}\right), \tag{6.14}$$

where the phase variation along the propagation direction z has been omitted. $N_{\mathrm{cav}}(z)$ is a normalization constant (see Eq. (6.17)), and $w(z)$ is the beam waist defined as

$$w(z) = w_0 \sqrt{1 + \left(\frac{z}{z_0}\right)^2} = w_0 \sqrt{1 + \frac{\lambda^2}{\pi^2 w_0^4} z^2}. \tag{6.15}$$

The mode is normalized into one direction as

$$\iint E_{\mathrm{cav}}(r, z)^2 \, r \mathrm{d}r \mathrm{d}\varphi = 1, \tag{6.16}$$

which requires

$$N_{\mathrm{cav}}(z) = \frac{\pi w_0^2}{2} + \frac{\lambda^2}{2\pi w_0^2} z^2. \tag{6.17}$$

Now, the overlap integral between the intensity-normalized electric fields of the dipole mode E_{dip}, Eq. (6.12), and the fundamental Hermite-Gaussian cavity mode E_{cav}, Eq. (6.14), are evaluated in the far field at a fixed value z. There, the dipole mode and the cavity mode have phase fronts lying on spheres centered at the position of the scatterer. The overlap in one propagation direction z is given by

$$\eta = \int_A E_{\mathrm{dip}}^* E_{\mathrm{cav}} \Omega. \tag{6.18}$$

Due to the small transverse extent of the cavity mode, the dipole mode E_{dip} is approximated by its value on the z-axis,

$$E_{\mathrm{dip}}(\theta = \pi/2, z) = \sqrt{\frac{3}{8\pi}} \frac{1}{z}. \tag{6.19}$$

This results in

$$\eta = \iint E_{\mathrm{cav}} \sqrt{\frac{3}{8\pi}} \frac{1}{z}\, r \mathrm{d}r \mathrm{d}\phi = \frac{\sqrt{3} w_0}{2z} + \frac{\sqrt{3}\lambda}{2\pi w_0}, \tag{6.20}$$

which in the limit $z \to \infty$ converges to

$$\eta = \frac{\sqrt{3}\lambda}{2\pi w_0}. \tag{6.21}$$

The fraction of the full 4π solid angle covered by the cavity mode Ω_{cav} is given by the ratio between the power scattered into the cavity mode and the total power scattered into the dipole mode. Hence,

$$\Omega_{\mathrm{cav}} = 2\eta^2 = \frac{3\lambda^2}{2\pi^2 w_0^2}, \tag{6.22}$$

where the factor 2 comes into play since in the evaluation of the overlap integral only one direction of the cavity mode was taken into account. Here, the intensities are summed up and not the fields, since there is no interference between the fields scattered into the two directions.

Comparison to free-space scattering

The power scattered into the mode defined by the cavity in the free-space situation, i.e., without the cavity enhancement, is (see section 6.3.1)

$$P_{\mathrm{fs}}^{\Omega_{\mathrm{cav}}} = 2\,\alpha^2 P_{\mathrm{p}}. \tag{6.23}$$

Using the effective solid angle of the cavity mode, the total power scattered into free space is given by

$$P_{\mathrm{fs}} = \frac{1}{\Omega_{\mathrm{cav}}} \times P_{\mathrm{fs}}^{\Omega_{\mathrm{cav}}} = \frac{4\pi^2 w_0^2}{3\lambda^2}\, \alpha^2 P_{\mathrm{p}}. \tag{6.24}$$

Therefore, the ratio between the power P_{cav} scattered into the cavity mode by a particle maximally coupled to the cavity and the total power P_{fs} scattered into free space is found to be

$$\frac{P_{\mathrm{cav}}}{P_{\mathrm{fs}}} = \frac{8\,\alpha^2 P_{\mathrm{p}}\, \mathcal{F}/\pi}{\frac{4\pi^2 w_0^2}{3\lambda^2}\, \alpha^2 P_{\mathrm{p}}} = 6\,\frac{\lambda^2}{\pi^2 w_0^2}\, \mathcal{F}/\pi. \tag{6.25}$$

The Purcell factor

In the literature, processes modified by the presence of a cavity such as enhanced spontaneous-emission rates [Goy83, Hei87] are typically connected to the Purcell factor [Pur46]. The Purcell factor is defined as

$$2C = \frac{3}{4\pi^2}\lambda^3 \frac{Q}{V}, \tag{6.26}$$

with Q the quality factor of the cavity and V the mode volume. For an atomic system, the free-space atomic-polarization decay rate γ is changed to the value $\gamma' = (1 + 2C)\gamma$ by the presence of a cavity being resonant with the atomic transition frequency. For a two mirror Fabry-Perot cavity, the mode volume V is well approximated by

$$V = \pi w_0^2 L/4. \tag{6.27}$$

The Q factor is defined as $Q = \nu/\delta\nu$ with ν the resonance frequency of the cavity and $\delta\nu$ the cavity linewidth. For a Fabry-Perot cavity, this can be related to the cavity finesse $\mathcal{F}$ and the cavity length L via

$$\mathcal{F} = \frac{c}{2L}\frac{1}{\delta\nu} \tag{6.28}$$

and

$$Q = \frac{\nu}{\delta\nu} = \frac{c/\lambda}{\delta\nu}. \tag{6.29}$$

Therefore, the cavity Q factor can be expressed in terms of the cavity finesse $\mathcal{F}$ and cavity length L as

$$Q = \frac{2L}{\lambda}\, \mathcal{F}. \tag{6.30}$$

Putting all of the above together, one finds for the Purcell factor of a standing-wave Fabry-Perot cavity

$$2C = \frac{3}{4\pi^2}\lambda^3 \frac{Q}{V} = \frac{3}{4\pi^2}\lambda^3 \frac{(2L/\lambda)\, \mathcal{F}}{\pi w_0^2 L/4} = 6\frac{\lambda^2}{\pi^2 w_0^2}\, \mathcal{F}/\pi. \tag{6.31}$$

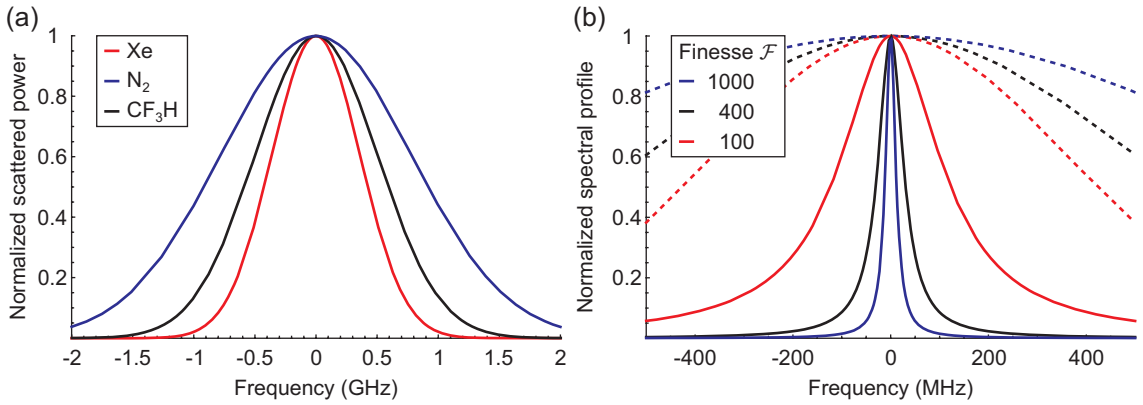

Figure 6.8: Spectral Overlap between the Doppler-broadened scattering profile and the Lorentzian cavity line shape. (a) Doppler profile for the different room-temperature gases used in the experiment. The factor $\sqrt{2}$ due to the 90° scattering geometry is included. (b) Calculated spectral profile of the cavity resonance for the different values of the finesse employed in the experiment. The dashed curves are the same Doppler profiles as shown in (a), which vary only slightly over the frequency range spanned by the cavity linewidth.

This is exactly the same expression as the one obtained using the classical wave-interference model, Eq. (6.25). Therefore, the classical wave-interference model presented here shows that the Purcell factor is indeed fully explained by interference of scattered fields [Kas62, Mil73, Dow93].

6.4 Cavity-finesse dependence of Rayleigh scattering

In section 6.2, the spectral profiles of the light scattered into the cavity were discussed. There, the mode structure of the cavity was clearly visible from the distinct transverse cavity modes in Fig. 6.3. However, this measurement did not yet allow a conclusion whether the cavity indeed enhances the amount of scattered light. Therefore, measurements were performed for different values of the cavity finesse, under otherwise identical conditions.

6.4.1 Influence of the cavity finesse on the spectral profiles

Before comparing the experimental results to the theoretical predictions, the effect of the thermal motion is briefly discussed. The frequency dependence of the power scattered from a polarizable medium into the cavity is given by the convolution of the Lorentzian cavity line shape with the Doppler-broadened profile. Figure 6.8 compares the Doppler profiles of the various thermal gases with the spectral profiles of the cavity for different values of the cavity finesse. For the gases used, the $1/e$ Doppler half-widths α_{D} are 0.50 GHz for CF_3H, 0.78 GHz for N_2, and 0.36 GHz for

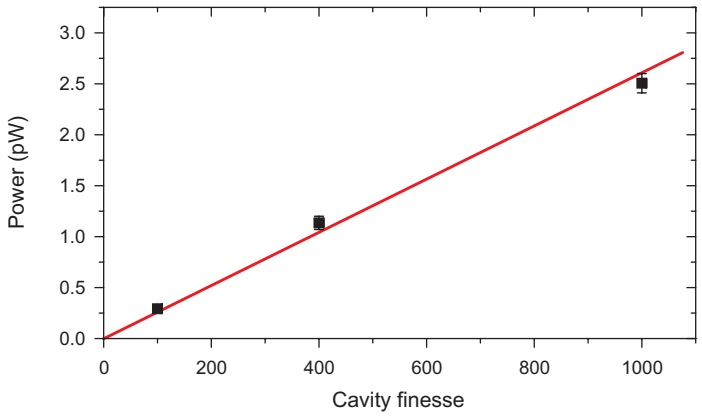

Figure 6.9: Dependence of scattered power on the cavity finesse, measured with Xe at 0.1 bar. The data is corrected for the limited overlap of the cavity mode with the Doppler-broadened spectrum of the Rayleigh-scattered light.

Xe. Hence, the experimentally relevant Doppler half-width $\alpha_{\mathrm{obs}} = \sqrt{2}\alpha_{\mathrm{D}}$ is much larger than the cavity HWHM (Half Width at Half Maximum) κ, which takes a value of ≈ 125 MHz for the lowest-finesse resonator. For a thermal gas, increasing the cavity finesse does not increase the overall power of Rayleigh scattered light into the cavity mode. Although the power scattered by a molecule being resonant with the cavity increases linearly with cavity finesse, the number of resonant molecules decreases linearly with κ (for $\kappa \ll \alpha_{\mathrm{obs}}$). Hence, these two effects cancel. Only for cold scatterers, when the Doppler width becomes smaller than the cavity line width, increasing the cavity finesse pays off in terms of observable signal.

6.4.2 Cavity-finesse dependence of the scattered power

To test the expected dependence of the scattered power on the cavity parameters, the cavity output power was measured for the three available values of the cavity finesse $\mathcal{F}$=(1000, 400, 100). The spectral overlaps of a Doppler-broadened thermal Xe gas with the cavity modes are (4.2, 10.1, 33.4) % for the respectively used cavities. From the measured signals (52, 85, 90) fW, the scattered power from particles at rest was calculated to eliminate the effect of thermal motion, i.e., the Doppler broadening. The result for Xe is shown in Fig. 6.3 (d). As predicted by the classical wave-interference model and the Purcell factor, a linear dependence on the cavity finesse is found. The scattered power also depends on the polarizability of the particles. From the experiment a ratio between scattered powers for Xe, CF_3H, and N_2 of (1: 0.35: 0.1) is determined for fixed cavity finesse. Based on their polarizabilities [Lid90, Mil81] and Doppler broadenings, ratios of (1: 0.36: 0.09) are expected, which is in good agreement with the observations. The good agreement again confirms the validity of the classical oscillating-dipole light-scattering model.

Finally, the enhancement of the scattered power leaving the cavity as compared to the free-space situation is shown. For this measurement, the single-mode fiber was used to select the same mode in the free-space scattering experiment. Under otherwise identical conditions (100 mbar Xe pressure, 1 W pump power), but without the cavity in place, a scattered power of $\approx 1.3\,\mathrm{fW}$ is observed. A factor of two is estimated for the accuracy of this measurement, constrained by mode-matching. This power measured in free-space scattering has to be compared to the value of $\approx 50\,\mathrm{fW}$ measured with a cavity finesse of 1000, an enhancement of 38. To test the classical model for the cavity enhancement, the limited overlap of the Doppler-broadened spectral profile with the cavity mode of 4.2 %, which does not occur in the free-space scattering, and the enhancement by the cavity with a finesse of 1000 are taken into account. Putting these together, a value of $\approx 2.0\,\mathrm{fW}$ is expected for the free-space scattering measurement without the cavity, taking $\approx 50\,\mathrm{fW}$ measured with the cavity as reference. Within the experimental uncertainties, the calculated and measured enhancements are in agreement, showing the process is well described by the classical model.

6.5 Summary

In this chapter it has been shown that the rate of Rayleigh scattering can be enhanced by placing a thermal gas in an optical cavity, similar to the Purcell effect generally associated with enhanced (or inhibited) spontaneous emission. Compared to the free-space situation, the enhancement factor for scattering into the fundamental cavity mode is found to be as high as 38. The results are in good agreement with the model of a classical oscillating dipole coupled to the cavity mode, showing that the origins of the Purcell effect are by no means quantum-mechanical but instead explainable by an interference effect of classical waves.

The experiment shows the potential of an optical cavity to increase weak signals in light-scattering experiments, which should, in principle, be extendable to Raman-type scattering [Mor07]. The large detuning of the laser light from any optical transition allows the method to be applied to different species as demonstrated with the use of Xe, N_2, and CF_3H, independent of their specific internal level structure. This opens a new pathway to optical detection of deeply-bound ultracold molecules, for which the efficient production was reported recently [Sag05, Osp08, Dan08, Dei08b, Lan08, Ni08, Vit08, Ni09, Osp09]. So far, however, detection of these molecules requires either dissociation to unbound atom pairs or ionization. Here, cavity-enhanced Rayleigh scattering might be an attractive in-situ detection technique since it does not rely on closed cycling transitions. Although in the described experiment room-temperature gases at typical densities of $2.5 \times 10^{18}\,\mathrm{cm}^{-3}$ were used, the number of particles contributing to the scattering into the cavity is only $\approx 10^{10}$ for a cavity finesse of 1000. The aforementioned molecule production techniques can typically prepare 10^5 ultracold molecules at

cloud sizes compatible with the cavity-mode diameter in the presented experiment. Since Doppler broadening is absent for light scattered by these trapped ultracold molecules, the cavity finesse can be increased to an experimentally realistic value of 10^5. Furthermore, alkali dimers have a more than $10\times$ larger polarizability α as compared to Xe used as a reference gas in the described measurements (static polarizabilities α, which should give a lower bound for the polarizabilities at optical frequencies: KRb: 502 a.u., Cs_2: 670 a.u., Xe: 27.3 a.u., 1 a.u.=0.148 $Å^3$) [Lid90, Dei08a], and the Rayleigh-scattering cross section σ scales as $\sigma \propto \alpha^2$. All together, ensemble scattering rates into the cavity on the order of 100 kHz can be anticipated for such an ultracold molecular sample. It follows that on average every molecule scatters photons at a total rate on the order of 1 Hz, where the ratio between scattering into the cavity and scattering into free space $P_{\mathrm{cav}}/P_{\mathrm{fs}} \approx 2$ for the given parameters. Therefore, cavity-enhanced Rayleigh scattering might allow for a nearly demolition-free detection with almost no photon-recoil heating. As an extension of the presented setup, the use of degenerate cavities could boost the power scattered into the cavity with the number of incorporated modes [Cha03]. Collective enhancement effects [Dom02], observed for atomic ensembles [Bla03], could finally result in an additional increase of signal.

Chapter 7

Outlook

In the last years, the electrostatic velocity-filtering and guiding technique has been developed in the Rempe group. A key feature of this method to produce continuous beams of cold polar molecules is its applicability to different molecular species. It demands only for a favorable ratio of Stark shift to mass and the presence of low-field-seeking states populated in the source from which the molecules are extracted. The flux of molecules is so high (up to $10^{11}\,\mathrm{s}^{-1}$ at densities of $10^{9}\,\mathrm{cm}^{-3}$ and typical velocities of 50 m/s [Ran03, Jun04b, Som09, vB09]), that they are easily detected by a quadrupole mass spectrometer. The achievable flux is finally limited by the onset of collisions in the vicinity of the nozzle for increasing reservoir pressure. Especially the slowest molecules are thereby expelled from the beam, such that these collisional effects become observable even in the near-effusive regime in which the source is operated [Mot09a].

The selectivity of the guide on the molecular Stark shift is evident from the contribution of molecules in different internal states to the guided beam. Depending on its rotational state a molecule exhibits a unique Stark shift. Therefore, rotational states with large Stark shifts contribute strongly to the guided beam. Conversely, for molecular species with systematically differing Stark-shift behavior different efficiencies for electrostatic velocity filtering are observed. Taking the water isotopologs as an example, a flux of guided molecules is achieved for HDO which is larger by more than order of magnitude as compared to that of H_2O and D_2O. Responsible for this behavior are states with mainly linear Stark shifts in HDO and the quadratic Stark shifts of H_2O and D_2O. As a consequence, a specific dependence of the signal of guided molecules on the applied electrode voltage is observed as well [Mot09b]. The internal-state distribution of guided molecules is even more directly accessible by depletion spectroscopy. Using ultraviolet laser excitation, guided formaldehyde molecules are optically pumped to a predissociating electronic state. The laser-frequency-dependent molecule loss reveals the contribution of individual rotational states to the guided beam. These contributions depend on the molecular states' Stark shift and its population in the thermal source as described by the model of velocity filtering [Mot07].

All measurements presented in this thesis share one feature: The guided molecules are detected by a quadrupole mass spectrometer. This is a destructive detection process, which is common to most other methods in the field of cold molecules. For example, molecules which are produced using magnetic Feshbach resonances are dissociated to atom pairs before being imaged with resonant laser light. For many applications it is desirable to have a non-destructive detection method at hand. Cavity-enhanced Rayleigh scattering, which has been observed for room-temperature gases, might permit such in-situ, non-destructive detection for dense samples of trapped ultracold molecules [Mot09c].

In the following sections, some possible applications and future extensions of electrostatic velocity filtering and guiding are discussed. The extension of depletion spectroscopy beyond internal-state diagnostics and the study of cold collisions are presented in section 7.1 as possible applications of the guiding technique. Ongoing developments in the Rempe group are discussed in section 7.2. On the one hand side, they advertise the use of electric guides as a very general source for cold beams of polar molecules. Meanwhile, the technique is being copied and being used in a number of laboratories around the world (guiding with electrostatic fields: [Bic05, Tsu07, Hel08, Hum08a, Pie08, Wil08a, Wil08b, Bel09a, Mom09, Mud09, Pat09], guiding with alternating electric fields: [Fil08, Küp09, Wal09]). On the other hand side, they show the necessity for the detailed understanding of the velocity-filtering process which was gained in this thesis. Especially individual internal molecular states become even more important for the new cooling and trapping schemes under development. This points out the significance of the acquired proficiency about their influence on velocity filtering and guiding.

7.1 Extensions and applications of electrostatic velocity filtering and guiding

7.1.1 Spectroscopy of cold molecules

So far, depletion spectroscopy has been performed with guided formaldehyde molecules in the near-ultraviolet spectral range for internal-state diagnostics. The molecules are optically pumped to an excited state which predissociates, such that a decrease in the flux of guided molecules proportional to the population of the addressed internal state is observed. Pumping to a dissociating state is, however, not a necessary condition for application of this method. Instead, it is sufficient to transfer the molecules to some internal state which is not guided anymore. This may be either a high-field-seeking state or a low-field-seeking state with a significantly smaller Stark shift as compared to the initial state. In this situation a depletion signal, dependent on the population of the addressed internal molecular state, will be observable as well. Therefore, the depletion-spectroscopy technique could be transferred to other frequency ranges to address different species. Many molecules which

have been successfully velocity filtered and guided [Som09] have vibrational transitions in the mid-infrared range around 3–5 μm [Zep09]. In this wavelength range, optical parametrical oscillators (OPOs) are available as tunable narrow-linewidth continuous-wave (cw) or pulsed lasers.

Furthermore, depletion spectroscopy is not only a tool for internal-state diagnostics. It can be used as well to depopulate unwanted states, thereby increasing the purity of the guided beam. Spectroscopy in a cold and guided beam of polar molecules offers the advantage of long interaction times, making it attractive for the study of weak transitions. In the presented experiment the observed lineshape and linewidth of the transitions was caused by the magnitude of the inhomogeneous guiding electric field. To circumvent this, spectroscopy could be performed with molecules occupying a trap volume, in which homogeneous electric fields ar applied. This would result in smaller linewidths and as an additional benefit in even longer interaction times with the laser light. Such a trap can be implemented with microstructured electrode arrays in a way compatible with the electrostatic guiding system [Zep09].

7.1.2 Collision experiments with cold molecules

Due to their high flux and continuous character, cold guided beams produced by electrostatic velocity filtering promise to be an excellent starting point for the investigation of cold collisions and cold chemistry. The applicability of the electric guide as a cold molecule source for such collision studies has already been demonstrated in an experiment targeting laser-cooled trapped atomic Ca^+ ions with cold guided CH_3F molecules [Wil08a, Wil08b, Bel09a]. Conceivable experiments include collisions between the cold guided beam and ultracold atoms in a magneto optical trap (MOT), which might even be extendable to sympathetic cooling of polar molecules. In a recent paper, P. S. Żuchowski and J. M. Hutson presented calculations of cross sections for low-energetic collisions of NH_3 and ND_3 with ultracold Rb atoms [Żuc09]. These calculations focus on NH_3 (ND_3) molecules in the upper component of the inversion doublet of the $|J = 1, K = 1\rangle$ state ($11u$). This low-field-seeking state is used for Stark deceleration and also preferentially populated in cold guided beams produced by electrostatic velocity filtering in combination with buffer-gas cooling. According to their results, the cross section for elastic collisions between NH_3 or ND_3 and Rb is on the order of 1000 Å^2 over a wide energy range (1–100 cm^{-1}), while the cross section for inelastic collisions is predicted to be on the order of 100 Å^2. For lower collision energies (but not too small, $\geq$100 μK) the elastic cross section for ND_3-Rb collisions is still larger than the inelastic cross section for transitions to the high-field-seeking lower component of the inversion doublet of the $|J = 1, K = 1\rangle$ state ($11l$), however, not by more than a factor of ten. This rather small ratio makes the realization of sympathetic cooling to ultracold temperatures through the combination of electrostatically trapped ND_3 molecules in a low-field-seeking state with Rb atoms not too favorable. As a possible way out, P. S. Żuchowski and J. M. Hutson

suggest that ND_3 molecules in a high-field-seeking state trapped by AC electric fields could show much more favorable collision properties with magnetically trapped Rb atoms, which might permit sympathetic cooling.

Combining the calculated cross section for ND_3-Rb collisions of $\sigma{=}10^{-13}\,\mathrm{cm}^2$ [Żuc09] with the flux of $\Phi{=}10^{11}$ molecules/s produced by the electric guide [Som09, vB09], some estimates can be made for an imaginable collision experiment between the two species. We assume a cloud of laser-cooled atoms is held in a trap for neutral atoms [Met99]. To ensure good overlap between the atoms and the molecular beam, the trapped atom cloud can be positioned inside the electric guide. Since the molecules are hot compared to the depth of the trap holding the atoms, an atom undergoing a collision will be expelled from this trap. The experimentally accessible signature for collisions is the relative loss rate of atoms, R/N, with R being the scattering rate and N the atom number. If the size of the atom cloud is small compared to the diameter of the molecular beam, this relative atom loss rate can be estimated by

$$R/N = \Phi \times \frac{\sigma}{d_\mathrm{m}^2}, \tag{7.1}$$

with d_m being the diameter of the molecular beam. This formula is motivated as follows: $p_\mathrm{sc} = \sigma/d_\mathrm{m}^2$ is the probability for a single molecule in the guided beam to undergo a collision with a single atom. The rate, with which an atom is kicked out of the trap by a collision with any of the guided molecules, is therefore given by $\Phi \times p_\mathrm{sc}$. Putting in the numbers given above together with the size of the molecular beam of $d_\mathrm{m} \approx 0.1\,\mathrm{cm}$ results in a relative loss rate of atoms of $R/N \approx 1\,\mathrm{s}^{-1}$. This should be observable in an experiment, considering typical lifetimes on the order of 10 s for trapped neutral atoms. As an alternative, one could place the atom cloud behind the exit of the guide to avoid influences of the electric guiding fields. Note that the density of molecules would be reduced in such an experiment, since the molecular beam spreads out when leaving the guiding structure [Jun04b, Som09]. Nevertheless, the flux of molecules through the atom cloud should still be high enough to cause a measurable loss of atoms.

7.2 Ongoing developments in the Rempe group

In this section ongoing developments in the cold molecules group are presented. The combination of electrostatic velocity filtering with buffer-gas cooling, which allows to produce high-flux beams of internally-cold polar molecules, is discussed in section 7.2.1. The availability of such a high-purity beam of molecules allows, e.g., the investigation of internal-state-dependent cross sections in cold collision experiments. To bridge the gap from the cold to the ultracold regime, a cooling scheme based on infrared transitions in suitably tailored trapping electric fields is under development. The main ideas of this opto-electrical cooling scheme are presented in section 7.2.2.

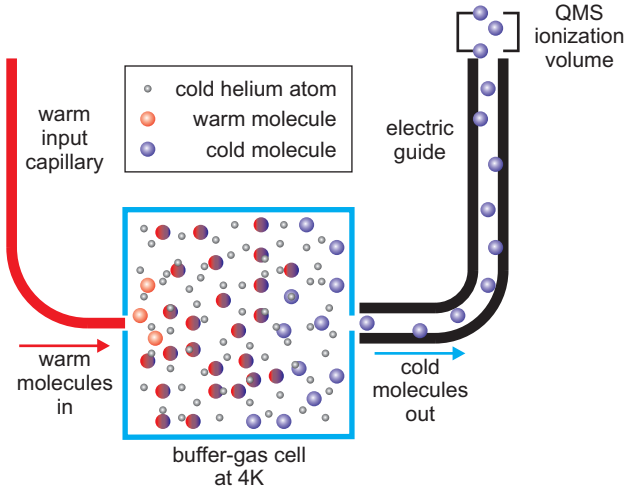

Figure 7.1: Schematic representation of the setup combining cryogenic buffer-gas cooling and electrostatic extraction. Molecules are injected into the cold buffer gas through a warm input capillary. In the buffer-gas cell their translational and internal degrees of freedom are cooled by collisions with the cold helium atoms. Slow molecules, which leave the cell through the exit hole and which are in a low-field-seeking internal state, are collected by the electrostatic guide. These molecules are then transported out of the cold environment, where they are detected by the QMS.

7.2.1 Electrostatic extraction of molecules from a cryogenic buffer-gas source

In section 5.3 it was shown that the internal-state distribution of guided formaldehyde molecules is purified by reducing the source temperature. Nonetheless, the maximally achievable temperature reduction with the liquid-nitrogen-cooled nozzle described in section 2.2 is limited to 150 K. Below this temperature, the vapor pressure of the formaldehyde gas in the nozzle becomes lower than the typical operation pressure. This causes condensation of the molecules on the walls of the effusive source and a strong reduction in the flux of molecules. To circumvent this problem the molecules must be cooled by other means. This can be achieved by collisions with a cold buffer gas, thereby avoiding collisions with a cold wall [Wei98]. In such experiments helium is typically used as a buffer gas, since it is the only gas to have a sufficiently high vapor pressure at temperatures of a few Kelvin.

In the last few years a setup combining cryogenic buffer-gas cooling and electrostatic velocity filtering has been developed in the Rempe group, thereby merging the advantages of the two approaches [Som09, vB09]. The principle is schematically shown in Fig. 7.1. Warm molecules are injected into a cryogenic ($T \geq 4\,K$) helium buffer gas. Both the translational and internal degrees of freedom of the molecules are cooled by collisions with the cold helium atoms. Slow molecules, which leave the cell through a small exit hole and which are in a low-field-seeking internal state,

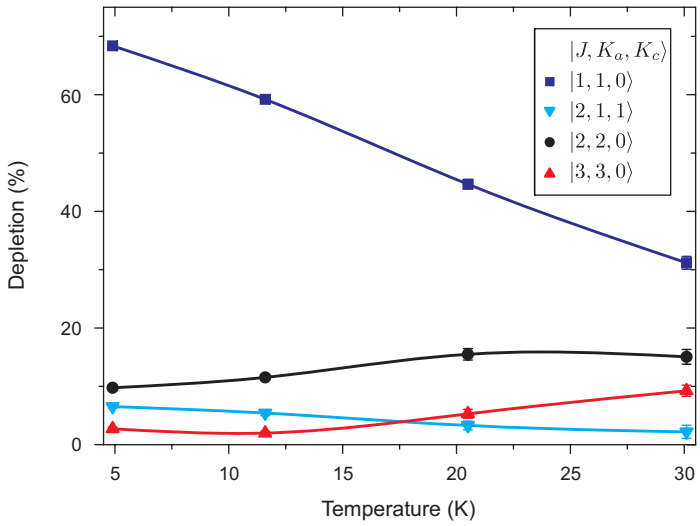

Figure 7.2: Temperature dependence of the depletion signal for guided formaldehyde (H_2CO) molecules. This laser-induced depletion in the signal of guided molecules is proportional to the population in the addressed rotational state. For lower cell temperatures the population in the lower-energetic rotational states increases and the purity of the guided beam is improved. For comparison, at a source temperature of 300 K the state $|1,1,0\rangle$ contributes 2 % to the guided beam. This value increases to 4 % at a temperature of 150 K, the lowest operable temperature using the liquid-nitrogen-cooled source described in chapter 2. By cooling the reservoir to 4 K and utilizing the buffer-gas-cooling technique, the contribution of this state is enhanced to 80 % [Som09, vB09]

are collected by the electrostatic guide and transported to an UHV chamber for detection and further experiments.

The depletion-spectroscopy technique developed within this thesis is employed to quantitatively study internal cooling of the molecules in the buffer-gas cell. Initially, the performance of the setup, which combines buffer-gas cooling and electrostatic guiding, has been optimized with deuterated ammonia (ND_3) molecules. Thereupon, depletion spectroscopy of guided formaldehyde (H_2CO) molecules, which had been cooled in the buffer-gas cell prior to injection into the electric guide, was performed. In this experiment direct evidence for cooling of the internal degrees of freedom is obtained as shown in Fig. 7.2. When the temperature of the buffer-gas cell is reduced, more and more population accumulates in the lowest-energetic low-field-seeking rotational state with a reasonably large Stark shift $|J = 1, K_a = 1, K_c = 0\rangle$. Hence, the purity of the guided beam is significantly improved by the low temperature of the buffer-gas cell. For comparison, at a source temperature of 300 K the state $|1,1,0\rangle$ contributes 2 % to the guided beam, and at a temperature of 150 K it contributes 4 %. By cooling the reservoir, from which the molecules are extracted, to 4 K and utilizing the buffer-gas-cooling technique, the contribution of this state can be enhanced to 80 % [Som09, vB09]. This demonstrates that by complementing

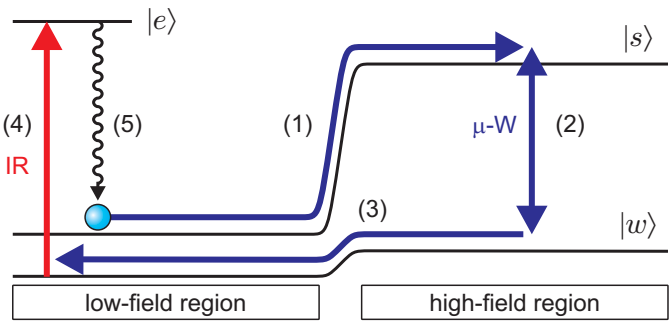

Figure 7.3: Schematic representation of the opto-electrical cooling process. Indicated are the potential energy curves for the lfs molecular states $|s\rangle$ and $|w\rangle$ in the region of low (left) and high electric-field strength (right). (1) Molecules in the strong low-field-seeking state $|s\rangle$ move from the low-field to the high-field region, loosing the amount of kinetic energy corresponding to the difference in Stark energy. (2) There, they are coupled to the weak low-field-seeking state $|w\rangle$ by a microwave field (μ-W), which removes potential energy. (3) The molecules in state $|w\rangle$ move back to the low-field region, gaining less kinetic energy than they lost during (1). (4) To close the cycle, the molecules are optically pumped by an infrared light field (IR) to a vibrationally excited state $|e\rangle$, (5) from which they can spontaneously decay back to the initial state $|s\rangle$.

the electrostatic velocity-filtering setup with such a cold molecule source based on cryogenic buffer-gas cooling, high-flux, state-selected, cold guided beams of polar molecules are produced. Further experiments utilizing these cold beams, the technical details of the setup, its optimization with respect to the relevant quantities of the guided beam, and its everyday operation will be described in the doctoral thesis of Christian Sommer.

7.2.2 Opto-electrical cooling of polar molecules

To cool the molecules produced by the electrostatic velocity-filtering and guiding technique to even lower temperatures, a new trapping and cooling scheme is under development in the Rempe group [Zep09]. Its principle is schematically shown in Fig. 7.3. Cold polar molecules from the electric guide are loaded into an electrostatic trap. There, the molecules are enclosed by high electric fields provided by a ring electrode and two opposing microstructured plate electrodes. This geometry results in a trapping potential for low-field-seeking states.

In the trap volume, two regions of homogeneous, but different magnitude, electric fields are created, between which the molecules can freely move. When a molecule moves from the low-field region to the high-field region, it looses the amount of kinetic energy corresponding to the difference in Stark energy. Hence, this energy difference can be as high as 1 K. Since the molecule can, of course, move back again from the high-field to the low-field region, no cooling is achieved.

To provide cooling, a dissipative process must be added to the scheme. This is accomplished by considering spontaneous vibrational decay in a three-level system as shown in Fig. 7.3. In the high-field region, the strong $|s\rangle$ and the weak $|w\rangle$ low-field-seeking states are coupled. For polar molecules, the states $|s\rangle$ and $|w\rangle$ represent different rotational energy levels. In this case, the coupling is provided by a microwave field (μ-W). The molecule in state $|w\rangle$ can move from the high-field region to the low-field region, thereby gaining less kinetic energy then it lost when climbing the potential-energy hill in state $|s\rangle$. In the low-field region the molecule in state $|w\rangle$ is then optically pumped to an excited state $|e\rangle$. The following spontaneous decay to the initial state $|s\rangle$ renders the whole process unidirectional, hence permitting a net cooling of the molecules in the trap.

Note that the requirements for this spontaneous decay process in opto-electrical cooling are different from those in conventional laser cooling. Laser cooling relies on iterative small momentum transfer by scattering photons on a closed cycling transition, therefore demanding for a fast decay rate in the MHz range as found for electronic dipole transitions [Met99]. In contrast, opto-electrical cooling benefits from the large amount of energy that is removed per scattered photon. This allows to reconsider the use of vibrational transitions, which have been neglected for laser cooling due to glacial decay rates on the order of 100 Hz. Since vibrational transitions exhibit very favorable selection rules for symmetric-top molecules, their use is envisioned for the implementation of the cooling scheme. Simulations of the cooling process show the potential to reach a temperature of 1 mK after 10 s, when starting with a molecular ensemble at a temperature of 0.4 K. Details of the opto-electrical cooling scheme as well as experimental efforts to realize this idea will be discussed in the doctoral thesis of Martin Zeppenfeld.

Appendix A

Guiding-efficiency reconstruction for the different water isotopologs

The purpose of this appendix is to explain how the guiding efficiencies of the different water isotopologs are extracted from the QMS signal. Complications arise since pure measurements are only possible with H_2O and D_2O. For guiding experiments with HDO a mixture of liquid H_2O and D_2O is prepared in a container. These react to form HDO,

$$H_2O + D_2O \rightleftharpoons 2\,HDO. \tag{A.1}$$

The equilibrium concentrations in this hydrogen-exchange reaction depend on the initial volume ratio of H_2O and D_2O. Therefore, the concentrations of the three isotopologs in this liquid depend on the chosen volume ratio between H_2O and D_2O. The constituents of the gas phase above this liquid, whose concentrations reflect the ones in the liquid phase, are brought to the nozzle through a flow valve, as described in section 2.2.

The measurements have all been performed at a constant reservoir pressure of 0.10 mbar with the nozzle assembly at room temperature. To obtain signals of all three water isotopologs, several mixtures with different volume ratios of H_2O and D_2O have been prepared. These ratios and the experimentally determined concentrations in the equilibrium of the hydrogen-exchange reaction, Eq. (A.1), are listed in Tbl. A.1. To reconstruct the fluxes of guided molecules for the individual isotopologs, two main questions must be answered. What is actually injected into the guide, and what detector response is obtained for one guided H_2O, D_2O, or HDO molecule respectively.

A.1 Concentrations of water isotopologs injected into the quadrupole guide

To monitor the gas contents injected through the ceramic nozzle, a residual-gas analyzer (RGA) is placed in the vacuum chamber containing the nozzle and the

Meas. Nr.	Prepared Mixture		Measured Contribution (%)		
	D_2O	H_2O	D_2O	HDO	H_2O
1	0	1	0	0	100
2	1	0	93	6	1
3	1	1	22	47	31
4	4	1	3	27	70

Table A.1: Volume ratios of the different liquid water isotopologs which were mixed in the test tube, and the resulting contributions of the isotopologs in the gas effusing out of the nozzle. In measurement 2, where only D_2O was put in the container, the contributions of HDO and H_2O are due to contaminations of the gas lines with H_2O from previous measurements.

first bend of the quadrupole guide. The RGA records the ion currents of all relevant masses during the measurements. Because the molecules can fragment during electron-impact ionization the ion currents measured at mass 18 amu (amu: atomic mass unit, $1\,\text{amu} = 1.66 \times 10^{-27}\,\text{kg}$), 19 amu, and 20 amu do not directly reflect the concentrations of H_2O, HDO, and D_2O, respectively. The following fragments are detected in the RGA:

$$\text{H}_2\text{O} \rightarrow \begin{cases} \text{H}_2\text{O}^+ & 18\,\text{amu} \\ \text{OH}^+ & 17\,\text{amu} \\ \text{O}^+ & 16\,\text{amu} \end{cases} \tag{A.2a}$$

$$\text{HDO} \rightarrow \begin{cases} \text{HDO}^+ & 19\,\text{amu} \\ \text{OD}^+ & 18\,\text{amu} \\ \text{OH}^+ & 17\,\text{amu} \\ \text{O}^+ & 16\,\text{amu} \end{cases} \tag{A.2b}$$

$$\text{D}_2\text{O} \rightarrow \begin{cases} \text{D}_2\text{O}^+ & 20\,\text{amu} \\ \text{OD}^+ & 18\,\text{amu} \\ \text{O}^+ & 16\,\text{amu} \end{cases} \tag{A.2c}$$

For all these molecules, also hydrogen (H_2^+, H^+) or deuterium ions (D_2^+, D^+) are produced. However, due to the larger contribution of background gas at these masses they are not used for data acquisition. As can be seen from Eq. (A.2), several water isotopologs can contribute to the RGA signal except for 19 amu and 20 amu. Therefore, some corrections are necessary to reconstruct the concentrations of the individual water isotopologs from this integral RGA signal.

In a first measurement, pure liquid H_2O was used. From the measured ion currents a fragmentation ratio of

$$\text{H}_2\text{O} \rightarrow \begin{cases} 18\,\text{amu} & 80\,\% \\ 17\,\text{amu} & 19\,\% \\ 16\,\text{amu} & 1\,\% \end{cases} \tag{A.3}$$

is determined. In a second measurement, pure liquid D_2O was put in the container and the vapor was injected through the nozzle. Nonetheless, also contributions at mass 19 amu and 17 amu are detected with the RGA. These unwanted contaminations can be attributed to residual H_2O from the previous measurements sticking to the walls of the gas lines. The H_2O molecules can then form HDO by hydrogen-exchange reactions with D_2O. Therefore it is not possible to extract a fragmentation ratio for D_2O from unperturbed data. Subtracting the contribution of HDO by scaling the data at mass 19 amu with a hypothetical fragment distribution (see Eq. (A.5)), the data suggest a similar fragmentation ratio of D_2O as for H_2O,

$$\mathrm{D_2O} \rightarrow \begin{cases} 20\,\mathrm{amu} & 80\,\% \\ 18\,\mathrm{amu} & 19\,\% \\ 16\,\mathrm{amu} & 1\,\% \end{cases}. \tag{A.4}$$

Since the fragmentation ratio of HDO can not be determined uniquely from the residual-gas-analyzer signal due to the contributions of D_2O at mass 18 and H_2O at mass 16, based on the measurements with H_2O and D_2O the fragmentation ratio

$$\mathrm{HDO} \rightarrow \begin{cases} 19\,\mathrm{amu} & 80\,\% \\ 18\,\mathrm{amu} & 9.5\,\% \\ 17\,\mathrm{amu} & 9.5\,\% \\ 16\,\mathrm{amu} & 1\,\% \end{cases} \tag{A.5}$$

is assumed.

For the studies of the velocity-filtering and guiding properties of the water isotopologs, mixtures with different volume ratios of H_2O and D_2O have been used. These ratios and the resulting contributions of D_2O, HDO, and H_2O to the gas are listed in Tbl. A.1. For measurements with the mixtures of H_2O and D_2O prepared in the container, the following procedure has been used to determine the relative contents of the gas injected into the guide.

- The reservoir pressure for all the measurements is kept fixed at 0.1 mbar.
- From the ion current measured at 20 amu, I_{20}, the total ion current of D_2O, $I_{\mathrm{D_2O}}$, can be directly determined using the fragmentation probability $p_{20}^{\mathrm{D_2O}}$ of D_2O into mass 20 amu, Eq. (A.3), as

  $$I_{\mathrm{D_2O}} = 1/p_{20}^{\mathrm{D_2O}} \times I_{20}. \tag{A.6}$$

  Similarly, the measurement at 19 amu, I_{19}, yields the total ion current

  $$I_{\mathrm{HDO}} = 1/p_{19}^{\mathrm{HDO}} \times I_{19} \tag{A.7}$$

  of HDO.

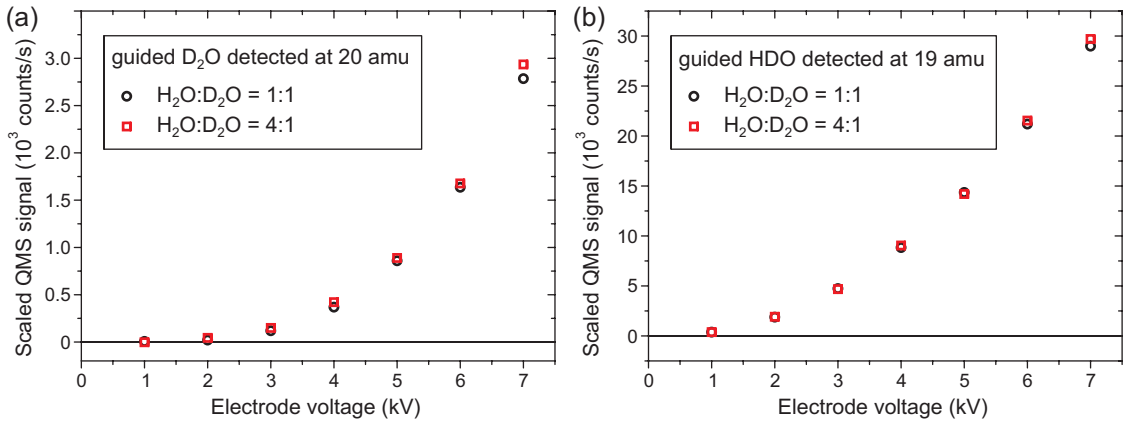

Figure A.1: Electrode-voltage dependence of the signal of guided D_2O and HDO molecules. Different volume ratios of H_2O and D_2O have been put in the container. The measurement with the $H_2O : D_2O = 1 : 1$ mixture is taken as a reference. The data measured with the $H_2O : D_2O = 4 : 1$ mixture are individually scaled with the contributions of D_2O and HDO (see Tbl. A.1) determined with the RGA in the source vacuum chamber.

- The total ion current of H_2O can be determined from the measurement at 18 amu using the previously determined values for the total ion currents of D_2O and HDO. Considering the different possible contributions at 18 amu, one finds

$$I_{18} = p_{18}^{D_2O} \times I_{D_2O} + p_{18}^{HDO} \times I_{HDO} + p_{18}^{H_2O} \times I_{H_2O}, \tag{A.8}$$

  ans therefore arrives at

$$\begin{aligned} I_{H_2O} &= 1/p_{18}^{H_2O} \left[I_{18} - \left(p_{18}^{D_2O} \times I_{D_2O} + p_{18}^{HDO} \times I_{HDO} \right) \right] \\ &= 1/p_{18}^{H_2O} \left[I_{18} - \left(p_{18}^{D_2O}/p_{20}^{D_2O} \times I_{20} + p_{18}^{HDO}/p_{19}^{HDO} \times I_{19} \right) \right]. \end{aligned} \tag{A.9}$$

- As a consistency check, the ion currents at 17 amu and 16 amu can be used.

To test the dependence of electrostatic velocity filtering and guiding on the amount of the different isotopologs injected through the nozzle, the QMS signals of guided HDO and D_2O molecules detected at mass 19 amu and 20 amu, respectively, are considered. For these measurements, H_2O and D_2O have been mixed in the sourc with two different ratios. The QMS signals measured with the $H_2O : D_2O = 1 : 1$ mixture serves as a reference. The observed signals of guided molecules using the $H_2O : D_2O = 4 : 1$ mixture are then scaled with contribution of HDO and D_2O determined with the RGA in the source vacuum chamber, which reflect their relative fraction to the gas injected in the guide. As can be seen from Fig. A.1, the QMS signals of guided HDO and D_2O can be scaled with the ion current. The remaining difference of 5–10 % might be caused by changes in the background gas or by nonlinearities of the RGA and give an estimate for the accuracy of the determination of the gas contents.

A.2 Detection of cold guided water isotopologs

After having discussed the determination of the gas contents injected into the guide, the second point is addressed, namely the detector response to the guided molecules. For these measurements, one assumption is made: All the water isotopologs have the same total ionization probability, which seems reasonable considering the similarity of the molecules. For these measurements the masses 16–20 amu are considered as for the determination of the gas contents injected into the guide

Figure A.2 shows the distribution of masses, at which fragments of guided water molecules are detected. In this figure, measurements with various concentrations of the water isotopologs injected into the guide are combined. These allow a reconstruction of the distributions of the fragments for the individual water isotopologs.

- From the first measurement, Fig. A.2 (a), where only H_2O was injected into the guide, the fragment distribution of H_2O

$$H_2O \rightarrow \begin{cases} 18\,\text{amu} & 63\,\% \\ 17\,\text{amu} & 19\,\% \\ 16\,\text{amu} & 18\,\% \end{cases} \tag{A.10}$$

  is directly visible.

- The measurement with mainly D_2O injected into the guide, Fig. A.2 (b), does not allow to directly reconstruct the fragment distribution of D_2O. Although the contribution of HDO to the gas injected into the guide through the nozzle is only 6 %, the QMS signal at 19 amu, where only HDO contributes, gives nearly the same countrate as the signal at 20 amu, which is solely caused by guided D_2O molecules. The reason for this strong HDO contribution is its higher guiding efficiency due to its larger and linear Stark shifts.

- From the data shown in Fig. A.2 (c), where HDO was injected with the largest contribution of 47 % into the guide, the fragmentation ratio of HDO is extracted. Because the count rate at 20 amu is much smaller than the count rate at 19 amu, the contribution of D_2O is neglected for the analysis. Also the influence of H_2O is neglected, since it contributes with a fraction similar to that of D_2O to the gas injected into the guide and is guided with an efficiency comparable to that of D_2O. The distribution of masses in this measurement is therefore used directly as a fragmentation ratio for HDO,

$$\text{HDO} \rightarrow \begin{cases} 19\,\text{amu} & 74\,\% \\ 18\,\text{amu} & 16\,\% \\ 17\,\text{amu} & 8\,\% \\ 16\,\text{amu} & 2\,\% \end{cases}. \tag{A.11}$$

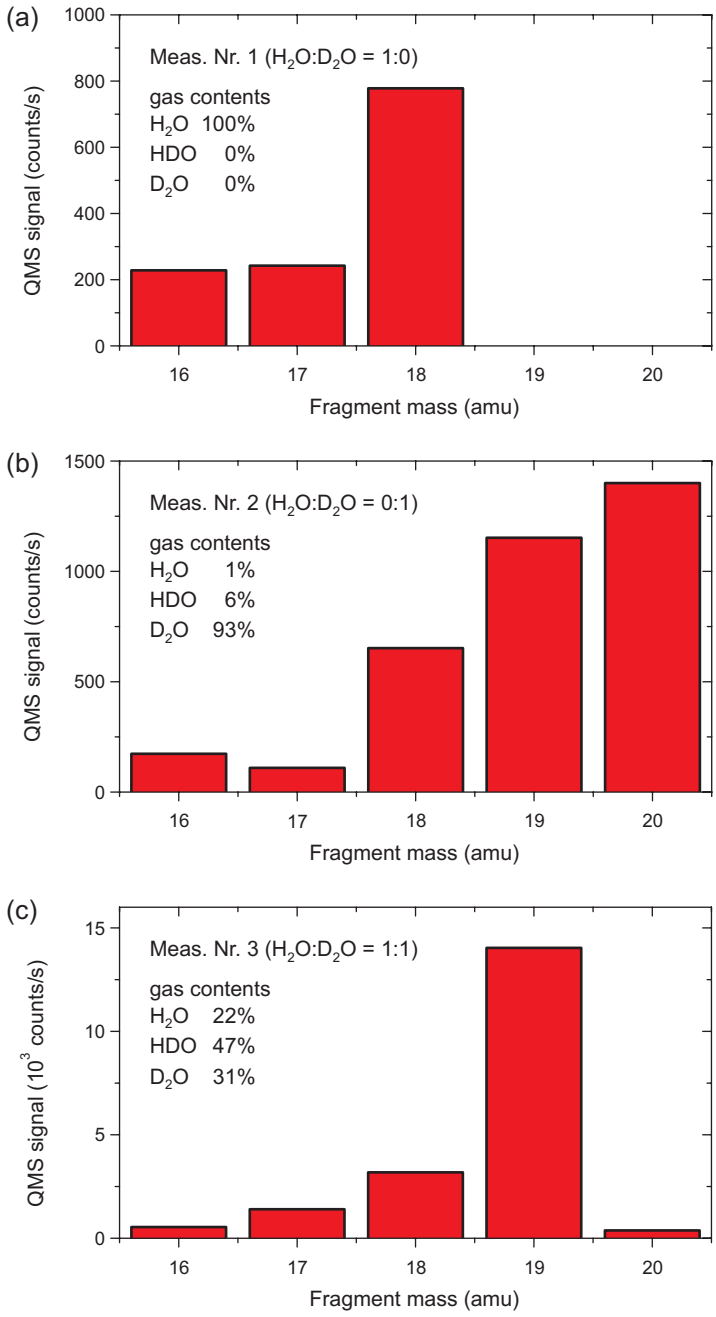

Figure A.2: Distribution of masses, at which fragments of guided H_2O, D_2O, and HDO molecules are detected at an electrode voltage of $\pm 5\,\mathrm{kV}$. A constant reservoir pressure of 0.1 mbar has been used, but the gas contents have been varied as shown in Tbl. A.1. From these measurements, the fragmentation ratios for the various isotopologs are reconstructed.

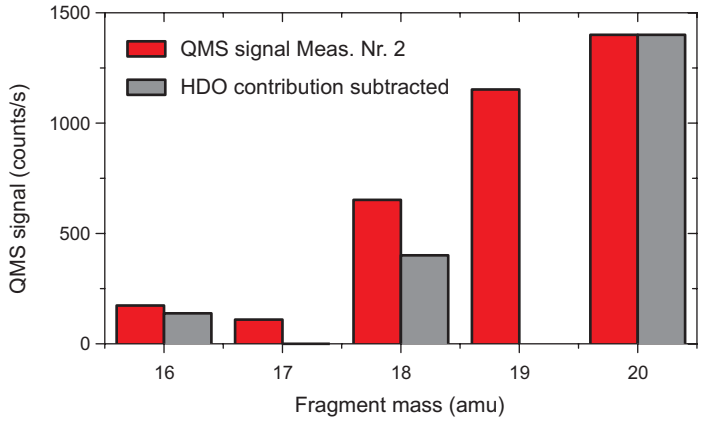

Figure A.3: Determination of the fragmentation ratio of guided D_2O molecules. The same data are shown as in Fig. A.2 (b). Using the fragmentation ratio of HDO determined in advance, the contribution of guided HDO molecules to the signal at masses 16–19 amu is subtracted.

- To extract the fragment distribution of guided D_2O molecules the data of the measurement with mainly D_2O, Fig. A.2 (b), are revisited. In this measurement, the distribution of masses shows fragments of HDO and D_2O. Since H_2O contributed only 1% to the gas injected into the guide, its influence is neglected here. Using the extracted fragmentation ratio of HDO, the contribution of guided HDO molecules is subtracted from the distribution. The result of this correction is shown in Fig. A.3 and yields a fragment distribution of

$$\mathrm{D_2O} \rightarrow \begin{cases} 20\,\mathrm{amu} & 72\,\% \\ 18\,\mathrm{amu} & 21\,\% \\ 16\,\mathrm{amu} & 7\,\% \end{cases} \tag{A.12}$$

  for D_2O. Note that after the correction the residual signal at 17 amu is consistent with zero. Because only HDO could fragment into this mass, this gives a hint for the reliability of the method.

Bibliography

[Abr95] E. R. I. Abraham, N. W. M. Ritchie, W. I. McAlexander, and R. G. Hulet. Photoassociative spectroscopy of long-range states of ultracold $^6Li_2$ and $^7Li_2$. *J. Chem. Phys.* **103**, 7773 (1995).

[All63] H. C. Allen, Jr. and P. Cross. Molecular Vib-Rotors. John Wiley and Sons, New York (1963).

[And06] A. André, D. DeMille, J. M. Doyle, M. D. Lukin, S. E. Maxwell, P. Rabl, R. J. Schoelkopf, and P. Zoller. A coherent all-electrical interface between polar molecules and mesoscopic superconducting resonators. *Nature Phys.* **2**, 636 (2006).

[Ape85] E. C. Apel and E. K. C. Lee. Electronic Spectra and Single Rotational Level Fluorescence Lifetimes of Jet-Cooled H_2CO: The $\tilde{A}^1A_2 \leftarrow \tilde{X}^1A_1$ $2_0^1 6_0^1$, $2_0^1 4_0^3$, and $2_0^1 4_0^1 6_0^1$. *J. Phys. Chem.* **89**, 1391 (1985).

[Ash70] A. Ashkin. Atomic-Beam Deflection by Resonance-Radiation Pressure. *Phys. Rev. Lett.* **25**, 1321 (1970).

[Ash78] A. Ashkin. Trapping of Atoms by Resonance Radiation Pressure. *Phys. Rev. Lett.* **40**, 729 (1978).

[Avd02] A. V. Avdeenkov and J. L. Bohn. Collisional dynamics of ultracold OH molecules in an electrostatic field. *Phys. Rev. A* **66**, 052718 (2002).

[Bal01] N. Balakrishnan and A. Dalgarno. Chemistry at ultracold temperatures. *Chem. Phys. Lett.* **341**, 652 (2001).

[Bal02] N. Balakrishnan and A. Dalgarno. Erratum to: "Chemistry at ultracold temperatures" [Chem. Phys. Lett. 341 (2001) 652]. *Chem. Phys. Lett.* **351**, 159 (2002).

[Bar01] P. F. Barker and M. N. Shneider. Optical microlinear accelerator for molecules and atoms. *Phys. Rev. A* **64**, 033408 (2001).

[Bar02] P. F. Barker and M. N. Shneider. Slowing molecules by optical microlinear deceleration. *Phys. Rev. A* **66**, 065402 (2002).

[Bel09a] M. T. Bell, A. D. Gingell, J. M. Oldham, T. P. Softley, and S. Willitsch. Ion-molecule chemistry at very low temperatures: cold chemical reactions between Coulomb-crystallized ions and velocity-selected neutral molecules. *Faraday Discuss.* **142**, 73 (2009).

[Bel09b] M. T. Bell and T. P. Softley. Ultracold molecules and ultracold chemistry. *Mol. Phys.* **107**, 99 (2009).

[Bet99] H. L. Bethlem, G. Berden, and G. Meijer. Decelerating Neutral Dipolar Molecules. *Phys. Rev. Lett.* **83**, 1558 (1999).

[Bet00] H. L. Bethlem, G. Berden, F. M. H. Crompvoets, R. T. Jongma, A. J. A. van Roij, and G. Meijer. Electrostatic trapping of ammonia molecules. *Nature* **406**, 491 (2000).

[Bet02] H. L. Bethlem, F. M. H. Crompvoets, R. T. Jongma, S. Y. T. van de Meerakker, and G. Meijer. Deceleration and trapping of ammonia using time-varying electric fields. *Phys. Rev. A* **65**, 053416 (2002).

[Bet06] H. L. Bethlem, J. van Veldhoven, M. Schnell, and G. Meijer. Trapping polar molecules in an ac trap. *Phys. Rev. A* **74**, 063403 (2006).

[Bic05] B. J. Bichsel, Cold nitric oxide molecules from a Stark guide, Ph.D. thesis, University of Oklahoma (2005).

[Bil08] J. Billy, V. Josse, Z. Zuo, A. Bernard, B. Hambrecht, P. Lugan, D. Clément, L. Sanchez-Palencia, P. Bouyer, and A. Aspect. Direct observation of Anderson localization of matter waves in a controlled disorder. *Nature* **453**, 891 (2008).

[Bir52] G. Birnbaum and S. K. Chatterjee. The Dielectric Constant of Water Vapor in the Microwave Region. *J. Appl. Phys.* **23**, 220 (1952).

[Bjo80] G. C. Bjorklund. Frequency-modulation spectroscopy: a new method for measuring weak absorptions and dispersions. *Opt. Lett.* **5**, 15 (1980).

[Bjo83] G. C. Bjorklund, M. D. Levenson, W. Lenth, and C. Ortiz. Frequency Modulation (FM) Spectroscopy. *Appl. Phys. B* **32**, 145 (1983).

[Bla03] A. T. Black, H. W. Chan, and V. Vuletić. Observation of Collective Friction Forces due to Spatial Self-Organization of Atoms: From Rayleigh to Bragg Scattering. *Phys. Rev. Lett.* **91**, 203001 (2003).

[Blo08] I. Bloch, J. Dalibard, and W. Zwerger. Many-body physics with ultracold gases. *Rev. Mod. Phys.* **80**, 885 (2008).

[Boh83] C. F. Bohren and D. R. Huffman. Absorption and Scattering of Light by Small Particles. John Wiley and Sons, New York (1983).

[Boh01] J. L. Bohn. Inelastic collisions of ultracold polar molecules. *Phys. Rev. A* **63**, 052714 (2001).

[Bol08] P. A. Bolokhov, M. Pospelov, and M. Romalis. Electric dipole moments as probes of CPT invariance. *Phys. Rev. D* **78**, 057702 (2008).

[Bow06] J. M. Bowman and X. Zhang. New insights on reaction dynamics from formaldehyde photodissociation. *Phys. Chem. Chem. Phys.* **8**, 321 (2006).

[Bri72] A. H. Brittain, A. P. Cox, G. Duxbury, T. G. Hersey, and R. G. Jones. The dipole moment of water: Stark effects in D_2O and HDO. *Mol. Phys.* **24**, 843 (1972).

[Bul09] I. Buluta and F. Nori. Quantum simulators. *Science* **326**, 108 (2009).

[Bun05] P. R. Bunker and P. Jensen. Fundamentals of Molecular Symmetry. Institute of Physics Publishing, Bristol (2005).

[Bun06] P. R. Bunker and P. Jensen. Molecular Symmetry and Spectroscopy. NRC Research Press, Ottawa, Ontario, Canada, 2nd edition (2006).

[Cam07] W. C. Campbell, E. Tsikata, H.-I. Lu, L. D. van Buuren, and J. M. Doyle. Magnetic Trapping and Zeeman Relaxation of NH ($X^3\Sigma^-$). *Phys. Rev. Lett.* **98**, 213001 (2007).

[Cam08] W. C. Campbell, G. C. Groenenboom, H.-I. Lu, E. Tsikata, and J. M. Doyle. Time-Domain Measurement of Spontaneous Vibrational Decay of Magnetically Trapped NH. *Phys. Rev. Lett.* **100**, 083003 (2008).

[Cam09] W. C. Campbell, T. V. Tscherbul, H.-I. Lu, E. Tsikata, R. V. Krems, and J. M. Doyle. Mechanism of Collisional Spin Relaxation in $^3\Sigma$ Molecules. *Phys. Rev. Lett.* **102**, 013003 (2009).

[Can90] C. A. Cantrell, J. A. Davidson, A. H. McDaniel, R. E. Shetter, and J. G. Calvert. Temperature-Dependent Formaldehyde Cross Sections in the Near-Ultraviolet Spectral Region. *J. Phys. Chem.* **94**, 3902 (1990).

[Car09] L. D. Carr, D. DeMille, R. V. Krems, and J. Ye. Cold and ultracold molecules: science, technology and applications. *New J. Phys.* **11**, 055049 (2009).

[Cha03] H. W. Chan, A. T. Black, and V. Vuletić. Observation of Collective-Emission-Induced Cooling of Atoms in an Optical Cavity. *Phys. Rev. Lett.* **90**, 063003 (2003).

[Chr64] J. H. Christenson, J. W. Cronin, V. L. Fitch, and R. Turlay. Evidence for the 2π Decay of the K_2^0 Meson. *Phys. Rev. Lett.* **13**, 138 (1964).

[Cla78] J. H. Clark, C. B. Moore, and N. S. Nogar. The photochemistry of formaldehyde: Absolute quantum yields, radical reactions, and NO reactions. *J. Chem. Phys.* **68**, 1264 (1978).

[Clo73] S. A. Clough, Y. Beers, G. P. Klein, and L. S. Rothman. Dipole moment of water from Stark measurements of H_2O, HDO, and D_2O. *J. Chem. Phys.* **59**, 2254 (1973).

[Clo83] D. J. Clouthier and D. A. Ramsay. The Spectroscopy of Formaldehyde and Thioformaldehyde. *Annu. Rev. Phys. Chem.* **34**, 31 (1983).

[Co05] D. T. Co, T. F. Hanisco, J. G. Anderson, and F. N. Keutsch. Rotationally Resolved Absorption Cross Sections of Formaldehyde in the 28100–28500 cm^{-1} (351–356 nm) Spectral Region: Implication for in Situ LIF Measurements. *J. Phys. Chem. A* **109**, 10675 (2005).

[Com99] E. D. Commins, Electric Dipole Moments of Leptons, in Adv. At. Mol. Opt. Phys., volume 40, editors B. Bederson and H. Walther, Elsevier Academic Press, San Diego, USA (1999).

[Com07] E. D. Commins, J. D. Jackson, and D. P. DeMille. The electric dipole moment of the electron: An intuitive explanation for the evasion of Schiff's theorem. *Am. J. Phys.* **75**, 532 (2007).

[Cor99] P. B. Corkum, C. Ellert, M. Mehendale, P. Dietrich, S. Hankin, S. Aseyev, D. Rayner, and D. Villeneuve. Molecular science with strong laser fields. *Faraday Discuss.* **113**, 47 (1999).

[Cor02] E. A. Cornell and C. E. Wieman. Nobel Lecture: Bose-Einstein condensation in a dilute gas, the first 70 years and some recent experiments. *Rev. Mod. Phys.* **74**, 875 (2002).

[Côt06] R. Côté. Quantum Information Processing: Bridge between two length-scales. *Nature Phys.* **2**, 583 (2006).

[Cro44] P. C. Cross, R. M. Hainer, and G. W. King. The Asymmetric Rotor II. Calculation of Dipole Intensities and Line Classification. *J. Chem. Phys.* **12**, 210 (1944).

[Cro01] F. M. H. Crompvoets, H. L. Bethlem, R. T. Jongma, and G. Meijer. A prototype storage ring for neutral molecules. *Nature* **411**, 174 (2001).

[Dan08] J. G. Danzl, E. Haller, M. Gustavsson, M. J. Mark, R. Hart, N. Bouloufa, O. Dulieu, H. Ritsch, and H.-C. Nägerl. Quantum Gas of Deeply Bound Ground State Molecules. *Science* **321**, 1062 (2008).

[Dan09] J. G. Danzl, M. J. Mark, E. Haller, M. Gustavsson, R. Hart, A. Liem, H. Zellmer, and H.-C. Nägerl. Deeply bound ultracold molecules in an optical lattice. *New J. Phys.* **11**, 055036 (2009).

[Dei08a] J. Deiglmayr, M. Aymar, R. Wester, M. Weidemüller, and O. Dulieu. Calculations of static dipole polarizabilities of alkali dimers: Prospects for alignment of ultracold molecules. *J. Chem. Phys.* **129**, 064309 (2008).

[Dei08b] J. Deiglmayr, A. Grochola, M. Repp, K. Mörtlbauer, C. Glück, J. Lange, O. Dulieu, R. Wester, and M. Weidemüller. Formation of Ultracold Polar Molecules in the Rovibrational Ground State. *Phys. Rev. Lett.* **101**, 133004 (2008).

[Dem99] W. Demtröder. Experimentalphysik 2: Elektrizität und Optik. Springer, Berlin, 2nd edition (1999).

[DeM00] D. DeMille, F. Bay, S. Bickman, D. Kawall, D. Krause, Jr., S. E. Maxwell, and L. R. Hunter. Investigation of PbO as a system for measuring the electric dipole moment of the electron. *Phys. Rev. A* **61**, 052507 (2000).

[DeM02] D. DeMille. Quantum Computation with Trapped Polar Molecules. *Phys. Rev. Lett.* **88**, 067901 (2002).

[Dem03a] W. Demtröder. Laser Spectroscopy: Basic Concepts and Instrumentation. Springer, Berlin, 3rd edition (2003).

[Dem03b] W. Demtröder. Molekülphysik: Theoretische Grundlagen und experimentelle Methoden. Oldenbourg, München (2003).

[dH08] E. de Hoffmann and V. Stroobant. Mass Spectrometry: Principles and Applications. John Wiley and Sons, West Sussex, England, 3rd edition (2008).

[Die34] G. H. Dieke and G. B. Kistiakowsky. The Structure of the Ultraviolet Absorption Spectrum of Formaldehyde. I. *Phys. Rev.* **45**, 4 (1934).

[DL81] G. Di Lonardo and A. Trombetti. Dipole moment of the $\nu_2 = 1$ state of ND_3 by saturation laser Stark spectroscopy. *Chem. Phys. Lett.* **84**, 327 (1981).

[Dom02] P. Domokos and H. Ritsch. Collective Cooling and Self-Organization of Atoms in a Cavity. *Phys. Rev. Lett.* **89**, 253003 (2002).

[Don05] G. Dong, W. Lu, P. F. Barker, and M. N. Shneider. Cold molecules in pulsed optical lattices. *Prog. Quantum Electron.* **29**, 1 (2005).

[Dow93] J. P. Dowling. Spontaneous Emission in Cavities: How Much More Classical Can You Get? *Found. Phys.* **23**, 895 (1993).

[Doy04] J. Doyle, B. Friedrich, R. V. Krems, and F. Masnou-Seeuws. Editorial: Quo vadis, cold molecules? *Eur. Phys. J. D* **31**, 149 (2004).

[DR04] M. D. Di Rosa. Laser-cooling molecules. *Eur. Phys. J. D* **31**, 395 (2004).

[Dul06] O. Dulieu, M. Raoult, and E. Tiemann. Cold molecules: a chemistry kitchen for physicists? *J. Phys. B* **39**(19) (2006).

[Dür04] S. Dürr, T. Volz, A. Marte, and G. Rempe. Observation of Molecules Produced from a Bose-Einstein Condensate. *Phys. Rev. Lett.* **92**, 020406 (2004).

[Dyk73] T. R. Dyke and J. S. Muenter. Electric dipole moments of low J states of H_2O and D_2O. *J. Chem. Phys.* **59**, 3125 (1973).

[Ego02] D. Egorov, T. Lahaye, W. Schöllkopf, B. Friedrich, and J. M. Doyle. Buffer-gas cooling of atomic and molecular beams. *Phys. Rev. A* **66**, 043401 (2002).

[Ego04] D. Egorov, W. C. Campbell, B. Friedrich, S. Maxwell, E. Tsikata, L. D. van Buuren, and J. M. Doyle. Buffer-gas cooling of NH via the beam loaded buffer-gas method. *Eur. Phys. J. D* **31**, 307 (2004).

[Eli03] M. S. Elioff, J. J. Valentini, and D. W. Chandler. Subkelvin Cooling NO Molecules via "Billiard-like" Collisions with Argon. *Science* **302**, 1940 (2003).

[Fey82] R. Feynman. Simulating physics with computers. *Int. J. Theor. Phys.* **21**, 467 (1982).

[Fil08] F. Filsinger, U. Erlekam, G. von Helden, J. Küpper, and G. Meijer. Selector for Structural Isomers of Neutral Molecules. *Phys. Rev. Lett.* **100**, 133003 (2008).

[Fio98] A. Fioretti, D. Comparat, A. Crubellier, O. Dulieu, F. Masnou-Seeuws, and P. Pillet. Formation of Cold Cs_2 Molecules through Photoassociation. *Phys. Rev. Lett.* **80**, 4402 (1998).

[Ful04] R. Fulton, A. I. Bishop, and P. F. Barker. Optical Stark Decelerator for Molecules. *Phys. Rev. Lett.* **93**, 243004 (2004).

[Ful06a] R. Fulton, A. I. Bishop, M. N. Shneider, and P. F. Barker. Controlling the motion of cold molecules with deep periodic optical potentials. *Nature Phys.* **2**, 465 (2006).

[Ful06b] R. Fulton, A. I. Bishop, M. N. Shneider, and P. F. Barker. Optical Stark deceleration of nitric oxide and benzene molecules using optical lattices. *J. Phys. B* **39**, S1097 (2006).

[Gan87] S. R. Gandhi and R. B. Bernstein. Focusing and state selection of NH_3 and OCS by the electrostatic hexapole via first- and second-order Stark effects. *J. Chem. Phys.* **87**, 6457 (1987).

[Gha99] B. Ghaffari, J. M. Gerton, W. I. McAlexander, K. E. Strecker, D. M. Homan, and R. G. Hulet. Laser-free slow atom source. *Phys. Rev. A* **60**, 3878 (1999).

[Gil06] J. J. Gilijamse, S. Hoekstra, S. Y. T. van de Meerakker, G. C. Groenenboom, and G. Meijer. Near-Treshold Inelastic Collisions Using Molecular Beams with a Tunable Velocity. *Science* **313**, 1617 (2006).

[Gil07] J. J. Gilijamse, S. Hoekstra, S. A. Meek, M. Metsälä, S. Y. T. van de Meerakker, G. Meijer, and G. C. Groenenboom. The radiative lifetime of metastable CO ($a^3\Pi, v = 0$). *J. Chem. Phys.* **127**, 221102 (2007).

[Gio08] S. Giorgini, L. P. Pitaevskii, and S. Stringari. Theory of ultracold atomic Fermi gases. *Rev. Mod. Phys.* **80**, 1215 (2008).

[GM80] V. Ghaem-Maghami and A. D. May. Rayleigh-Brillouin spectrum of compressed He, Ne, and Ar. I. Scaling. *Phys. Rev. A* **22**, 692 (1980).

[Gol48] S. Golden, T. Wentink, R. Hillger, and M. W. P. Strandberg. Stark Spectrum of H_2O. *Phys. Rev.* **73**, 92 (1948).

[Gor70] W. Gordy and R. L. Cook. Microwave Molecular Spectra. Techniques of Organic Chemistry, Volume IX: Chemical Applications of Spectroscopy, Part II, Interscience Publishers, New York (1970).

[Goy83] P. Goy, J. M. Raimond, M. Gross, and S. Haroche. Observation of Cavity-Enhanced Single-Atom Spontaneous Emission. *Phys. Rev. Lett.* **50**, 1903 (1983).

[Gre02] M. Greiner, O. Mandel, T. Esslinger, T. W. Hänsch, and I. Bloch. Quantum phase transition from a superfluid to a Mott insulator in a gas of ultracold atoms. *Nature* **415**, 39 (2002).

[Gri09] W. C. Griffith, M. D. Swallows, T. H. Loftus, M. V. Romalis, B. R. Heckel, and E. N. Fortson. Improved Limit on the Permanent Electric Dipole Moment of ^{199}Hg. *Phys. Rev. Lett.* **102**, 101601 (2009).

[Gro83] D. Grosjean, R. D. Swanson, and C. Ellis. Carbonyls in Los Angeles air: Contribution of direct emissions and photochemistry. *Sci. Tot. Environ.* **29**, 65 (1983).

[Gup99] M. Gupta and D. Herschbach. A Mechanical Means to Produce Intense Beams of Slow Molecules. *J. Phys. Chem. A* **103**, 10670 (1999).

[Gup01] M. Gupta and D. Herschbach. Slowing and Speeding Molecular Beams by Means of a Rapidly Rotating Source. *J. Phys. Chem. A* **105**, 1626 (2001).

[Hai99] T. D. Hain, R. M. Moision, and T. J. Curtiss. Hexapole state-selection and orientation of asymmetric top molecules: CH_2F_2. *J. Chem. Phys.* **111**, 6797 (1999).

[Hai04] C. Haimberger, J. Kleinert, M. Bhattacharya, and N. P. Bigelow. Formation and detection of ultracold ground-state polar molecules. *Phys. Rev. A* **70**, 021402(R) (2004).

[Hak03] H. Haken and H. C. Wolf. Moleküphysik und Quantenchemie: Einführung in die experimentellen und theoretischen Grundlagen. Springer, Berlin, 4th edition (2003).

[Hal67] E. A. Halevi, E. N. Haran, and B. Ravid. Dipole moment and polarizability differences between NH_3 and ND_3. *Chem. Phys. Lett.* **1**, 475 (1967).

[Hän75] T. W. Hänsch and A. L. Schawlow. Cooling of gases by laser radiation. *Opt. Comm.* **13**, 68 (1975).

[Hän80] T. W. Hänsch and B. Couillaud. Laser frequency stabilization by polarization spectroscopy of a reflecting reference cavity. *Opt. Comm.* **35**, 441 (1980).

[Hei87] D. J. Heinzen, J. J. Childs, J. E. Thomas, and M. S. Feld. Enhanced and Inhibited Visible Spontaneous Emission by Atoms in a Confocal Resonator. *Phys. Rev. Lett.* **58**, 1320 (1987).

[Hei06] C. E. Heiner, H. L. Bethlem, and G. Meijer. Molecular beams with a tunable velocity. *Phys. Chem. Chem. Phys.* **8**, 2666 (2006).

[Hei07] C. E. Heiner, D. Carty, G. Meijer, and H. L. Bethlem. A molecular synchrotron. *Nature Phys.* **3**, 115 (2007).

[Hel08] H. Helm, private communication (2008).

[Her45] G. Herzberg. Molecular Spectra and Molecular Structure, II. Infrared and Raman Spectra of Polyatomic Molecules. Van Nostrand Reinhold, New York (1945).

[Her50] G. Herzberg. Molecular Spectra and Molecular Structure, I. Spectra of Diatomic Molecules. Van Nostrand Reinhold, New York, 2nd edition (1950).

[Hij07a] M. Hijlkema, Single photons from a single atom trapped in a high-finesse optical cavity, Ph.D. thesis, Max-Planck-Institut für Quantenoptik, Garching, und Fakultät für Physik, Technische Universität München (2007).

[Hij07b] M. Hijlkema, B. Weber, H. P. Specht, S. C. Webster, A. Kuhn, and G. Rempe. A single-photon server with just one atom. *Nature Phys.* **3**, 253 (2007).

[Hin97] E. A. Hinds. Testing Time Reversal Symmetry Using Molecules. *Phys. Scr.* **T70**, 34 (1997).

[Hoe07] S. Hoekstra, J. J. Gilijamse, B. Sartakov, N. Vanhaecke, L. Scharfenberg, S. Y. T. van de Meerakker, and G. Meijer. Optical Pumping of Trapped Neutral Molecules by Blackbody Radiation. *Phys. Rev. Lett.* **98**, 133001 (2007).

[Hog08a] S. D. Hogan, A. W. Wiederkehr, M. Andrist, H. Schmutz, and F. Merkt. Slow beams of atomic hydrogen by multistage Zeeman deceleration. *J. Phys. B* **41**, 081005 (2008).

[Hog08b] S. D. Hogan, A. W. Wiederkehr, H. Schmutz, and F. Merkt. Magnetic Trapping of Hydrogen after Multistage Zeeman Deceleration. *Phys. Rev. Lett.* **101**, 143001 (2008).

[Hor78a] A. Horowitz and J. G. Calvert. The Quantum Efficiency of the Primary Processes in Formaldehyde Photolysis at 3130 Å and 25°C. *Int. J. Chem. Kin.* **10**, 713 (1978).

[Hor78b] A. Horowitz and J. G. Calvert. Wavelength Dependence of the Quantum Efficiencies of the Primary Processes in Formaldehyde Photolysis at 25°C. *Int. J. Chem. Kin.* **10**, 805 (1978).

[Hor97] P. Horak, G. Hechenblaikner, K. M. Gheri, H. Stecher, and H. Ritsch. Cavity-Induced Atom Cooling in the Strong Coupling Regime. *Phys. Rev. Lett.* **79**, 4974 (1997).

[Hud02] J. J. Hudson, B. E. Sauer, M. R. Tarbutt, and E. A. Hinds. Measurement of the Electron Electric Dipole Moment Using YbF Molecules. *Phys. Rev. Lett.* **89**, 023003 (2002).

[Hud06] E. R. Hudson, C. Ticknor, B. C. Sawyer, C. A. Taatjes, H. J. Lewandowski, J. R. Bochinski, J. L. Bohn, and J. Ye. Production of cold formaldehyde molecules for study and control of chemical reaction dynamics with hydroxyl radicals. *Phys. Rev. A* **73**, 063404 (2006).

[Hum08a] J. Humburg, Erzeugung langsamer und kalter Molekülstrahlen mittels einer rotierenden Düse, Master's thesis, Fakultät für Mathematik und Physik, Albert-Ludwigs-Universität Freiburg im Breisgau (2008).

[Hum08b] M. T. Hummon, W. C. Campbell, H.-I. Lu, E. Tsikata, Y. Wang, and J. M. Doyle. Magnetic trapping of atomic nitrogen (^{14}N) and cotrapping of NH ($X^3\Sigma^-$). *Phys. Rev. A* **78**, 050702(R) (2008).

[Hun91] L. R. Hunter. Tests of Time-Reversal Invariance in Atoms, Molecules, and the Neutron. *Science* **252**, 73 (1991).

[Ino04] S. Inouye, J. Goldwin, M. L. Olsen, C. Ticknor, J. L. Bohn, and D. S. Jin. Observation of Heteronuclear Feshbach Resonances in a Mixture of Bosons and Fermions. *Phys. Rev. Lett.* **93**, 183201 (2004).

[Jac99] J. D. Jackson. Classical Electrodynamics. John Wiley and Sons, New York, 3rd edition (1999).

[Joc03] S. Jochim, M. Bartenstein, A. Altmeyer, G. Hendl, S. Riedl, C. Chin, J. Hecker Denschlag, and R. Grimm. Bose-Einstein Condensation of Molecules. *Science* **302**, 2101 (2003).

[Jon06] K. M. Jones, E. Tiesinga, P. D. Lett, and P. S. Julienne. Ultracold photoassociation spectroscopy: Long-range molecules and atomic scattering. *Rev. Mod. Phys.* **78**, 483 (2006).

[Jun04a] T. Junglen, T. Rieger, S. A. Rangwala, P. W. H. Pinkse, and G. Rempe. Slow ammonia molecules in an electrostatic quadrupole guide. *Eur. Phys. J. D* **31**, 365 (2004).

[Jun04b] T. Junglen, T. Rieger, S. A. Rangwala, P. W. H. Pinkse, and G. Rempe. Two-Dimensional Trapping of Dipolar Molecules in Time-Varying Electric Fields. *Phys. Rev. Lett.* **92**, 223001 (2004).

[Jun05] T. Junglen, Guiding and Trapping of Cold Dipolar Molecules, Ph.D. thesis, Max-Planck-Institut für Quantenoptik, Garching, und Fakultät für Physik, Technische Universität München (2005).

[Kas62] A. Kastler. Atomes à l'Intérieur d'un Interféromètre Perot-Fabry. *Appl. Opt.* **1**, 17 (1962).

[Ker04a] A. J. Kerman, J. M. Sage, S. Sainis, T. Bergeman, and D. DeMille. Production and State-Selective Detection of Ultracold RbCs Molecules. *Phys. Rev. Lett.* **92**, 153001 (2004).

[Ker04b] A. J. Kerman, J. M. Sage, S. Sainis, T. Bergeman, and D. DeMille. Production of Ultracold, Polar RbCs* Molecules via Photoassociation. *Phys. Rev. Lett.* **92**, 033004 (2004).

[Ket02] W. Ketterle. Nobel lecture: When atoms behave as waves: Bose-Einstein condensation and the atom laser. *Rev. Mod. Phys.* **74**, 1131 (2002).

[Kin43] G. W. King, R. M. Hainer, and P. C. Cross. The Asymmetric Rotor I. Calculation and Symmetry Classification of Energy Levels. *J. Chem. Phys.* **11**, 27 (1943).

[Köh06] T. Köhler, K. Góral, and P. S. Julienne. Production of cold molecules via magnetically tunable Feshbach resonances. *Rev. Mod. Phys.* **78**, 1311 (2006).

[Kow07] M. Kowalewski, G. Morigi, P. W. H. Pinkse, and R. de Vivie-Riedle. Cavity cooling of translational and ro-vibrational motion of molecules: ab initio-based simulations for OH and NO. *Appl. Phys. B* **89**, 459 (2007).

[Koz02] M. G. Kozlov and D. DeMille. Enhancement of the Electric Dipole Moment of the Electron in PbO. *Phys. Rev. Lett.* **89**, 133001 (2002).

[Kra06] S. D. Kraft, P. Staanum, J. Lange, L. Vogel, R. Wester, and M. Weidemüller. Formation of ultracold LiCs molecules. *J. Phys. B* **39**, S993 (2006).

[Kre05] R. V. Krems. Molecules near absolute zero and external field control of atomic and molecular dynamics. *Int. Rev. Phys. Chem.* **24**, 99 (2005).

[Kre08] R. V. Krems. Cold controlled chemistry. *Phys. Chem. Chem. Phys.* **10**, 4079 (2008).

[Kro75] H. W. Kroto. Molecular Rotation Spectra. John Wiley and Sons, New York (1975).

[Küp09] J. Küpper, F. Filsinger, and G. Meijer. Manipulating the motion of large neutral molecules. *Faraday Discuss.* **142**, 155 (2009).

[Lan08] F. Lang, K. Winkler, C. Strauss, R. Grimm, and J. Hecker Denschlag. Ultracold Triplet Molecules in the Rovibrational Ground State. *Phys. Rev. Lett.* **101**, 133005 (2008).

[Lee56] T. D. Lee and C. N. Yang. Question of Parity Conservation in Weak Interactions. *Phys. Rev.* **104**, 254 (1956).

[Lee57] T. D. Lee, R. Oehme, and C. N. Yang. Remarks on Possible Noninvariance under Time Reversal and Charge Conjugation. *Phys. Rev.* **106**, 340 (1957).

[Lei09] D. R. Leibrandt, J. Labaziewicz, V. Vuletić, and I. L. Chuang. Cavity Sideband Cooling of a Single Trapped Ion. *Phys. Rev. Lett.* **103**, 103001 (2009).

[Let93] P. D. Lett, K. Helmerson, W. D. Phillips, L. P. Ratliff, S. L. Rolston, and M. E. Wagshul. Spectroscopy of Na_2 by photoassociation of laser-cooled Na. *Phys. Rev. Lett.* **71**, 2200 (1993).

[Lev08] B. L. Lev, A. Vukics, E. R. Hudson, B. C. Sawyer, P. Domokos, H. Ritsch, and J. Ye. Prospects for the cavity-assisted laser cooling of molecules. *Phys. Rev. A* **77**, 023402 (2008).

[Lew06] M. Lewenstein. Polar molecules in topological order. *Nature Phys.* **2**, 309 (2006).

[Lew07] M. Lewenstein, A. Sanpera, V. Ahufinger, B. Damski, A. Sen, and U. Sen. Ultracold atomic gases in optical lattices: mimicking condensed matter physics and beyond. *Adv. Phys.* **56**, 243 (2007).

[Lid90] D. R. Lide (Editor) CRC Handbook of Chemistry and Physics. CRC Press, Boca Raton, 71st edition (1990).

[Man04] M. W. Mancini, G. D. Telles, A. R. L. Caires, V. S. Bagnato, and L. G. Marcassa. Observation of Ultracold Ground-State Heteronuclear Molecules. *Phys. Rev. Lett* **92**, 133203 (2004).

[Mau04] P. Maunz, T. Puppe, I. Schuster, N. Syassen, P. W. H. Pinkse, and G. Rempe. Cavity cooling of a single atom. *Nature* **428**, 50 (2004).

[Mau05a] P. Maunz, T. Puppe, I. Schuster, N. Syassen, P. W. H. Pinkse, and G. Rempe. Normal-Mode Spectroscopy of a Single-Bound-Atom–Cavity System. *Phys. Rev. Lett.* **94**, 033002 (2005).

[Mau05b] P. L. W. Maunz, Cavity cooling and spectroscopy of a bound atom-cavity system, Ph.D. thesis, Max-Planck-Institut für Quantenoptik, Garching, und Fakultät für Physik, Technische Universität München (2005).

[Max05] S. E. Maxwell, N. Brahms, R. deCarvalho, D. R. Glenn, J. S. Helton, S. V. Nguyen, D. Patterson, J. Petricka, D. DeMille, and J. M. Doyle. High-Flux Beam Source for Cold, Slow Atoms or Molecules. *Phys. Rev. Lett.* **95**, 173201 (2005).

[Maz07] A. Mazzei, S. Götzinger, L. de S. Menezes, G. Zumofen, O. Benson, and V. Sandoghdar. Controlled Coupling of Counterpropagating Whispering-Gallery Modes by a Single Rayleigh Scatterer: A Classical Problem in a Quantum Optical Light. *Phys. Rev. Lett.* **99**, 173603 (2007).

[McQ69] R. D. McQuigg and J. G. Calvert. The Photodecomposition of CH_2O, CD_2O, CHDO, and CH_2O–CD_2O Mixtures at Xenon Flash Lamp Intensities. *J. Am. Chem. Soc.* **91**, 1590 (1969).

[Mee04] W. L. Meerts, M. Schmit, and G. C. Groenenboom. New applications of the genetic algorithm for the interpretation of high-resolution spectra. *Can. J. Chem.* **82**, 804 (2004).

[Mee06a] W. L. Meerts and M. Schmitt. Application of genetic algorithms in automated assignments of high-resolution spectra. *Int. Rev. Phys. Chem.* **25**, 353 (2006).

[Mee06b] W. L. Meerts and M. Schmitt. A new automated assign and analysing method for high-resolution rotalionally resolved spectra using genetic algorithms. *Phys. Scr.* **73**, C47 (2006).

[Mee08] S. A. Meek, H. L. Bethlem, H. Conrad, and G. Meijer. Trapping Molecules on a Chip in Traveling Potential Wells. *Phys. Rev. Lett.* **100**, 153003 (2008).

[Mee09] S. A. Meek, H. Conrad, and G. Meijer. Trapping Molecules on a Chip. *Science* **324**, 5935 (2009).

[Met99] H. J. Metcalf and P. van der Straten. Laser Cooling and Trapping. Springer, New York (1999).

[Mey08] E. R. Meyer and J. L. Bohn. Prospects for an electron electric-dipole moment search in metastable ThO and ThF^+. *Phys. Rev. A* **78**, 010502(R) (2008).

[Mey09] E. R. Meyer and J. L. Bohn. Electron electric-dipole-moment searches based on alkali-metal- or alkaline-earth-metal-bearing molecules. *Phys. Rev. A* **80**, 042508 (2009).

[Mic06] A. Micheli, G. K. Brennen, and P. Zoller. A toolbox for lattice-spin models with polar molecules. *Nature Phys.* **2**, 341 (2006).

[Mik08a] J. Mikosch, R. Otto, S. Trippel, C. Eichhorn, M. Weidemüller, and R. Wester. Inverse Temperature Dependent Lifetimes of Transient S_N2 Ion-Dipole Complexes. *J. Phys. Chem. A* **112**, 10448 (2008).

[Mik08b] J. Mikosch, S. Trippel, C. Eichhorn, R. Otto, U. Lourderaj, J. X. Zhang, W. L. Hase, M. Weidemüller, and R. Wester. Imaging Nucleophilic Substitution Dynamics. *Science* **319**, 183 (2008).

[Mil73] P. W. Milonni and P. L. Knight. Spontaneous emission between mirrors. *Opt. Comm.* **9**, 119 (1973).

[Mil81] C. K. Miller, B. J. Orr, and J. F. Ward. An interacting segment model of molecular electric tensor properties: Application to dipole moments, polarizabilities, and hyperpolarizabilities for the halogenated methanes. *J. Chem. Phys.* **74**, 4858 (1981).

[Mil93] J. D. Miller, R. A. Cline, and D. J. Heinzen. Photoassociation spectrum of ultracold Rb atoms. *Phys. Rev. Lett.* **71**, 2204 (1993).

[Mom09] T. Momose, private communication (2009).

[Moo78] G. K. Moortgart, F. Šlemr, W. Seiler, and P. Warneck. Photolysis of Formaldehyde: Relative quantum yields of H_2 and CO in the wavelength range 270–360 nm. *Chem. Phys. Lett.* **54**, 444 (1978).

[Moo83] C. B. Moore and J. C. Weisshaar. Formaldehyde Photochemistry. *Annu. Rev. Phys. Chem.* **34**, 525 (1983).

[Mor07] G. Morigi, P. W. H. Pinkse, M. Kowalewski, and R. de Vivie-Riedle. Cavity Cooling of Internal Molecular Motion. *Phys. Rev. Lett.* **99**, 073001 (2007).

[Mot07] M. Motsch, M. Schenk, L. D. van Buuren, M. Zeppenfeld, P. W. H. Pinkse, and G. Rempe. Internal-state thermometry by depletion spectroscopy in a cold guided beam of formaldehyde. *Phys. Rev. A* **76**, 061402(R) (2007).

[Mot08] M. Motsch, M. Schenk, M. Zeppenfeld, M. Schmitt, W. L. Meerts, P. W. H. Pinkse, and G. Rempe. Spectroscopy of the $\tilde{A}^1A_2 \leftarrow \tilde{X}^1A_1$ transition of formaldehyde in the 30140–30790 cm^{-1} range: the $2_0^1 4_0^3$ and $2_0^2 4_0^1$ rovibrational bands. *J. Mol. Spec.* **252**, 25 (2008).

[Mot09a] M. Motsch, C. Sommer, M. Zeppenfeld, L. D. van Buuren, G. Rempe, and P. W. H. Pinkse. Collisional effects in the formation of cold guided beams of polar molecules. *New J. Phys.* **11**, 055030 (2009).

[Mot09b] M. Motsch, L. D. van Buuren, C. Sommer, M. Zeppenfeld, G. Rempe, and P. W. H. Pinkse. Cold guided beams of water isotopologs. *Phys. Rev. A* **79**, 013405 (2009).

[Mot09c] M. Motsch, M. Zeppenfeld, P. W. H. Pinkse, and G. Rempe, Cavity-Enhanced Rayleigh Scattering, arXiv.org:0904.4405 (2009).

[Mud09] M. Mudrich, private communication (2009).

[Mün99a] P. Münstermann, Dynamik einzelner Atome in einem optischen Resonator höchster Finesse, Ph.D. thesis, Fakultät für Physik, Universität Konstanz (1999).

[Mün99b] P. Münstermann, T. Fischer, P. W. H. Pinkse, and G. Rempe. Single slow atoms from an atomic fountain observed in a high-finesse optical cavity. *Opt. Comm.* **159**, 63 (1999).

[Mur06a] K. Murr. Large Velocity Capture Range and Low Temperatures with Cavities. *Phys. Rev. Lett.* **96**, 253001 (2006).

[Mur06b] K. Murr, S. Nußmann, T. Puppe, M. Hijlkema, B. Weber, S. C. Webster, A. Kuhn, and G. Rempe. Three-dimensional cavity cooling and trapping in an optical lattice. *Phys. Rev. A* **73**, 063415 (2006).

[Nar07a] E. Narevicius, A. Libson, M. F. Riedel, C. G. Parthey, I. Chavez, U. Even, and M. G. Raizen. Coherent Slowing of a Supersonic Beam with an Atomic Paddle. *Phys. Rev. Lett.* **98**, 103201 (2007).

[Nar07b] E. Narevicius, C. G. Parthey, A. Libson, J. Narevicius, I. Chavez, U. Even, and M. G. Raizen. An atomic coilgun: using pulsed magnetic fields to slow a supersonic beam. *New J. Phys.* **9**, 358 (2007).

[Nar07c] E. Narevicius, C. G. Parthey, A. Libson, M. Riedel, U. Even, and M. G. Raizen. Towards magnetic slowing of atoms and molecules. *New J. Phys.* **9**, 96 (2007).

[Nar08a] E. Narevicius, A. Libson, C. G. Parthey, I. Chavez, J. Narevicius, U. Even, and M. G. Raizen. Stopping Supersonic Beams with a Series of Pulsed Electromagnetic Coils: An Atomic Coilgun. *Phys. Rev. Let.* **100**, 093003 (2008).

[Nar08b] E. Narevicius, A. Libson, C. G. Parthey, I. Chavez, J. Narevicius, U. Even, and M. G. Raizen. Stopping supersonic oxygen with a series of pulsed electromagnetic coils: A molecular coilgun. *Phys. Rev. A* **77**, 051401(R) (2008).

[Neu78] W. Neuhauser, M. Hohenstatt, P. Toschek, and H. Dehmelt. Optical-Sideband Cooling of Visible Atom Cloud Confined in Parabolic Well. *Phys. Rev. Lett.* **41**, 233 (1978).

[Ni08] K.-K. Ni, S. Ospelkaus, M. H. G. de Miranda, A. Pe'er, B. Neyenhuis, J. J. Zirbel, S. Kotochigova, P. S. Julienne, D. S. Jin, and J. Ye. A High Phase-Space-Density Gas of Polar Molecules. *Science* **322**, 231 (2008).

[Ni09] K.-K. Ni, S. Ospelkaus, D. J. Nesbitt, J. Ye, and D. S. Jin. A dipolar gas of ultracold molecules. *Phys. Chem. Chem. Phys.* **11**, 9626 (2009).

[Nuß05a] S. Nußmann, Kühlen und Positionieren eines Atoms in einem optischen Resonator, Ph.D. thesis, Max-Planck-Institut für Quantenoptik, Garching, und Fakultät für Physik, Technische Universität München (2005).

[Nuß05b] S. Nußmann, K. Murr, M. Hijlkema, B. Weber, A. Kuhn, and G. Rempe. Vacuum-stimulated cooling of single atoms in three dimensions. *Nature Phys.* **1**, 122 (2005).

[Osp08] S. Ospelkaus, A. Pe'er, K.-K. Ni, J. J. Zirbel, B. Neyenhuis, S. Kotochigova, P. S. Julienne, J. Ye, and D. S. Jin. Efficient state transfer in an ultracold dense gas of heteronuclear molecules. *Nature Phys.* **4**, 622 (2008).

[Osp09] S. Ospelkaus, K.-K. Ni, M. H. G. de Miranda, B. Neyenhuis, D. Wang, S. Kotochigova, P. S. Julienne, D. S. Jin, and J. Ye. Ultracold polar molecules near quantum degeneracy. *Faraday Discuss.* **142**, 351 (2009).

[Pan02] X. Pan, M. N. Shneider, and R. B. Miles. Coherent Rayleigh-Brillouin Scattering. *Phys. Rev. Lett.* **89**, 183001 (2002).

[Pat07] D. Patterson and J. M. Doyle. Bright, guided molecular beam with hydrodynamic enhancement. *J. Chem. Phys.* **126**, 154307 (2007).

[Pat09] D. Patterson, J. Rasmussen, and J. M. Doyle. Intense atomic and molecular beams via neon buffer-gas cooling. *New J. Phys.* **11**, 055018 (2009).

[Pau55] W. Pauli (Editor) Niels Bohr and the Development of Physics: Essays Dedicated to Niels Bohr on the Occasion of his 70. Birthday. Mc. Graw-Hill, New York (1955).

[Pau00] H. Pauly. Atom, Molecule, and Cluster Beams I: Basic Theory, Production and Detection of Thermal Energy Beams. Springer, Berlin (2000).

[Phi98] W. D. Phillips. Nobel Lecture: Laser cooling and trapping of neutral atoms. *Rev. Mod. Phys.* **70**, 721 (1998).

[Pie08] A. Piechaczek, Simulation, Konstruktion und Verwirklichung einer Stark-Effekt geführten Quelle für langsame Moleküle, Master's thesis, Fakultät für Mathematik und Physik, Albert-Ludwigs-Universität Freiburg im Breisgau (2008).

[Pil00] P. Pillet, C. Drag, B. Laburthe Tolra, D. Comparat, A. Fioretti, S. Guibal, C. Amiot, A. Crubellier, O. Dulieu, and F. Masnou-Seeuws. Photoassociative spectroscopy and formation of cold molecules. *Phys. Scr.* **T86**, 38 (2000).

[Pop05] F. D. Pope, C. A. Smith, M. N. R. Ashfold, and A. J. Orr-Ewing. High-resolution absorption cross sections of formaldehyde at wavelengths from 313 to 320 nm. *Phys. Chem. Chem. Phys.* **7**, 79 (2005).

[Pri08] G. N. Price, S. T. Bannerman, K. Viering, E. Narevicius, and M. G. Raizen. Single-Photon Atomic Cooling. *Phys. Rev. Lett.* **100**, 093004 (2008).

[Pur46] E. M. Purcell. Spontaneous emission probabilities at radio frequencies. *Phys. Rev.* **69**, 681 (1946).

[Pur50] E. M. Purcell and N. F. Ramsey. On the Possibility of Electric Dipole Moments for Elementary Particles and Nuclei. *Phys. Rev.* **78**, 807 (1950).

[Rab06] P. Rabl, D. DeMille, J. M. Doyle, M. D. Lukin, R. J. Schoelkopf, and P. Zoller. Hybrid Quantum Processors: Molecular Ensembles as Quantum Memory for Solid State Circuits. *Phys. Rev. Lett.* **97**, 033003 (2006).

[Rai09] M. G. Raizen. Comprehensive Control of Atomic Motion. *Science* **324**, 1403 (2009).

[Ram90] N. F. Ramsay. Molecular Beams. Oxford University Press, Oxford (1990).

[Ran03] S. A. Rangwala, T. Junglen, T. Rieger, P. W. H. Pinkse, and G. Rempe. Continuous source of translationally cold dipolar molecules. *Phys. Rev. A* **67**, 043406 (2003).

[Ray99] Lord Rayleigh. XXXIV. On the transmission of light through an atmosphere containing small particles in suspension, and on the origin of the blue of the sky. *Phil. Mag. Ser. 5* **47**, 375 (1899).

[Reg02] B. C. Regan, E. D. Commins, C. J. Schmidt, and D. DeMille. New Limit on the Electron Electric Dipole Moment. *Phys. Rev. Lett.* **88**, 071805 (2002).

[Reg03] C. A. Regal, C. Ticknor, J. L. Bohn, and D. S. Jin. Creation of ultracold molecules from a Fermi gas of atoms. *Nature* **424**, 47 (2003).

[Rei78] J. P. Reilly, J. H. Clark, C. B. Moore, and G. C. Pimentel. HCO production, vibrational relaxation, chemical kinetics, and spectroscopy following laser photolysis of formaldehyde. *J. Chem. Phys.* **69**, 4381 (1978).

[Rie99] K. Riedel, R. Weller, and O. Schrems. Variability of formaldehyde in the Antarctic troposhere. *Phys. Chem. Chem. Phys.* **1**, 5523 (1999).

[Rie05] T. Rieger, T. Junglen, S. A. Rangwala, P. W. H. Pinkse, and G. Rempe. Continuous Loading of an Electrostatic Trap for Polar Molecules. *Phys. Rev. Lett.* **95**, 173002 (2005).

[Rie06] T. Rieger, T. Junglen, S. A. Rangwala, G. Rempe, P. W. H. Pinkse, and J. Bulthuis. Water vapour at a translational temperature of 1 K. *Phys. Rev. A* **73**, 061402(R) (2006).

[Rie07a] T. Rieger, Elektrisches Speichern neutraler Atome und Moleküle, Ph.D. thesis, Max-Planck-Institut für Quantenoptik, Garching, und Fakultät für Physik, Technische Universität München (2007).

[Rie07b] T. Rieger, P. Windpassinger, S. A. Rangwala, G. Rempe, and P. W. H. Pinkse. Trapping of Neutral Rubidium with a Macroscopic Three-Phase Electric Trap. *Phys. Rev. Lett.* **99**, 063001 (2007).

[Roa08] G. Roati, C. D'Errico, L. Fallani, M. Fattori, C. Fort, M. Zaccanti, G. Modugno, M. Modugno, and M. Inguscio. Anderson localization of a non-interacting Bose–Einstein condensate. *Nature* **453**, 895 (2008).

[Sag05] J. M. Sage, S. Sainis, T. Bergeman, and D. DeMille. Optical Production of Ultracold Polar Molecules. *Phys. Rev. Lett.* **94**, 203001 (2005).

[Sal09] T. Salzburger and H. Ritsch. Collective transverse cavity cooling of a dense molecular beam. *New J. Phys.* **11**, 055025 (2009).

[San65] P. G. H. Sandars. The Electric Dipole Moment of an Atom. *Phys. Lett.* **14**, 194 (1965).

[Sau06a] B. E. Sauer, H. T. Ashworth, J. J. Hudson, M. R. Tarbutt, and E. A. Hinds, Probing the electron EDM with cold molecules, in Atomic Physics 20: XX International Conference on Atomic Physics, *AIP Conference Proceedings*, volume 869, editors C. Roos, H. Häffner, and R. Blatt (2006).

[Sau06b] B. E. Sauer, H. T. Ashworth, J. J. Hudson, M. R. Tarbutt, and E. A. Hinds, Probing the electron EDM with cold molecules, arXiv.org:physics/0611155 (2006).

[Saw08] B. C. Sawyer, B. K. Stuhl, D. Wang, M. Yeo, and J. Ye. Molecular Beam Collisions with a Magnetically Trapped Target. *Phys. Rev. Lett.* **101**, 203203 (2008).

[Sch04] M. Schulz, Laserspektroskopische Untersuchung von druckinduzierten Effekten an Absortionslinien des Formaldehyds im ultravioletten Spektralbereich, Ph.D. thesis, Fakultät II - Mathematik und Naturwissenschaften, Technische Universität Berlin (2004).

[Sch07a] M. Schenk, State-selective detection of electrostatically guided cold formaldehyde, Master's thesis, Max-Planck-Institut für Quantenoptik, Garching und Friedrich-Schiller-Universität Jena (2007).

[Sch07b] S. Schlunk, A. Marian, P. Geng, A. P. Mosk, G. Meijer, and W. Schöllkopf. Trapping of Rb Atoms by ac Electric Fields. *Phys. Rev. Lett.* **98**, 223002 (2007).

[Sch08] S. Schlunk, A. Marian, W. Schöllkopf, and G. Meijer. ac electric trapping of neutral atoms. *Phys. Rev. A* **77**, 043408 (2008).

[Sho91] S. L. Shostak, W. L. Ebenstein, and J. S. Muenter. The dipole moment of water. I. Dipole moments and hyperfine properties of H_2O and HDO in the ground and excited vibrational states. *J. Chem. Phys.* **94**, 5875 (1991).

[Sie86] A. E. Siegman. Lasers. University Science Books, Mill Valley, California (1986).

[Smi06] C. A. Smith, F. D. Pope, B. Cronin, C. B. Parkes, and A. J. Orr-Ewing. Absorption Cross Sections of Formaldehyde at Wavelengths from 300 to 340 nm at 294 and 245 K. *J. Phys. Chem. A* **110**, 11645 (2006).

[Sof09] D. Sofikitis, S. Weber, A. Fioretti, R. Horchani, M. Allegrini, B. Chatel, D. Comparat, and P. Pillet. Molecular vibrational cooling by optical pumping with shaped femtosecond pulses. *New J. Phys.* **11**, 055037 (2009).

[Som09] C. Sommer, L. D. van Buuren, M. Motsch, S. Pohle, J. Bayerl, P. W. H. Pinkse, and G. Rempe. Continuous guided beams of slow and internally cold polar molecules. *Faraday Discuss.* **142**, 203 (2009).

[Spe35] R. Spence and W. Wild. The Preparation of Liquid Monomeric Formaldehyde. *J. Chem. Soc.* p. 338 (1935).

[Sta97] H. Stapelfeldt, H. Sakai, E. Constant, and P. B. Corkum. Deflection of Neutral Molecules using the Nonresonant Dipole Force. *Phys. Rev. Lett.* **79**, 2787 (1997).

[Sta04] C. A. Stan, M. W. Zwierlein, C. H. Schunck, S. M. F. Raupach, and W. Ketterle. Observation of Feshbach Resonances between Two Different Atomic Species. *Phys. Rev. Lett.* **93**, 143001 (2004).

[Sti01] F. Stienkemeier and A. F. Vilesov. Electronic spectroscopy in He droplets. *J. Phys. Chem.* **115**, 10119 (2001).

[Stu08] B. K. Stuhl, B. C. Sawyer, D. Wang, and J. Ye. Magneto-optical Trap for Polar Molecules. *Phys. Rev. Lett.* **101**, 243002 (2008).

[Tar09] M. R. Tarbutt, J. J. Hudson, B. E. Sauer, and E. A. Hinds. Prospects for measuring the electric dipole moment of the electron using electrically trapped polar molecules. *Faraday Discuss.* **142**, 37 (2009).

[Tes02] C. M. Tesch and R. de Vivie-Riedle. Quantum Computation with Vibrationally Excited Molecules. *Phys. Rev. Lett.* **89**, 157901 (2002).

[Toe98] J. P. Toennies and A. F. Vilesov. Spectroscopy of Atoms and Molecules in Liquid Helium. *Annu. Rev. Phys. Chem.* **49**, 1 (1998).

[Tor08a] K. Tordrup and K. Mølmer. Quantum computing with a single molecular ensemble and a cooper-pair box. *Phys. Rev. A* **77**, 020301(R) (2008).

[Tor08b] K. Tordrup, A. Negretti, and K. Mølmer. Holographic Quantum Computing. *Phys. Rev. Lett.* **101**, 040501 (2008).

[Tow75] C. H. Townes and A. L. Schawlow. Microwave Spectroscopy. Dover Publications, New York (1975).

[Tsu07] H. Tsuji, Y. Okuda, T. Sekiguchi, and H. Kanamori. Velocity distribution of the pulsed ND_3 molecular beam selected by a quadrupole Stark velocity filter. *Chem. Phys. Lett.* **436**, 331 (2007).

[Van07] N. Vanhaecke, U. Meier, M. Andrist, B. H. Meier, and F. Merkt. Multistage Zeeman deceleration of hydrogen atoms. *Phys. Rev. A* **75**, 031402(R) (2007).

[vB09] L. D. van Buuren, C. Sommer, M. Motsch, S. Pohle, M. Schenk, J. Bayerl, P. W. H. Pinkse, and G. Rempe. Electrostatic Extraction of Cold Molecules from a Cryogenic Reservoir. *Phys. Rev. Lett.* **102**, 033001 (2009).

[vdH81] H. C. van de Hulst. Light Scattering by Small Particles. Dover Publications, New York (1981).

[vdM08] S. Y. T. van de Meerakker, H. L. Bethlem, and G. Meijer. Taming molecular beams. *Nature Phys.* **4**, 595 (2008).

[Vit08] M. Viteau, A. Chotia, M. Allegrini, N. Bouloufa, O. Dulieu, D. Comparat, and P. Pillet. Optical Pumping and Vibrational Cooling of Molecules. *Science* **321**, 232 (2008).

[Vol02] A. Volpi and J. L. Bohn. Magnetic-field effects in ultracold molecular collisions. *Phys. Rev. A* **65**, 052712 (2002).

[Vol06] T. Volz, N. Syassen, D. M. Bauer, E. Hansis, S. Dürr, and G. Rempe. Preparation of a quantum state with one molecule at each site of an optical lattice. *Nature Phys.* **2**, 692 (2006).

[Vol07] T. Volz, Ultracold Rubidium Molecules, Ph.D. thesis, Max-Planck-Institut für Quantenoptik, Garching, und Fakultät für Physik, Technische Universität München (2007).

[Vul00] V. Vuletić and S. Chu. Laser Cooling of Atoms, Ions, or Molecules by Coherent Scattering. *Phys. Rev. Lett.* **84**, 3787 (2000).

[Vul01] V. Vuletić, H. W. Chan, and A. T. Black. Three-dimensional cavity Doppler cooling and cavity sideband cooling by coherent scattering. *Phys. Rev. A* **64**, 033405 (2001).

[Wal08] M. Wallquist, P. Rabl, M. D. Lukin, and P. Zoller. Theory of cavity-assisted microwave cooling of polar molecules. *New J. Phys.* **10**, 063005 (2008).

[Wal09] T. E. Wall, S. Armitage, J. J. Hudson, B. E. Sauer, J. M. Dyne, E. A. Hinds, and M. R. Tarbutt. Transport of polar molecules by an alternating-gradient guide. *Phys. Rev. A* **80**, 043407 (2009).

[Wan96] H. Wang, P. L. Gould, and W. C. Stwalley. Photoassociative spectroscopy of ultracold ^{39}K atoms in a high-density vapor-cell magneto-optical trap. *Phys. Rev. A* **53**, R1216 (1996).

[Wan04] D. Wang, J. Qi, M. F. Stone, O. Nikolayeva, H. Wang, B. Hattaway, S. D. Gensemer, P. L. Gould, E. E. Eyler, and W. C. Stwalley. Photoassociative Production and Trapping of Ultracold KRb Molecules. *Phys. Rev. Lett.* **93**, 243005 (2004).

[Wat67] J. K. G. Watson. Determination of Centrifugal Distortion Coefficients of Asymmetric-Top Molecules. *J. Chem. Phys.* **46**, 1935 (1967).

[Wat68] J. K. G. Watson. Determination of Centrifugal-Distortion Coefficients of Asymmetric-Top Molecules. III. Sextic Coefficients. *J. Chem. Phys.* **48**, 4517 (1968).

[Web08] B. Weber, Distribution of quantum information between an atom and two photons, Ph.D. thesis, Max-Planck-Institut für Quantenoptik, Garching, und Fakultät für Physik, Technische Universität München (2008).

[Web09] B. Weber, H. P. Specht, T. Müller, J. Bochmann, M. Mücke, D. L. Moehring, and G. Rempe. Photon-Photon Entanglement with a Single Trapped Atom. *Phys. Rev. Lett.* **102**, 030501 (2009).

[Wei98] J. D. Weinstein, R. deCarvalho, T. Guillet, B. Friedrich, and J. M. Doyle. Magnetic trapping of calcium monohydride molecules at millikelvin temperatures. *Nature* **395**, 148 (1998).

[Wil96] I. D. Williams, D. M. Revitt, and R. S. Hamilton. A comparison of carbonyl compound concentrations at urban roadside and indoor sides. *Sci. Tot. Environ.* **189/190**, 475 (1996).

[Wil08a] S. Willitsch, M. T. Bell, A. D. Gingell, S. R. Procter, and T. P. Softley. Cold Reactive Collisions between Laser-Cooled Ions and Velocity-Selected Neutral Molecules. *Phys. Rev. Lett.* **100**, 043203 (2008).

[Wil08b] S. Willitsch, M. T. Bell, A. D. Gingell, and T. P. Softley. Chemical applications of laser- and sympathetically-cooled ions in ion traps. *Phys. Chem. Chem. Phys.* **10**, 7200 (2008).

[Win75] D. J. Wineland and W. M. Itano. Laser cooling of atoms. *Phys. Rev. A* **20**, 1521 (1975).

[Win78] D. J. Wineland, R. E. Drullinger, and F. L. Walls. Radiation-Pressure Cooling of Bound Resonant Absorbers. *Phys. Rev. Lett.* **40**, 1639 (1978).

[Wu57] C. S. Wu, E. Ambler, R. W. Hayward, D. D. Hoppes, and R. P. Hudson. Experimental Test of Parity Conservation in Beta Decay. *Phys. Rev.* **105**, 1413 (1957).

[Wut04] M. Wutz, H. Adam, and W. Walcher. Handbuch Vakuumtechnik: Theorie und Praxis. Vieweg, Wiesbaden, 8th edition (2004).

[Zac54] J. R. Zacharias. Precision Experiments with Molecular Beams. *Phys. Rev.* **94**, 751 (1954).

[Zar88] R. C. Zare. Angular Momentum: Understanding spatial aspects in chemistry and physics. John Wiley and Sons, New York (1988).

[Zep07] M. Zeppenfeld, M. Motsch, P. W. H. Pinkse, and G. Rempe. Doppler-free spectroscopy of weak transitions: An analytical model applied to formaldehyde. *Appl. Phys. B* **89**, 475 (2007).

[Zep09] M. Zeppenfeld, M. Motsch, P. W. H. Pinkse, and G. Rempe. Optoelectrical cooling of polar molecules. *Phys. Rev. A* **80**, 041401(R) (2009).

[Żuc09] P. S. Żuchowski and J. M. Hutson. Low-energy collisions of NH_3 and ND_3 with ultracold Rb atoms. *Phys. Rev. A* **79**, 062708 (2009).

[Zwi03] M. W. Zwierlein, C. A. Stan, C. H. Schunck, S. M. F. Raupach, S. Gupta, Z. Hadzibabic, and W. Ketterle. Observation of Bose-Einstein Condensation of Molecules. *Phys. Rev. Lett.* **91**, 250401 (2003).

List of Publications

Fine-Structure Splitting in a Fabry-Perot Resonator due to Berry's Geometric Phase
M. Zeppenfeld, M. Koch, B. Hagemann, M. Motsch, P. W. H. Pinkse, and G. Rempe.
In preparation (2009).

Velocity-selected pulses of slow molecules produced by an electric guide
C. Sommer, M. Motsch, L. D. van Buuren, S. Chervenkov, M. Zeppenfeld, P. W. H. Pinkse, and G. Rempe.
In preparation (2009).

Cavity-Enhanced Rayleigh Scattering
M. Motsch, M. Zeppenfeld, P. W. H. Pinkse, and G. Rempe.
In preparation, arXiv.org:0409.4405 (2009).

Optoelectrical cooling of polar molecules
M. Zeppenfeld, M. Motsch, P. W. H. Pinkse, and G. Rempe.
Phys. Rev. A **80**, 041401(R) (2009).

Continuous guided beams of slow and internally cold polar molecules
C. Sommer, L. D. van Buuren, M. Motsch, S. Pohle, J. Bayerl, P. W. H. Pinkse, and G. Rempe.
Faraday Discuss. **142**, 203 (2009).

Collisional effects in the formation of cold guided beams of polar molecules
M. Motsch, C. Sommer, M. Zeppenfeld, L. D. van Buuren, P. W. H. Pinkse, and G. Rempe.
New J. Phys. **11**, 055030 (2009).

Electrostatic Extraction of Cold Molecules from a Cryogenic Reservoir
L. D. van Buuren, C. Sommer, M. Motsch, S. Pohle, M. Schenk, J. Bayerl, P. W. H. Pinkse, and G. Rempe.
Phys. Rev. Lett. **102**, 033001 (2009).

Cold guided beams of water isotopologs
M. Motsch, L. D. van Buuren, C. Sommer, M. Zeppenfeld, G. Rempe, and P. W. H. Pinkse.
Phys. Rev. A **79**, 013405 (2009).

Inelastic electron collisions of the isotopically symmetric helium dimer ion $^4He_2^+$ in a storage ring
H. Buhr, H. B. Pedersen, S. Altevogt, V. M. Andrianarijaona, H. Kreckel, L. Lammich, S. Novotny, D. Strasser, J. Hoffmann, M. Lange, M. Lestinsky, M. B. Mendes, M. Motsch, O. Novotný, D. Schwalm, X. Urbain, D. Zajfman, and A. Wolf.
Phys. Rev. A **77**, 032719 (2008).

Spectroscopy of the $\tilde{A}^1A_2 \leftarrow \tilde{X}^1A_1$ transition of formaldehyde in the 30140–30790 cm^{-1} range: the $2_0^1 4_0^3$ and $2_0^2 4_0^1$ rovibrational bands
M. Motsch, M. Schenk, M. Zeppenfeld, M. Schmitt, W. L. Meerts, P. W. H. Pinkse, and G.Rempe.
J. Mol. Spec. **252**, 25 (2008).

Internal-state thermometry by depletion spectroscopy in a cold guided beam of formaldehyde
M. Motsch, M. Schenk, L. D. van Buuren, M. Zeppenfeld, P. W. H. Pinkse, and G. Rempe.
Phys. Rev. A **72**, 061402(R) (2007).

Doppler-free spectroscopy of weak transitions: An analytical model applied to formaldehyde
M. Zeppenfeld, M. Motsch, P. W. H. Pinkse, and G. Rempe.
Appl. Phys. B **89**, 475 (2007)

High-Resolution Dissociative Recombination of Cold H_3^+ and First Evidence for Nuclear Spin Effects
H. Kreckel, M. Motsch, J. Mikosch, J. Glosík, R. Plašil, S. Altevogt, V. Andrianarijaona, H. Buhr J. Hoffmann, L. Lammich, M. Lestinsky, I. Nevo, S. Novotny, D. A. Orlov, H. B. Pedersen, F. Sprenger, A. S. Terekhov, J. Toker, R. Wester, D. Gerlich, D. Schwalm, A. Wolf, and D. Zajfman.
Phys. Rev. Lett. **95**, 263201 (2005).

Towards state selective measurements of the H_3^+ dissociative recombination rate coefficient
H. Kreckel, J. Mikosch, R. Wester, J. Glosík, R. Plašil, M. Motsch, D. Gerlich, D. Schwalm, D. Zajfman, and A. Wolf.
J. Phys.: Conf. Ser. **4**, 126 (2005).

Danksagung

Zum Schluss möchte ich die Gelegenheit nutzen, all denjenigen meinen Dank auszusprechen, die auf vielfältige Weise zum Gelingen dieser Arbeit beigetragen haben.

An erster Stelle möchte ich meinem Doktorvater **Prof. Dr. Gerhard Rempe** für die Gelegenheit danken, diese Arbeit in seiner Gruppe am MPQ durchzuführen. Insbesondere hervorzuheben ist seine Unterstützung beim Verfolgen neuer Ideen, bereichernde Diskussionen und Denkanstöße, sowie die spürbare Begeisterung für unsere Forschungsarbeit.

Dr. Pepijn Pinkse, der im Rahmen seiner Habilitation das Molekülexperiment leitete, danke ich für die direkte Betreuung meiner Doktorarbeit. Er unterstützte mich bei der Entwicklung meiner Ideen und nahm sich stets die Zeit, über die unterschiedlichsten Aspekte des Experiments und der Theorie zu diskutieren.

Dr. Laurens van Buuren danke ich für die Unterstützung am Experiment, die reibungslose Zusammenführung der beiden Molekülexperimente sowie für die Bereitschaft, diverse Manuskripte bereits im frühen Entwurfsstadium zu lesen. Wann immer ich einen erfahrenen Wissenschaftler zur Diskussion von Messdaten oder auch bei ganz allgemeinen Fragestellungen brauchte, war er zur Stelle.

Bei meinen Mitstreitern am Molekülexperiment, **Martin Zeppenfeld**, **Christian Sommer**, **Dr. Sotir Chervenkov**, **Barbara Englert** und **Manuel Mielenz**, bedanke ich mich für die gute Zusammenarbeit am Experiment, für spannende und ergiebige Diskussionen über das Kühlen von Molekülen und andere Visionen, sowie für die schöne Zeit, die wir miteinander hatten.

Meinem ehemaligen Diplomanden **Markus Schenk** danke ich für den bedingungslosen Einsatz im Labor: die Bekämpfung von Farbstoffkatastrophen, die an den Kampf mit der Hydra erinnernde Aufnahme von Molekülspektren, sowie die odysseische Suche nach dem schon verschollen geglaubten Depletion-Signal der geführten Moleküle.

Meinen Vorgängern am Molekülexperiment, **Dr. Thomas Rieger** und **Dr. Tobias Junglen**, danke ich für die gute Einarbeitung ins Experiment sowie für praktische Ratschläge zum Überleben am MPQ. Übrigens, Farbstofflaser sind schön.

Alfonso Peréz Escudero danke ich für die Unterstützung bei den ersten Ausflügen in die Molekülspektroskopie.

Dr. Michael Schmitt danke ich für seine spontan zugesagte Hilfe bei der Interpretation der Formaldehydspektroskopie.

Dr. Tobias Schätz danke ich für spannende Gespräche, aufbauende Worte, wenn im Labor mal wieder gar nichts zu laufen schien, sowie für Ratschläge zur wissenschaftlichen Karriereplanung.

Axel Friedenauer danke ich für Erste Hilfe bei der Optimierung der Frequenzverdopplung.

Dr. Ingrid Schuster danke ich für Ratschläge, wie man seine Doktorarbeit verfasst und was beim Gang durch die Mühlen der Bürokratie zu beachten ist. **Dr. Niels Syassen** danke ich für die Bereitstellung des LaTeX-Templates, das hervorragende Dienste geleistet hat, und für seine Linux-Beratungsstunde.

Dr. Stephan Dürr danke ich für seine Bereitschaft, mir mit ausführlichen Gesprächen beim Durchdringen der unterschiedlichsten physikalischen Probleme zur Seite zu stehen.

Dank der exzellenten Unterstützung durch **Josef Bayerl**, **Franz Denk**, **Helmuth Stehbeck** und **Thomas Wiesmeier** konnte ich meine Experimente in einem anfangs leeren Labor aufbauen. Selbst unmöglich scheinende Wünsche wurden umgehend und technisch perfekt umgesetzt.

Odette Gori danke ich für ihr Organisationstalent und ihre Hilfsbereitschaft.

Der ganzen Arbeitsgruppe von Prof. Rempe danke ich für die motivierende und inspirierende Atmosphäre, sowie für ihre kollegiale Art. Erst diese ermöglichen hochkarätige wissenschaftliche Arbeit. In unserer gemeinsamen Zeit habe ich gute Freunde unter euch gefunden. Danke an alle!

Bei meinen ehemaligen Heidelberger bzw. Freiburger Kollegen **Dr. Holger Kreckel** und **Dr. Jochen Mikosch** habe ich das Handwerkszeug des Experimentalphysikers gelernt. Danke dafür!

Dr. Sascha Reinhard danke ich für seine Ratschläge auf der Suche nach einem Projekt für meine Doktorarbeit. Stichwort: „Farbstofflaser“.

Ein herzliches Dankeschön an meine **Freunde**, denen es gelang, mich den Sorgen und Nöten im Labor zu entreißen.

Zuletzt möchte ich ganz besonders meinen **Eltern** und meiner ganzen **Familie** für ihre immerwährende Unterstützung und den Rückhalt danken.

Danke **Bettina**!